Submitted to *Int. J. Mass Spectrom.* (Issue honoring A. G. Harrison)

The Simplest b_2^+ Ion: Determining Its Structure from Its Energetics by a Direct Comparison of the Threshold Collision-induced Dissociation of Protonated Oxazolone and Diketopiperazine

P. B. Armentrout and Amy A. Clark

315 S. 1400 E. Rm 2020, Chemistry Department, University of Utah, Salt Lake City, UT 84112

Abstract

Energy-resolved collision-induced dissociation of b_2^+ ions derived from protonated GGG and GAG are compared with that of protonated diketopiperazine (H^+DKP). Absolute dissociation cross sections are obtained using a guided ion beam tandem mass spectrometer and analyzed using statistical methods. The fragmentation pattern of the b_2^+ ion from H^+GGG differs significantly from that of H^+DKP, although decarbonylation (forming the a_2^+ ion) is the lowest energy pathway found for both species. The threshold measured for b_2^+ decarbonylation differs appreciably from that of H^+DKP, but both processes have onsets that are consistent with those obtained from quantum chemical calculations, positively identifying the b_2^+ ion as the protonated 2-aminomethyl-5-oxazolone, H^+AMOx. The threshold for the b_2^+ ion derived from H^+GAG has a slightly lower threshold, again consistent with theory. Examination of the higher energy dissociation pathways observed shows that these generally involve subsequent dissociation of the primary a_2^+ product ion. As a consequence, statistical analysis of these pathways for threshold information is difficult and ultimately provides little agreement with theory. This disagreement is rationalized on the basis of considerable kinetic energy release that has been observed previously by Harrison for these subsequent reactions. The present results are also favorably compared with previous results obtained by Siu and coworkers, although a number of refinements in the analysis and mechanisms are suggested.

Key words: b_2 ions, collision-induced dissociation, diketopiperazine, oxazolone, thermochemistry

Introduction

The gas phase fragmentation of protonated peptides often occurs at the peptide linkages, producing b ions when the charge is retained on the N-terminal fragment and y ions when the C-terminal fragment carries the charge. Structural identification of b ions along with their energetics and mechanisms of formation has been an active focus of much investigation recently because such information could aid in improving models for peptide fragmentation, thereby extending the utility of peptide sequencing by mass spectrometric approaches. For the smallest b_2^+ species, there are two principal structures: the six-membered cyclic diketopiperazine (DKP), formed by nucleophilic attack of the N-terminal amino group at the carbonyl carbon of the second residue; and the five-membered cyclic oxazolone (Ox), formed by nucleophilic attack of the carbonyl oxygen on the first reside at the carbonyl carbon of the second residue. A variety of mass spectrometric experiments and comparisons to theory, including seminal contributions from Harrison, have suggested that the oxazolone structure is generally formed [1-8]. Recent studies using infrared multiple photon dissociation (IRMPD) spectroscopy combined with theory have provided more direct evidence for such identifications, again usually finding Ox structures [9-15]; however, the b_2^+ ion derived from protonated histidine-alanine (HA) shows a mixture of the DKP and Ox structures [16].

Although identification of the structures of the fragments of peptides is important information, improving models of peptide fragmentation would also benefit from experimental determinations of both mechanistic and energetic details, information that IRMPD studies are not capable of providing. Energy-resolved collision-induced dissociation (CID) studies can provide much of the needed energetic information, and in addition can provide an alternative means of determining structure as well as exploring mechanisms by comparisons to theory . However, such quantitative experimental characterizations of peptides are few [17-25], with most not capable of acquiring accurate energetic information. An early pioneering study of Klassen and Kebarle [18] examined kinetic energy-resolved CID fragmentation of protonated G_n (n = 1 - 4) and several related compounds, acquiring thresholds for the primary dissociation pathways. Siu

and coworkers examined the energy-resolved CID of protonated GGG, AGG, and GAG and extracted threshold energy information that compares well with theory [20,21]. Recently, we completed a similar study of protonated glycine and diglycine, again obtaining information that could be compared favorably with theory [23-25]. These latter studies illustrate the utility of having good quantitative thermodynamic information available to confirm theoretical studies of mechanisms and product structures.

In addition to the examination of the dissociation of intact amino acids and peptides, in-source fragmentations can be used to generate fragment ions, which can then be subject to interrogation using IRMPD (as in the studies referenced above) or energy-resolved CID. Indeed, Siu and coworkers have previously examined energy-resolved collision-induced dissociation of the b_2^+ and a_2^+ ions formed by decomposition of H^+GGG [20]. For the b_2^+ ion, they observed two products: loss of CO to form the a_2^+ product ion and formation of the a_1^+ ion, $CH_2NH_2^+$, although no cross sections for these processes are provided. For the a_2^+ ion, the primary product is a_1^+ along with an additional minor product ion at *m/*z 59, but no energetic information is given for this product. Their energy-dependent cross sections were analyzed using our data analysis program, CRUNCH, to obtain threshold energies (with and without kinetic shifts), although none of the additional parameters used to reproduce the data were reported (such that the shape and magnitudes of the cross sections remain unknown). Theoretical calculations at a B3LYP/6-31++G(d,p) level were used to outline the mechanisms for these fragmentations, with good agreement reported between experimental and theoretical threshold energies. Similar experiments and calculations were carried out for the b_2^+ and a_2^+ ions formed from H^+GAG and H^+AGG [21].

In the present work, we initiate our own exploration of peptide fragment ions by examining the simplest b_2^+ ion, the major product ion formed in the fragmentation of H^+GGG. This provides an ideal test system as both previous IRMPD [13] and energy-resolved CID [20] work is available for comparison. IRMPD studies identify the structure of the b_2^+ ion as protonated 2-aminomethyl-5-oxazolone (H^+AMOx, protonated on the ring nitrogen) by good agreement with

theory and by direct comparison with an authentic sample of protonated diketopiperazine (H^+DKP, protonated on the oxygen). The CID work similarly finds consistency between theory and experiment when the b_2^+ ion is identified as H^+AMOx, although no direct comparisons to H^+DKP were made. As described in the Supplemental Information, there are some questions regarding these triple quadrupole experiments, such that a reinvestigation of these systems is also warranted. In addition, the present study extends this work a) by examining the b_2^+ fragmentation of H^+GGG and H^+GAG over a broader range of energies and with more sensitivity, b) by directly comparing the fragmentation of the b_2^+ ion with that of protonated DKP, and c) by revealing additional details regarding the relevant potential energy surfaces through an exploration at higher levels of theory.

Experimental and Computational Section

General Experimental Procedures

Cross sections for CID of the ions investigated here are measured using a guided ion beam tandem mass spectrometer that has been described in detail previously [26,27]. Ions are generated using an electrospray ionization (ESI) source [28-31] and an in-source fragmentation technique [32] for generation of thermalized b_2^+ ions from H^+GGG and H^+GAG. Details of the experimental methods and means of data analysis [33-35] can be found in the Supplemental Information. Measured cross sections have absolute and relative uncertainties of ±20% and 5%, respectively. The energy scale has an absolute uncertainty of ±0.03 eV in the center-of-mass frame.

Computational Approach

Model structures and vibrational frequencies for reactants, products, transition states, and intermediate species were performed at the B3LYP/6-311+G(d,p) level with energetics corrected for zero point energies determined by single point calculations at B3LYP/6-311+G(2d,2p) and MP2(full)/6-311+G(2d,2p) levels. Recent work has shown that these levels of theory provide

accurate comparisons with experimental energetics for such protonated systems, with mean absolute deviations of about 10 kJ/mol [23,24,36]. Details of the procedures used can be found in the Supplemental Information. We also compare these results with lower level B3LYP/6-31++G(d,p) results of Siu and coworkers [20,21]. In the Supplemental Information, a comparison of these approaches with previous literature results [23] suggests that the double-ζ basis set yields energies that are high. Indeed, for the present systems, these calculations average 16 ± 10 kJ/mol higher than the present triple-ζ B3LYP/6-311+G(d,p) results.

Nomenclature

To identify the various conformations of the molecules in this work, we use a nomenclature derived from the peptides that act as precursors to the b_2^+ ions and their fragments. This nomenclature specifies the site of protonation in brackets followed by a designation of any dihedral angles going from nitrogen that was the N terminus (N_1) along the backbone of the molecules, where c (cis) stands for angles < 45°, g (gauche) for angles between 45° and 135°, and t (trans) for angles > 135°. Thus the ground state (GS) of H^+AMOx is [N_2]-c where the N_2 designation indicates the proton is on the ring nitrogen and the aminomethyl group is cis relative to the ring (∠NCCN dihedral angle). The GS of H^+DKP is [O_c] indicating that the carbonyl oxygen is protonated and the proton has a cis orientation along the ∠CCOH dihedral. The position of the N-terminal amino group of H^+AMOx (when not protonated or involved in a hydrogen bond) can also be rotated but is often such that the lone-pair is cis with respect to the CC bond. When the amino group is rotated to the trans position, the ∠NCCN dihedral is augmented by a subscript t. Transition states are indicated by TS followed by the protonation site and backbone conformation. TSs for proton transfer steps are named like TS[N_1-N_2]-c and those for dihedral angle rotations as TS[N_2]-(cg). TSs involving bond cleavage indicate the bond being broken by ~ inside curly brackets, e.g. {OC~O}. Although more complicated than simply numbering species, we believe this nomenclature allows better visualization of the species.

UU IR Author Manuscript

Results and Discussion

Cross Sections for Collision-Induced Dissociation

Kinetic energy dependent experimental cross sections were obtained for the interaction of Xe with the b_2^+ ion of H^+GGG, H^+DKP, and the b_2^+ ion of H^+GAG, Figure 1. Data shown are a mean of results taken at xenon pressures of ~0.05 and 0.1 mTorr, as little pressure dependence was detected within our experimental uncertainties at these lower pressures, but at the higher pressure of 0.2 mTorr, shifts in the apparent thresholds are obvious, especially for the higher energy channels. Three processes are observed in the b_2^+ (*m/z* 115) system. The primary product is loss of CO to form the a_2^+ product ion at *m/z* 87 in reaction (1). The cross section for this species reaches a maximum near the onset of the species observed at higher energies, *m/z* 59 and 30, indicating subsequent decomposition or competition. These peaks can be identified as $H^+(CH_2NH)_2$ and $CH_2NH_2^+$ (a_1^+), respectively. The small magnitude of the cross section for reaction (2) is consistent with the suggestion that this product decomposes by reaction (3a), i.e., the a_2^+ ion undergoes CO loss followed rapidly by decomposition of the proton bound dimer to yield the a_1^+ ion as the dominant high energy species.

$$C_4H_7N_2O_2^+ (b_2^+) + Xe \rightarrow C_3H_7N_2O^+ (a_2^+) + CO + Xe \quad (1)$$

$$\rightarrow C_2H_7N_2^+ + CO \quad (2)$$

$$\rightarrow CH_2NH_2^+ (a_1^+) + CH_2NH \quad (3a)$$

$$\rightarrow CH_2NH_2^+ (a_1^+) + (C_3H_3NO_2) + Xe \quad (3b)$$

It is also possible that the a_1^+ ion is formed directly from the parent b_2^+ ion in reaction (3b), as interpreted by Siu and coworkers [20]. The present results are consistent with the general results of Siu and coworkers who report observation of reactions (1) and (3), but not reaction (2); however, they do observe a small peak at *m/z* 59 in their mass spectrum for dissociation of the a_2^+ ion along with the major peak at *m/z* 30.

Decomposition of H^+DKP (also *m/z* 115) shows the same three products as b_2^+ as well as additional peaks at *m/z* 58 and 43, which we assign to $C_2H_4NO^+$ and $C_2H_3O^+$, presumably the acetyl cation (protonated ketene), respectively, as formed in reactions (5) and (6).

$$C_4H_7N_2O_2^+ + Xe \rightarrow C_3H_7N_2O^+ + CO + Xe \quad (4)$$

$$\rightarrow C_2H_4NO^+ + CH_2NH \quad (5)$$

$$\rightarrow C_2H_3O^+ + (C_2H_4N_2O) + Xe \quad (6)$$

In comparison with the cross sections in Figure 1a, that for *m/z* 87 is much smaller with an onset about 1 eV higher in energy. Its cross section again shows evidence that it decomposes first to $H^+(CH_2NH)_2$, which then dissociates to $CH_2NH_2^+$ (a_1^+). The relative behavior of the *59* peaks is comparable in the two energy-resolved spectra, whereas that for *m/z* 30 shows a higher energy threshold from H^+DKP. Because they are minor products, the species at *m/z* 58 and 43 cannot be clearly assigned precursors, although it is clear that the onset for $C_2H_4NO^+$ is slightly below that for $CH_2NH_2^+$, although much less efficient. This behavior is consistent with identifying the *m/z* 58 species as $CH_2NH_2^+(CO)$, as discussed further below.

Threshold CID of the b_2^+ ion obtained from H^+GAG is shown in Figure 1c and exhibits four products formed in reactions (7) – (10).

$$C_5H_9N_2O_2^+ (b_2^+) + Xe \rightarrow C_4H_9N_2O^+ (a_2^+) + CO + Xe \quad (7)$$

$$\rightarrow C_3H_9N_2^+ + CO \quad (8)$$

$$\rightarrow C_2H_4NH_2^+ + CH_2NH \quad (9a)$$

$$\rightarrow CH_2NH_2^+ (a_1^+) + C_2H_4NH \quad (10a)$$

$$\rightarrow C_2H_4NH_2^+ + (C_3H_3NO_2) + Xe \quad (9b)$$

$$\rightarrow CH_2NH_2^+ (a_1^+) + (C_4H_5NO_2) + Xe \quad (10b)$$

The cross section for the primary a_2^+ product ion (*m/z* 101) is similar to that for the analogous species in Figure 1a, but has a lower apparent threshold by about 0.3 eV. Cross sections for the a_1^+ ion (*m/z* 30) have similar shapes and relative magnitudes in both the H^+GGG and H^+GAG b_2^+ ions, however, the latter system also exhibits the methylated iminium ion at *m/z* 44. This has a lower apparent threshold by about 0.6 eV, but otherwise exhibits a similar shape and magnitude at high energies. Thus, the two iminium ions are likely to be formed via similar mechanisms. We also observe the (a_2^+ - CO) product ion at *m/z* 73, but this has a cross section much smaller than that of the analogous product (*m/z* 59) in Figure 1a. This is consistent with this product,

UU IR Author Manuscript

presumably the proton bound complex $(C_2H_4NH)H^+(CH_2NH)$, dissociating to both iminium ions. Because the energy of the methylated iminium is lower in energy, this product dissociates more easily in this system, thereby restricting the magnitude of its cross section. These results are again consistent with those of Siu and coworkers [21] who report observation of reactions (7) and (9), but not reaction (8), although this species is observed as a small peak in their mass spectrum for dissociation of the a_2^+ ion along with the major peaks at *m/z* 44 and 30. It is also interesting that the qualitative behavior observed here has previously been observed by Harrison and coworkers in their energy-resolved CID study of protonated $GlyAlaNH_2$, which dissociates primarily to form the same b_2^+ ion [6]. This group also observed formation of a small amount of the *m/z* 73 ion in studies of the a_2^+ ion derived from this molecule [37].

Theoretical Results for H^+AMOx and H^+DKP Conformers

Several stable structures of both H^+AMOx and H^+DKP were located and are shown in Figure S1. Relative energies of these species and transition states connecting them are given in Table S2. AMOx can be protonated on either nitrogen atom, yielding $[N_1]$ (terminal nitrogen) and $[N_2]$ (ring nitrogen) structures. The most stable of these has a hydrogen bond between N_1 and N_2 with the proton on the N_2 nitrogen, $H^+AMOx[N_2]$-c. The proton can shift to N_1 to form a conformer lying 13 – 24 kJ/mol higher in energy by passing over $TS[N_2\text{-}N_1]$-c, which requires 29 – 39 kJ/mol. There are also $[N_2]$-g, $[N_2]$-g_t, and $[N_1]$-t conformers, lying 28 – 31, 31 – 36, and 33 – 45 kJ/mol, respectively, above $[N_2]$-c. These species have ∠NCCN dihedral angles of 97°, 115°, and 140°, respectively, and have NH•O hydrogen bonds between the terminal N_1H and the ring oxygen. The TSs interconnecting the nitrogen protonated H^+AMOx conformers all lie lower than 51 kJ/mol, Table S2, such that these five conformations can interchange readily. There are also conformations in which the oxygen atoms are protonated, but these lie considerably higher in energy than the N protonated conformers and are not easily connected to the primary reaction pathways. A discussion of these conformers can be found in the Supplemental Information with structures shown in Figure S2 and energetics in Table S3.

UU IR Author Manuscript

The GS conformer of H^+DKP is [O_c], which has an oxygen protonated with the proton cis to the ring carbon (pointing away from the adjacent NH). This isomer of $C_4H_7N_2O_2^+$ lies 7 – 12 kJ/mol *below* H^+AMOx[N_2]-c. If the proton in H^+DKP is trans, the [O_t] structure lies 7 – 8 kJ/mol higher in energy than [O_c], with a TS[O_{c-t}] interconverting these and lying 31 – 33 kJ/mol above the [O_c] GS, Table S2. Protonation of the nitrogen, [N], leads to a much higher energy structure, 52 – 68 kJ/mol above the GS. This is because this proton transfer partially cleaves the C-N bond, which increases from 1.295 and 1.299 Å in [O_c] and [O_t], respectively, to 1.573 Å in [N]. These results parallel those obtained by Balta et al. [38] at a B3LYP/6-31+G(d,p) level of theory and those of Siu and coworkers [20] at a B3LYP/6-31++G(d,p) level for the few species that overlap, Table S2. The transition states leading to [N] are quite high in energy. Proton transfer to the adjacent nitrogen involves a four-centered transition state, TS[O_t-N], which lies 223 – 231 kJ/mol above the GS, whereas proton transfer across the ring, a five-centered TS[O_c-N], lies 237 – 255 kJ/mol above the GS (13 – 24 kJ/mol above TS[O_t-N]). These transformations are shown explicitly below.

If the ion populations were equivalent to a 298 K thermal equilibrium, then the [N_2]-c GS should constitute > 99% of H^+AMOx ions, whereas 94% of H^+DKP ions should have the [O_c] structure with the remainder being [O_t]. Notably, the energy of H^+DKP lies below that of H^+AMOx by 7 – 12 kJ/mol. Thus, if these two structures could readily interconvert, H^+DKP would comprise 95 – 99% of the ion population. Although a detailed mechanism for such interconversion was not explored, a conceivable pathway would involve H^+DKP[N] cleaving the weak OC-NH_2 bond followed by dihedral rotations and formation of the OC-O bond in the five-membered ring of H^+AMOx. Interconversion of these isomers is unlikely because formation of H^+DKP[N] already involves a large barrier (>220 kJ/mol) and, as will be seen below, loss of CO can occur readily once the OC-NH_2 bond is cleaved. Thus, the independent identity of these two species should be retained.

UU IR Author Manuscript

Theoretical Results for H^+AMOx Decarbonylation

The loss of CO from H^+AMOx has a relatively simple mechanism, as shown in Figure 2, which generally parallels that previously elucidated by Siu and coworkers [20], although some differences are found as described below. Tables 1 and S4 list the relative energies of the various intermediates and transition states involved, including those calculated by Siu and coworkers. Their results lie between 4 – 29 kJ/mol higher in energy than the present B3LYP calculations, consistent with the differences found for the calibration reactions discussed in the Supplemental Information. In the following discussion, the previous results of Siu and coworkers for species names and energies are parenthetically indicated in bold.

Cleavage of the OC-O bond of the five-membered ring of the H^+AMOx[N_2]-c GS (**1**) leads to TS(H^+AMOx[N_2]-c{OC~O}) (**1→2**) lying 126 – 132 (**138**) kJ/mol higher in energy. The C-CO and O-CO bonds being broken have lengths of 1.829 and 3.242 Å. This TS is essentially an acylium ion that rearranges to form the $C_3H_7N_2O^+$[N_2]-ct(OC_C) (**2**) complex, in which the CO molecule is weakly bound to the terminal carbon (as indicated by the subscript C) of the $C_3H_7N_2O^+$ (a_2^+) molecule, Figure 2. The latter molecule is protonated on N_2 and has a ct orientation of the ∠NCCN and ∠CCNC dihedral angles that allows a N_2H•N_1 hydrogen bond. The CO can easily migrate to hydrogen bond at the N_2, N_1, or terminal HC positions, forming the (OC_{HN2}), (OC_{HN1}), and (OC_{HC}) complexes, respectively (species that were not explored by Siu and coworkers). These species are isoenergetic with one another within 7 kJ/mol, Table S4, (and therefore not shown in Figure 2) with the (OC_{HN2}) variant being the lowest energy species, but only 1 – 5 kJ/mol below the (OC_C) conformer. TSs between these $C_3H_7N_2O^+$[N_2]-ct(OC) complexes were located, Table S4, and the highest lies less than 8 kJ/mol above the lowest energy complex. All of these TSs are lower than the energy required to lose CO, only 11 – 21 kJ/mol. Because the $C_3H_7N_2O^+$[N_2]-ct (**3**) + CO asymptotic energy lies 29 – 37 (**35**) kJ/mol below the rate-limiting TS leading to its formation (Figure 2), CO should be readily lost from any of these conformers.

It is also possible for the H^+AMOx[N_1]-c conformer to dissociate over TS(H^+AMOx[N_1]-

c{OC~O}) (a pathway not explored by Siu and coworkers), but this TS is 20 – 24 kJ/mol higher than the [N_2] analogue, Figures 2 and S3. This TS leads to $C_3H_7N_2O^+$[N_1]-ct(CO) complexes, having both (OC_{HN1}) and (OC_C) variants, with the former being lower in energy and 7 – 8 kJ/mol lower than the lowest [N_2] complex. This complex lies 67 – 77 kJ/mol above the H^+AMOx GS and requires 20 – 28 kJ/mol to lose CO. It can also shift the proton from N_1 to N_2, which requires only 18 – 23 kJ/mol, Figure S3. Overall, the rate-limiting TS for decarbonylation of H^+AMOx is TS(H^+AMOx[N_2]-c{OC~O}) (**1→2**) and sufficient energy is needed to overcome this TS that CO should be readily lost to yield the $C_3H_7N_2O^+$ (a_2^+) product at *m/z* 87.

Theoretical Results for Methylated H^+AMOx Decarbonylation

As previously elucidated by Siu and coworkers [21], the pathway for decarbonylation of the b_2^+ ion formed from H^+GAG, H^+AMOx methylated on the ring (H^+MAMOx), is directly parallel to that for H^+GGG. Thus, our calculations primarily focus on the rate-limiting steps in these reactions, Table 1. We find two similar pathways for decarbonylation that depend on whether the departing CO leaves on the same side of the ring as the methyl group or on the opposite side. The former, TS(H^+MAMOx[N_2]-ctt{OC~O}) (not located by Siu and coworkers) where ctt indicates the approximate NCCN, CCNC, and CNCC dihedral angles, lies 116 – 120 kJ/mol above the GS, Table 1. The C-CO and O-CO bonds being broken have lengths of 1.898 and 2.532 Å. As in the H^+GGG case, this leads to an acylium-like intermediate having a very weak C-CO bond that leads to formation of $C_4H_9N_2O^+$[N_2]-ctt + CO, 47 – 66 (**58**) kJ/mol above the GS. The second TS, TS(H^+MAMOx[N_2]-ctg{OC~O}) (**1→2**), was located by Siu and coworkers and lies 125 – 129 (**125**) kJ/mol above the GS, with C-CO and O-CO bond lengths of 1.912 (**1.913**) and 2.742 Å. This leads to formation of $C_4H_9N_2O^+$[N_2]-ctc + CO, 59 – 79 kJ/mol above the GS. Note that the ctt orientation of the methyl group lowers the energy of the TS and products by about 10 kJ/mol. This consistent methyl effect disagrees with the results of Siu and coworkers, who show that TS(**1→2**) leads to the ctt conformer, rather than the higher energy ctc orientation. Intrinsic reaction coordinate (IRC) calculations verify the present theoretical results.

UU IR Author Manuscript

As for the H^+GGG system, we also find relatively low-lying TSs for decarbonylation of the H^+MAMOx[N_1] conformer (not located by Siu and coworkers). Again there are two TSs, ctt and ctg, corresponding to whether the CO leaves on the same or opposite side, respectively, as the methyl group. These two TSs lie 141 – 147 and 148 – 152 kJ/mol, respectively, above the GS, Table 1, and lead to $C_4H_9N_2O^+$[N_1]-ctt and ctc + CO products.

Theoretical Results for H^+DKP Decarbonylation

To decarbonylate H^+DKP, the [O_c] GS must first rearrange to the [N] conformer. As discussed above and shown in Figure 3, formation of the [N] conformer requires passing over TS(H^+DKP[O_t-N]), 224 – 231 kJ/mol above the GS, or TS(H^+DKP[O_c-N]), which lies 13 – 24 kJ/mol higher in energy, Table S2. Because protonation of the nitrogen weakens the OC-N bond, cleavage of the adjacent OC-C bond leads to decarbonylation over TS(H^+DKP[N]{C~CO~N}), which lies 158 – 166 kJ/mol above the [O_c] GS, and 65 – 67 kJ/mol *below* the TS for proton transfer, Figure 3 and Table S4. This forms a $C_3H_7N_2O^+$[N_2]-cc(OC_C) complex, in which the $C_3H_7N_2O^+$ fragment now has a cis-cis orientation of the ∠NCCN and ∠CCNC dihedrals and the CO molecule is weakly bound to the terminal C atom. Less than 2 kJ/mol is needed to move the CO molecule to the protonated N_2 site, which lies 10 – 12 kJ/mol lower in energy. This (OC_{HN2}) complex requires only 8 – 21 kJ/mol to lose CO forming $C_3H_7N_2O^+$[N_2]-cc, which lies 29 kJ/mol above the [N_2]-ct conformer formed by decarbonylation of H^+AMOx. Because the $C_3H_7N_2O^+$[N_2]-cc + CO products lie well below the rate-limiting TS, CO should be lost readily once TS(H^+DKP[N]{C~CO~N}) has been passed.

Experimental Results for Decarbonylation of H^+DKP, H^+AMOx, and H^+MAMOx

Eq. (S1) was used to analyze the thresholds for decarbonylation of H^+DKP and the b_2^+ ions derived from H^+GGG and H^+GAG. The data were interpreted assuming rate-limiting TSs of TS(H^+DKP[O_t-N]), TS(H^+AMOx[N_2]-c{OC~O}), and TS(H^+MAMOx[N_2]-ctg{OC~O}), respectively. Results of these analyses are given in Table S5 with threshold energies of 2.17 ±

0.18, 1.56 ± 0.12, and 1.44 ± 0.10 eV, respectively. Also the difference between the thresholds for the two b_2^+ species can be given more precisely as 0.12 ± 0.10 eV because several of the uncertainties associated with the measurements of these absolute threshold energies cancel. Clearly the decarbonylation of H^+DKP differs quantitatively from that for the isobaric b_2^+ ion, indicating they are not the same species, as also indicated by the distinct fragmentation patterns.

Table 2 provides a comparison of these threshold energies to theoretical values for the rate-limiting TSs and to the results of Siu and coworkers for decomposition of the b_2^+ ions of H^+GGG and H^+GAG, 1.45 +0.08/-0.13 [20] and 1.30 +0.08/-0.09 [21] eV, respectively. Our results are slightly greater than those of Siu and coworkers, but within the combined experimental uncertainties. Our experimental values are also in reasonable agreement with theory, with the threshold for H^+DKP being slightly lower (by 10 – 17 kJ/mol) and those for the b_2^+ ions being slightly higher (by 19 – 25 kJ/mol) than the lowest energy TSs predicted. The latter differences are systematic such that theory predicts that methylation will reduce the TS energy by 7 – 12 kJ/mol, compared to 12 ± 10 kJ/mol from experiment. In making these comparisons, it is possible that the experimental threshold is a weighted average of the various TSs having similar energies that all lead to the same product. In such a case, we note that the experimental measurement for b_2^+ (H^+GGG) lies closer to TS(H^+AMOx[N_1]-c{OC~O}) than to the lower energy TS(H^+AMOx[N_2]-c{OC~O}). Likewise, the threshold measured for b_2^+(H^+GAG) is close to the average value of the four possible TSs found, 136 kJ/mol (B3LYP and MP2). In any case, it seems clear that the mechanism elucidated by Siu and coworkers [20,21] and refined here is consistent with the dissociation onset for decarbonylation of the b_2^+ ions. This positively identifies them as protonated 2-aminomethyl-5-oxazolone and its methylated analogue, in agreement with the results for the b_2^+(H^+GGG) ion from comparison of theory and IRMPD studies [13].

Theoretical Results for Rearrangement of $C_3H_7N_2O^+$ (a_2^+)

Once the CO molecule is gone from either H^+AMOx or H^+DKP, the $C_3H_7N_2O^+$ (a_2^+) species can

UU IR Author Manuscript

rearrange further, Figure 4, a surface that was partly explored by Siu and coworkers [20]. The $C_3H_7N_2O^+[N_2]$-ct (**3**) and $C_3H_7N_2O^+[N_1]$-ct species formed by decarbonylation of H^+AMOx are interconnected by TS$[N_2\text{-}N_1]$-ct, lying 13 – 14 kJ/mol above $C_3H_7N_2O^+[N_2]$-ct, 11 – 15 kJ/mol above $C_3H_7N_2O^+[N_1]$-ct, and 16 – 24 kJ/mol below TS(H^+AMOx$[N_2]$-c{OC~O}). It is also possible for this molecule to cyclize creating c-$C_3H_7N_2O^+[N_1]$ (**4**), 40 – 55 (**43**) kJ/mol below $C_3H_7N_2O^+[N_2]$-ct (**3**). We find that the cyclization occurs in two steps, Figure 4. a) Conversion of $C_3H_7N_2O^+[N_2]$-ct (**4**) to $C_3H_7N_2O^+[N_2]$-cc (**12**) over TS($C_3H_7N_2O^+[N_2]$-c(tc)) (**3→4**), 41 – 46 (**48**) kJ/mol above $C_3H_7N_2O^+[N_2]$-ct. b) $C_3H_7N_2O^+[N_2]$-cc (**12**) can rearrange to the cyclic conformer over TS(c-$C_3H_7N_2O^+[N_1]${C~N_1}) (**4→12**), which lies only 8 – 15 (**8**) kJ/mol higher in energy and 2 above to 8 (**10**) kJ/mol below TS($C_3H_7N_2O^+[N_2]$-c(tc)) (**3→4**). Although Siu and coworkers locate all of these species, they convert $C_3H_7N_2O^+[N_2]$-ct (**3**) directly to c-$C_3H_7N_2O^+[N_1]$ (**4**) rather than having $C_3H_7N_2O^+[N_2]$-cc (**12**) be an intermediate between them, Figure 4. Our IRC calculations clearly define the sequence shown in Figure 4 at the level of theory used here (and IRC calculations at the B3LYP/6-31++G(d,p) level used by Siu and coworkers show the same result).

An interesting feature of the present surface is that TS(H^+AMOx$[N_2]$-c{OC~O}) (**1→2**), which must be overcome to form the $C_3H_7N_2O^+$ + CO products from H^+AMOx, is 8 – 12 (**13**) kJ/mol *below* the trans-cis isomerization TS, TS($C_3H_7N_2O^+[N_2]$-c(tc)) (**3→4**), Figure 4. This result suggests that at threshold, the b_2^+ ions should form the $C_3H_7N_2O^+[N_2]$-ct products (**3**), which could rearrange at higher energies to the more stable cyclic c-$C_3H_7N_2O^+[N_1]$ (**4**). Siu and coworkers have suggested that the a_2^+ product ion is the cyclic isomer on the basis of two experiments. The threshold they measured for a_2^+ (formed from in-source fragmentation of H^+GGG) to decompose to a_1^+ ($CH_2NH_2^+$), 143 ± 9 kJ/mol, matched the value calculated for decomposition of c-$C_3H_7N_2O^+[N_1]$ (**4**), 149 (137 – 167 calculated here) kJ/mol, rather than that for decomposition of $C_3H_7N_2O^+[N_2]$-ct (**3**), 106 (96 – 112) kJ/mol [20]. Furthermore, IRMPD measurements suggest that the a_2^+ ion is a mixture of conformers with the cyclic species being the most abundant (55% or more) [39,40]. In both IRMPD studies, the comparison of

UU IR Author Manuscript

experimental and theoretical spectra may be flawed because several possible conformations were not included. These include $C_3H_7N_2O^+[N_1]$-ct and $C_3H_7N_2O^+[N_2]$-cc, which are likely to be formed in some yield in the decomposition of the b_2^+ ion as well as $CH_3C(O)NHCHNH_2^+$, which is the most stable of the $C_3H_7N_2O^+$ isomers examined here, lying 60 – 81 kJ/mol below c-$C_3H_7N_2O^+[N_1]$. This species can be derived from the cyclic isomer, as discussed further below. Although these species could contribute to the observed IRMPD spectrum, our comparison of the calculated one-photon IR spectra for these species with the experimental spectra does not change the conclusion that the cyclic species dominates. As we have suggested previously [24], the abundance of the cyclic isomer may be influenced by how the a_2^+ ions are formed. Upon initial dissociation from H^+GGG, if the product ions are formed at high energies or undergo further collisions, the additional energy could allow subsequent transformations of the initially formed conformations.

In contrast to the situation for H^+AMOx, the transition state for decarbonylation of H^+DKP, TS(H^+DKP[O_t-N]), lies well above the TS energies for rearrangement of the initially formed $C_3H_7N_2O^+[N_2]$-cc product, Table 4. Thus such rearrangements should be facile.

Theoretical Results for Decomposition of $C_3H_7N_2O^+$ (a_2^+)

As the collision energy increases, the initially formed $C_3H_7N_2O^+$ (a_2^+) ion can undergo further decomposition. This is obvious in Figure 1a where the a_2^+ cross section declines as the cross sections for formation of *m/z* 59 and 30 (a_1^+) ions increase, such that the total cross section behaves smoothly, leveling out above 3 eV. Similar behavior is found in Figure 1b, although here competition with other pathways makes the coupling between these pathways less distinct. Figure 2 shows the pathway for decomposition of a_2^+: $C_3H_7N_2O^+[N_2]$-ct passes over TS($C_3H_7N_2O^+[N_2]$-ct{C~OC~N}) (**3→14**), in which both bonds to the carbonyl are synchronously broken, 189 – 209 (**209**) kJ/mol above the H^+AMOx GS. This forms the proton bound dimer of CH_2NH where the carbonyl is bound to one of the carbon atoms, $H^+(CH_2NH)_2(OC_C)$ (**14**). Presumably the CO molecule can migrate to other positions, hydrogen

UU IR Author Manuscript

binding to CH or NH, where the latter species, $H^+(CH_2NH)_2(OC_{HN})$, is the lowest in energy, 8 – 10 kJ/mol lower than $H^+(CH_2NH)_2(OC_C)$, Figure 2. Detailed explorations of these transformations were not investigated because loss of CO to yield $H^+(CH_2NH)_2$ (*m/z* 59) (**15**) + CO requires only 6 – 12 (**6**) kJ/mol, 81 – 93 (**82**) kJ/mol *below* the TS. Indeed, subsequent decomposition of the proton bound dimer to form $CH_2NH_2^+$ (*m/z* 30, a_1^+) + CH_2NH lies only 19 – 28 (**29**) kJ/mol above the TS, 217 – 226 (**238**) kJ/mol above the H^+AMOx GS, Figure 2. Alternative pathways for decomposition of the a_2^+ product ion were also explored, but the same TS is located if decomposition of the cc conformer is examined; dissociation from the $[N_1]$ conformer cannot occur without proton transfer to $[N_2]$; and the cyclic isomer first rearranges to $C_3H_7N_2O^+[N_2]$-ct before decomposition, as also determined by Siu and coworkers [20]. The mechanism for decomposition of the $C_3H_7N_2O^+$ product formed from H^+DKP should be the same, as the initially formed $C_3H_7N_2O^+[N_2]$-cc species can readily rearrange to $C_3H_7N_2O^+[N_2]$-ct, Figure 4. Because H^+DKP is more stable than H^+AMOx by 7 – 12 kJ/mol, Table S2, the energies for all these species relative to the H^+DKP reactant will increase by this amount.

Theoretical Results for Decomposition of $C_4H_9N_2O^+$ (a_2^+)

As noted above, the $C_4H_9N_2O^+[N_2]$ product ion formed by decarbonylation of H^+MAMOx is originally formed in both the ctt and ctc conformations, with the former being lower in energy and having a lower energy TS for its formation. Decarbonylation of this trans isomer is also lower in energy, with TS($C_4H_9N_2O^+[N_2]$-ctt{C~OC~N}) (**3→5**) lying 171 – 199 (**191**) kJ/mol above the GS, whereas TS($C_4H_9N_2O^+[N_2]$-ctc{C~OC~N}) lies at 176 – 203 kJ/mol, Table 1. These TSs lie 122 – 133 and 116 – 124 kJ/mol above their respective a_2^+ ion, which is comparable to the value of 133 kJ/mol for the ctt isomer calculated by Harrison et al. at a B3LYP/6-31+G(d,p) level [37]. We find that the ctt and ctc TSs lead to slightly different proton bound complexes of $(C_2H_4NH)H^+(CH_2NH)$ in which the methyl group is either trans or cis, respectively, as indicated by the CCNH dihedral angle, where the H atom is involved in the hydrogen bond to CH_2NH. The former is lower in energy but only by 2 – 4 kJ/mol, and rotation

UU IR Author Manuscript

about the proton bond is much lower in energy than the TSs overcome to form these species. Formation of $C_2H_4NH_2^+$ + CH_2NH is 38 – 45 (**47**) kJ/mol lower in energy than formation of C_2H_4NH-t + $CH_2NH_2^+$, and formation of C_2H_4NH-c is 3 – 4 kJ/mol higher in energy.

The rate-limiting TS for decomposition of the a_2^+ (H^+GAG) ion, TS($C_4H_9N_2O^+[N_2]$-ctt{C~OC~N}) lies 5 – 18 (**18**) kJ/mol below the comparable TS in the H^+AMOx system, 4 – 7 (**3**) kJ/mol above the $C_2H_4NH_2^+$ + CH_2NH + CO asymptote, and 32 – 40 (**44**) kJ/mol below the $CH_2NH_2^+$ (a_1^+) + C_2H_4NH-t + CO asymptote. All of these relative energies are consistent with the data shown in Figures 1a and 1c, including the observation that once a_2^+ (H^+GAG) is decarbonylated to form the proton-bound complex at *m/z* 73, it rapidly decomposes to the $C_2H_4NH_2^+$ product ion, thereby limiting the yield of the complex.

Experimental Results for Sequential Decomposition of $C_3H_7N_2O^+$ (a_2^+) and $C_4H_9N_2O^+$ (a_2^+)

Our modeling of the experimental cross sections can be extended to the first sequential decomposition reaction of the a_2^+ primary products forming $H^+(CH_2NH)_2$ (*m/z* 59) in the b_2^+(H^+GGG) system, $H^+(CH_2NH)(C_2H_4NH)$ (*m/z* 73) in the b_2^+(H^+GAG) system, and competitive sequential formation of $H^+(CH_2NH)_2$ (*m/z* 59) and $CH_2NH_2^+$(CO) (*m/z* 58) in the H^+DKP system. Qualitatively, the mechanism elucidated in Figure 2 is consistent with the energy behavior of the higher energy products observed for decomposition of both b_2^+ ions, Figures 1a and 1c. Because the same $C_3H_7N_2O^+$ ion can be formed from H^+DKP, this mechanism is also appropriate for its subsequent decomposition to both $H^+(CH_2NH)_2$ (*m/z* 59) and $CH_2NH_2^+$(CO) (*m/z* 58), Figure 2, where the latter species is an adduct of carbon monoxide with $CH_2NH_2^+$. The energy dependence shown in Figure 1b is consistent with this as the cross section for this product has an apparent threshold slightly below that for the $CH_2NH_2^+$ product, but above that for $H^+(CH_2NH)_2$. On this basis, one might also expect to observe this species in the decomposition of H^+AMOx. Acquisition of accurate absolute reaction cross sections generally requires using low mass resolution conditions, but such conditions also inhibit the observation of weak product ions adjacent to more intense products ions, such as *m/z* 59. In the

UU IR Author Manuscript

case of H^+DKP, the possibility of the *m/z* 58 product was specifically looked for using altered experimental conditions, whereas such additional experiments were not performed in the case of H^+AMOx. It is possible that such an experiment would yield a similar cross section for the *m/z* 58 species as that in Figure 1b, although Siu and coworkers did not observe this product ion either [20]. As no quantitative information can be obtained from this minor product (see below), such an experiment was not pursued.

In modeling these data, the cross sections for formation of $H^+(CH_2NH)_2$ and $H^+(CH_2NH)(C_2H_4NH)$ are taken to be the sum of their cross sections and those for the subsequent dissociation to $CH_2NH_2^+$ and $C_2H_4NH_2^+$ (which is a slight overestimate in the H^+DKP system because the $CH_2NH_2^+(CO)$ product also decomposes to the $CH_2NH_2^+$ ion, although to a much smaller extent). Using the sequential dissociation model described in the Supplemental Information (which assumes a statistical distribution of internal and translation energies among the initial products, which are assumed to lie at the energy of the initial transition state), the threshold energies for formation of $H^+(CH_2NH)_2$, $H^+(CH_2NH)(C_2H_4NH)$, and $CH_2NH_2^+(CO)$ obtained are listed in Table S5. This analysis may not yield results directly comparable to theory because formation of the primary products in reactions (1), (4), and (7) occur over a tight TS, such that release of the CO is subject to the dynamics of the reactions (i.e., may not be statistical), may vary from system to system, and the product ion actually lies at a different energy than the model assumes (the energy of the TS). Indeed, Harrison and coworkers have shown that the fragmentations of the b_2^+ ions to form a_2^+ ions involving Gly and Ala residues have a kinetic energy release of 0.50 – 0.57 eV [1], consistent with the energy profile shown in Figure 2. Thus, energy is released preferentially in translation, leaving the primary a_2^+ ion with less internal energy, thereby shifting the observed threshold to energies above the calculated energy for subsequent dissociation.

To test the sensitivity of the results to the assumptions, we also analyzed these cross sections independently (i.e., ignoring formation of the lower energy precursor), although because these products involve formation of three species (loss of 2 CO or loss of CO + CH_2NH), the

energized molecule (EM) must then be the a_2^+ ion. The thresholds for the independent fits are systematically about 0.4 eV lower than those from the sequential modeling, Table S5. This difference can be understood by considering the RRKM expression of Eq. (S2). The number of states in the TS is the same at a particular collision energy and the EM for production of the secondary products is the a_2^+ primary product for both models, but assumptions about the energy available to the EM change the density of states in the denominator. When the secondary dissociation is treated as a primary process, the a_2^+ species is assumed to have the full collision energy, but when the sequential model is used, the energy required to overcome the TS is removed. Thus, the latter EM has a lower internal energy, a lower density of states, a higher dissociation rate according to Eq. (S2), which leads to a smaller kinetic shift and thus a higher threshold is measured using the sequential model. Because these two models give the a_2^+ ion close to the maximum and minimum amounts of energy possible, the kinetic shifts should represent upper and lower limits as well, but this presumes that a statistical model is applicable. As noted above, it is known that formation of the a_2^+ ion preferentially releases energy into translation, such that both measurements are shifted to higher energies than the true thresholds, making them both upper limits. Compared to the theoretical TS energies, these limits are substantially higher, Table 2, although the independent fits are 32 – 79 kJ/mol above the theoretical energies, comparable to the kinetic energy release of 48 – 55 kJ/mol measured by Harrison and coworkers [1]. Overall, these analyses of the data are flawed by the dynamics of the reactions involved, such that statistical theories are not appropriate for their analysis. Thus, the thresholds can be compared with theory only as upper limits, although the discrepancies do have approximately the correct magnitudes compared with the known kinetic energy release.

Modeling of the further decomposition of the secondary products to $CH_2NH_2^+$ and $C_2H_4NH_2^+$ requires consideration of two sequential dissociations, which is sufficiently complicated that such processes are not included in our data analysis software. However, relative thresholds can be obtained by starting with the independent fits of the $H^+(CH_2NH)_2$, $CH_2NH_2^+(CO)$, and $H^+(CH_2NH)(C_2H_4NH)$ secondary product cross sections, and then adding the

UU IR Author Manuscript

possibility that these species decompose in sequential reactions to form $CH_2NH_2^+$ and $C_2H_4NH_2^+$ over loose PSL TSs. In all cases, the absolute thresholds are again well above the theoretical values, Table 2, in part because they are still elevated by the known kinetic energy release associated with a_2^+ ion formation but also because in passing over the TS for formation of the proton-bound dimer products, even more kinetic energy can be released. Indeed, this second TS has a larger reverse activation barrier than the TS leading to a_2^+ formation, Figure 2.

If only relative energies are compared, we find that the thresholds for formation of $H^+(CH_2NH)_2$ (*m/z* 59) and $CH_2NH_2^+(CO)$ (*m/z* 58) in the H^+DKP system have identical thresholds within experimental error, consistent with the reaction coordinate surface of Figure 2 which indicates they are both limited by the same TS($C_3H_7N_2O^+[N_2]$-ct{C~OC~N}). Subsequent formation of $CH_2NH_2^+$ (*m/z* 30) has a threshold measured to lie 76 ± 18 kJ/mol above that for $H^+(CH_2NH)_2$ (*m/z* 59), whereas the theoretical difference between TS($C_3H_7N_2O^+[N_2]$-ct{C~OC~N}) and the $CH_2NH_2^+$ + CH_2NH + CO asymptote is 18 – 27 kJ/mol. A comparable result is obtained in the b_2^+ (H^+GGG) system where the threshold for a_1^+ (*m/z* 30) formation is measured to lie 41 ± 24 kJ/mol above that for $H^+(CH_2NH)_2$. These observations suggest that there may be considerable kinetic energy release upon passing over TS($C_3H_7N_2O^+[N_2]$-ct{C~OC~N}), consistent with the large reverse activation barrier calculated theoretically.

In the H^+GAG system, the analogous process is more difficult to model because of the small size of the cross section for the $H^+(CH_2NH)(C_2H_4NH)$ intermediate, however, a reasonable analysis finds that this cross section can be reproduced reasonably well when its threshold is the same as that for the subsequent decomposition to $C_2H_4NH_2^+$, which is consistent with the theoretical result that the latter asymptote lies below the TS energy, Table 1. In addition, this analysis finds that the $C_2H_4NH_2^+$ (*m/z* 44) and $CH_2NH_2^+$ (*m/z* 30) products have thresholds differing by 18 ± 4 kJ/mol, compared to the theoretical difference in the asymptotes of 38 – 45 kJ/mol, Table 2. However, as TS($C_4H_9N_2O^+[N_2]$-ctc{C~OC~N}) lies above the $C_2H_4NH_2^+$ + CH_2NH + 2 CO asymptote by 20 – 23 kJ/mol, the measured threshold for $C_2H_4NH_2^+$ should be

UU IR Author Manuscript

compared with this energy, which lies 28 – 32 kJ/mol below the $CH_2NH_2^+ + C_2H_4NH + 2\ CO$, more comparable to the 18 ± 4 kJ/mol measured difference.

Theoretical Results for Direct $b_2^+ \rightarrow a_1^+$ Decomposition

Siu and coworkers [20,21] interpreted their cross sections for formation of the a_1^+ product in terms of a direct dissociation from the b_2^+ parent. As noted above, the very similar shapes and magnitudes of the $C_2H_4NH_2^+$ and $CH_2NH_2^+$ cross sections in Figure 1c with each other and with that for $CH_2NH_2^+$ in Figure 1a indicates that these species are dominantly formed by similar mechanisms. This is consistent with the decomposition of the proton-bound $H^+(CH_2NH)(RCHNH)$ complex (where R = H or CH_3) but not with the direct $b_2^+ \rightarrow a_1^+$ mechanism outlined by Siu and coworkers (and further expanded in the Supplemental Information), as this mechanism cannot yield $C_2H_4NH_2^+$. Therefore interpretation of the threshold for appearance of the a_1^+ ion via this mechanism, whether in competition with a_2^+ formation or not, as suggested by Siu and coworkers, is inconsistent with our results. Harrison and coworkers reached the same conclusion for the methylated b_2^+ ion [6]. As detailed further in the Supplemental Information, we conclude that although direct $b_2^+ \rightarrow a_1^+$ decomposition may contribute to the total a_1^+ cross sections at high energies, it cannot be the primary pathway for its formation.

Theoretical Results for Alternate Decomposition Pathways of H^+DKP

H^+DKP is also observed to form a minor product ion at *m/z* 43 at higher energies. Computations indicate that the lowest energy structure of this ion is the acetyl cation (ketene protonated on the carbon), CH_3CO^+. This product can be formed by cleaving two bonds across the six-membered ring. Several pathways for this process were explored and include two possible neutral products, as shown in reactions (11) and (12).

$$C_4H_7N_2O_2^+ + Xe \rightarrow CH_3CO^+ + OCNH + CH_2NH + Xe \quad (11)$$

$$\rightarrow CH_3CO^+ + H_2NCHNH + CO + Xe \quad (12)$$

UU IR Author Manuscript

$$\rightarrow CH_2CO + OCNH + CH_2NH_2^+ + Xe \quad (13)$$

$$\rightarrow CH_2CO + H_2NCHNH_2^+ + CO + Xe \quad (14)$$

In both cases, the proton affinity of the nitrogen species is higher than that of ketene such that CH_3CO^+ must clearly be a minor decomposition pathway, consistent with the magnitude of its cross section. Calculations indicate that the products of reaction (11) lie above those of reaction (13) by 35 – 62 kJ/mol and that those for reactions (12) and (14) differ by 113 – 146 kJ/mol, Table S7. The former difference is sufficiently small that competition between the two pathways seems plausible, whereas the latter difference would be expected to yield very little CH_3CO^+. Furthermore, the $CH_2NH_2^+$ product is observed in Figure 1b, whereas the $H_2NCHNH_2^+$ product is not. Therefore, reaction (11) is a more likely pathway for CH_3CO^+ formation, but we explore mechanisms for both possibilities (with results for reactions (12) and (14) in Supplemental Information). Table S7 lists the energies of the various species involved.

The lowest energy route found for reaction (11) starts with $H^+DKP[O_c]$ and cleaves a CC and a CN bond across the ring to form the OCNH molecule along with $H^+CH_2CONHCH_2[O_c]$ protonated on the oxygen. The transition state for this cleavage, TS($H^+DKP[O_c]${C~C,C~N}), is 272 – 278 kJ/mol above the H^+DKP GS with the product asymptote at a much lower energy, 123 – 149 kJ/mol, such that loss of the OCNH should occur readily. However, the resultant ionic product at *m/z* 72 is not observed, possibly because its cross section is too small. This is consistent with the fact that decomposition of $H^+CH_2CONHCH_2[O_c]$ requires only another 27 – 82 kJ/mol. This involves cleavage of the CN bond by passing over the rate-limiting TS, TS($H^+CH_2CONHCH_2[O_c]${C~N}), lying 301 – 355 kJ/mol above H^+DKP GS. This can lead to both reactions (11) and (13) as these product asymptotes lie well below the TS energy (by 82 – 119 and 143 – 154 kJ/mol, respectively). Notably, formation of $CH_2NH_2^+ + CH_2CO + OCNH$ in reaction (13) is lower in energy than formation of $CH_2NH_2^+ + CH_2NH + 2\ CO$ (by 34 – 71 kJ/mol), the route discussed above. However, formation of the $CH_2NH_2^+$ product ion should be dominated by the latter pathway because it is limited by the product asymptote in a loose TS (at 228 – 236 kJ/mol), whereas reaction (13) must pass over two relatively high energy tight TSs

UU IR Author Manuscript

with the highest at 301 – 355 kJ/mol.

Analysis of the data for production of CH_3CO^+ is not easily performed because the mechanism outlined above requires a sequential dissociation pathway with the first intermediate (*m/z* 72) not observed. A rough idea of the threshold can be obtained by using the first TS instead, TS(H^+DKP[O_c]{C~C,C~N}). This leads to a threshold for formation of CH_3CO^+ that is about 58 ± 26 kJ/mol above that for decarbonylation, Table 2, the process with which it competes. Theory finds that the rate limiting TSs for these two pathways differ in energy by 74 – 131 kJ/mol, where the lower values (B3LYP) are in reasonable agreement with experiment.

Acknowledgement. This work is supported by the National Science Foundation, CHE-1049580. Abhigya Mookherjee is thanked for help with the experiments and Monica Heaton is thanked for early contributions to the calculations.

Appendix A. Supplementary Information

Supplementary information associated with this article can be found, in the online version, at doi: xxx.

References

[1] T. Yalcin, C. Khouw, I.G. Csizmadia, M.R. Peterson, A.G. Harrison, J. Am. Soc. Mass Spectrom. 6 (1995) 1165.

[2] T. Yalcin, I.G. Csizmadia, M.R. Peterson, A.G. Harrison, J. Am. Soc. Mass Spectrom. 7 (1996) 233.

[3] K. Ambihapathy, T. Yalcin, H.-W. Leung, A.G. Harrison, J. Mass Spectrom. 32 (1997) 209.

[4] M.J. Nold, C. Wesdemiotis, T. Yalcin, A.G. Harrison, Int. J. Mass Spectrom. Ion Processes 164 (1997) 137.

[5] M.J. Nold, B.A. Cerda, C. Wesdemiotis, J. Am. Soc. Mass Spectrom. 10 (1999) 1.

[6] A.G. Harrison, I.G. Csizmadia, T.-H. Tang, J. Am. Soc. Mass Spectrom. 11 (2000) 427.

[7] G.E. Reid, R.J. Simpson, R.A.J. O'Hair, J. Am. Soc. Mass Spectrom. 9 (1998) 945.

[8] B. Paizs, G. Lendvay, K. Vekey, S. Suhai, Rapid Commun. Mass Spectrom. 13 (1999) 525.

[9] S.H. Yoon, J. Chamot-Rooke, B.R. Perkins, A.E. Hilderbrand, J.C. Poutsma, V.H. Wysocki, J. Am. Chem. Soc. 130 (2008) 17644.

[10] J. Oomens, S. Young, S. Molesworth, M.J. van Stipdonk, J. Am. Soc. Mass Spectrom. 20 (2009) 334.

[11] X. Chen, L. Yu, J.D. Steill, J. Oomens, N.C. Polfer, J. Am. Chem. Soc. 131 (2009) 18272.

[12] X. Chen, J.D. Steill, J. Oomens, N.C. Polfer, J. Am. Soc. Mass Spectrom. 21 (2010) 1313.

[13] D. Wang, K. Gulyuz, C.N. Stedwell, N.C. Polfer, J. Am. Soc. Mass Spectrom. 22 (2011) 1197.

[14] R.K. Sinha, U. Erlekam, B.J. Bythell, B. Paizs, P. Maître, J. Am. Soc. Mass Spectrom. 22 (2011) 1645.

[15] N.C. Polfer, J. Oomens, S. Suhai, B. Paizs, J. Am. Chem. Soc. 127 (2005) 17154.

[16] B.R. Perkins, J. Chamot-Rooke, S.H. Yoon, A.C. Gucinski, A. Somogyi, V.H. Wysocki, J. Am. Chem. Soc. 131 (2009) 17528.

[17] C.W. Tsang, A.G. Harrison, J. Am. Chem. Soc. 98 (1976) 1301.

[18] J.S. Klassen, P. Kebarle, J. Am. Chem. Soc. 119 (1997) 6552.

[19] J. Laskin, E. Denisov, J.H. Futrell, J. Am. Chem. Soc. 122 (2000) 9703.

[20] H. El Aribi, C.F. Rodriquez, D.R.P. Almeida, Y. Ling, W.W.-N. Mak, A.C. Hopkinson, K.W.M. Siu, J. Am. Chem. Soc. 125 (2003) 9229.

[21] H. El Aribi, G. Orlova, C.F. Rodriquez, D.R.P. Almeida, A.C. Hopkinson, K.W.M. Siu, J. Phys. Chem. B 108 (2004) 18743.

[22] S. Abirami, Y.M. Xing, C.W. Tsang, N.L. Ma, J. Phys. Chem. A 109 (2005) 500.

[23] P.B. Armentrout, A.L. Heaton, S.J. Ye, J. Phys. Chem. A. (2011) in press.

[24] P.B. Armentrout, A.L. Heaton, J. Am. Soc. Mass Spectrom. (2011) in press.

[25] P.B. Armentrout, A.L. Heaton, J. Am. Soc. Mass Spectrom. (2011) in press.

UU IR Author Manuscript

[26] K.M. Ervin, P.B. Armentrout, J. Chem. Phys. 83 (1985) 166.

[27] F. Muntean, P.B. Armentrout, J. Chem. Phys. 115 (2001) 1213.

[28] R.M. Moision, P.B. Armentrout, J. Am. Soc. Mass Spectrom. 18 (2007) 1124.

[29] R.M. Moision, P.B. Armentrout, J. Phys. Chem. A 106 (2002) 10350.

[30] A.L. Heaton, R.M. Moision, P.B. Armentrout, J. Phys Chem. A 112 (2008) 3319.

[31] A.L. Heaton, P.B. Armentrout, J. Phys. Chem. B 112 (2008) 12056.

[32] D.R. Carl, R.M. Moision, P.B. Armentrout, J. Am. Soc. Mass Spectrom. 20 (2009) 2312.

[33] M.T. Rodgers, K.M. Ervin, P.B. Armentrout, J. Chem. Phys. 106 (1997) 4499.

[34] M.T. Rodgers, P.B. Armentrout, J. Chem. Phys. 109 (1998) 1787.

[35] P.B. Armentrout, J. Chem. Phys. 126 (2007) 234302.

[36] A.L. Heaton, P.B. Armentrout, J. Am. Soc. Mass Spectrom. 20 (2009) 852.

[37] A.G. Harrison, A.B. Young, M. Schnoelzer, B. Paizs, Rapid Commun. Mass Spectrom. 18 (2004) 1635.

[38] B. Balta, V. Aviyente, C. Lifshitz, J. Am. Soc. Mass Spectrom. 14 (2003) 1192.

[39] U.H. Verkerk, C.-K. Siu, J.D. Steill, H. El Aribi, J. Zhao, C.F. Rodriguez, J. Oomens, A.C. Hopkinson, K.W.M. Siu, J. Phys. Chem. Lett. 1 (2010) 868.

[40] B.J. Bythell, P. Maitre, B. Paizs, J. Am. Chem. Soc. 132 (2010) 14766.

UU IR Author Manuscript

Table 1. Relative theoretical energies (kJ/mol) at 0 K of H^+AMOx and H^+MAMOx fragmentation intermediates, products, and transition states (imaginary frequencies, cm^{-1})

Species	B3LYP[a]	B3LYP// B3LYP[a]	MP2(full) //B3LYP[a]	Literature[b]	imag freq
H^+AMOx[N_2]-c / H^+MAMOx[N_2]-c	0.0	0.0	0.0	0.0 (**1**)	
TS(H^+AMOx[N_2]-c{OC~O})	127.8	131.7	126.4	137.7 (**1**→**2**)	338
TS(H^+MAMOx[N_2]-ctt{OC~O})	116.2	119.5	119.1		347
TS(H^+MAMOx[N_2]-ctg{OC~O})	125.4	129.1	126.9	125.1 (**1**→**2**)	345
TS(H^+AMOx[N_1]-c{OC~O})	151.4	154.4	147.1		386
TS(H^+MAMOx[N_1]-ctt{OC~O})	141.5	144.3	146.5		347
TS(H^+MAMOx[N_1]-ctg{OC~O})	148.2	151.1	151.6		336
c-$C_3H_7N_2O^+$[N_1] + CO	50.8	55.4	41.9	59.4 (**4**)	
$C_4H_9N_2O^+$[N_2]-ctt + CO	46.9	51.4	66.2		
$C_4H_9N_2O^+$[N_2]-ctc + CO	59.0	63.8	79.1	57.7 (**3**)	
TS($C_3H_7N_2O^+$[N_2]-ct{C~OC~N}) + CO	189.2	192.4	208.5	208.8 (**3**→**14**)	190
TS($C_4H_9N_2O^+$[N_2]-ctt{C~OC~N}) + CO	171.1	173.6	199.4	190.8 (**3**→**5**)	168
TS($C_4H_9N_2O^+$[N_2]-ctc{C~OC~N}) + CO	176.5	179.6	203.1		219
$H^+(CH_2NH)_2$ + 2 CO	106.8	111.3	115.8	126.4 (**15**)	
$(C_2H_4NH)H^+(CH_2NH)$-t + 2 CO	72.7	76.0	94.9	115.9 (**5**)	
$(C_2H_4NH)H^+(CH_2NH)$-c + 2 CO	76.4	79.7	97.4		
$CH_2NH_2^+$ + CH_2NH + 2 CO	216.7	218.2	227.4	238.1	
$C_2H_4NH_2^+$ + CH_2NH + 2 CO	166.5	166.8	193.4	187.9	
$CH_2NH_2^+$ + C_2H_4NH-t + 2 CO	210.6	211.9	231.3	234.7	
$CH_2NH_2^+$ + C_2H_4NH-c + 2 CO	214.0	215.0	234.8		

[a] Values from the present study at the B3LYP/6-311+G(d,p), B3LYP/6-311+G(2d,2p)// B3LYP/6-311+G(d,p), and MP2(full)/6-311+G(2d,2p)//B3LYP/6-311+G(d,p) levels of theory.

[b] B3LYP/6-31++G(d,p) values from Siu and coworkers [20,21]. Designations in parentheses are the names used by these authors.

TABLE 2: Experimental and Theoretical Reaction Energies for Decomposition of H^+DKP and b_2^+ Ions (kJ/mol)

Reaction	Reactant	Products	TS[a]	Expt		Theory[d]	
				This work[b]	Lit.[c]	B3LYP	MP2
4	H^+DKP	$C_3H_7N_2O^+$ + CO	H^+DKP[O_t-N]	209 (18)		231	224
			H^+DKP[O_c-N]			255	237
6		CH_3CO^+ + OCNH + CH_2NH	TS($H^+CH_2CONHCH_2$[O_c]{C~N})	~267 (20)		305	355
1	b_2^+ (H^+GGG)	a_2^+ + CO	H^+AMOx[N_2]-c{OC~O}	151 (12)	140 (24)	132	126
			H^+AMOx[N_1]-c{OC~O}			154	147
7	b_2^+ (H^+GAG)	a_2^+ + CO	H^+MAMOx[N_2]-ctg{OC~O}	139 (10)	125 (18)	120	119
			H^+MAMOx[N_2]-ctt{OC~O}			129	127
			H^+MAMOx[N_1]-ctt{OC~O}			144	146
			H^+MAMOx[N_1]-ctg{OC~O}			151	152
2	H^+DKP	$H^+(CH_2NH)_2$ + 2 CO	$C_3H_7N_2O^+$[N_2]-ct{C~OC~N}	<249 (16)		204	216
5		$CH_2NH_2^+$(CO) + CH_2NH + CO	$C_3H_7N_2O^+$[N_2]-ct{C~OC~N}	<255 (16)		204	216
3a		$CH_2NH_2^+$ + CH_2NH + 2 CO	PSL	<325 (12)		230	235
2	b_2^+ (H^+GGG)	$H^+(CH_2NH)_2$ + 2 CO	$C_3H_7N_2O^+$[N_2]-ct{C~OC~N}	<241 (30)		192	209
3a		a_1^+ + CH_2NH + 2 CO	PSL	<282 (40)		218	227
3b		a_1^+ + c-$C_3H_3NO_2$	H^+AMOx [N_2]-g_t(C~C)	219 (40)	163 (20)[e]	164	189
8	b_2^+ (H^+GAG)	$H^+(CH_2NH)(C_2H_4NH)$ + 2 CO	$C_4H_9N_2O^+$[N_2]-ctt{C~OC~N}	<253 (8)		174	199
			$C_4H_9N_2O^+$[N_2]-ctc{C~OC~N}			180	203
9a		$C_2H_4NH_2^+$ + CH_2NH + 2 CO	PSL	<263 (28)		167	193
10a		a_1^+ + C_2H_4NH + 2 CO	PSL	<281 (28)		212	231

[a] PSL = loose phase space limit. [b] Present experimental values from Table S5 with uncertainties (2 standard deviations) in parentheses. [c] Experimental values from Siu and coworkers [20,21]. [d] Present calculations from Tables 1, S2, S4, and S6. [e] These authors also report a value of 178 ± 22 kJ/mol when no competition is included.

Figure Captions

Figure 1. Cross sections for collision-induced dissociation of the b_2^+ product ion formed by decomposition of H^+GGG (part a), H^+DKP (part b), and the b_2^+ product ion formed by decomposition of H^+GAG (part c) with Xe as a function of kinetic energy in the center-of-mass (lower *x*-axis) and laboratory frames (upper *x*-axis).

Figure 2. Reaction coordinate surface for CO loss from H^+AMOx and subsequent fragmentation. Geometry optimizations and single point energies of each elementary step are determined at the B3LYP/6-311+G(d,p) level of theory and corrected for ZPE. Short dashed lines indicate hydrogen bonds and longer dashed lines show bonds that are breaking or particularly weak interactions. The inset and additional horizontal bar indicate an alternative rate-limiting transition state for the initial decarbonylation.

Figure 3. Reaction coordinate surface for CO loss from H^+DKP. Geometry optimizations and single point energies of each elementary step are determined at the B3LYP/6-311+G(d,p) level of theory and corrected for ZPE. Short dashed lines indicate hydrogen bonds and longer dashed lines show bonds that are breaking or particularly weak interactions. The inset and additional horizontal bar indicate an alternative rate-limiting transition state.

Figure 4. Reaction coordinate surface for rearrangement of the $C_3H_7N_2O^+$ (a_2^+) product ion. Geometry optimizations and single point energies of each elementary step are determined at the B3LYP/6-311+G(d,p) level of theory and corrected for ZPE. Dashed lines show the energies of the transition states leading to the $C_3H_7N_2O^+$ (a_2^+) ion from H^+AMOx and H^+DKP.

UU IR Author Manuscript

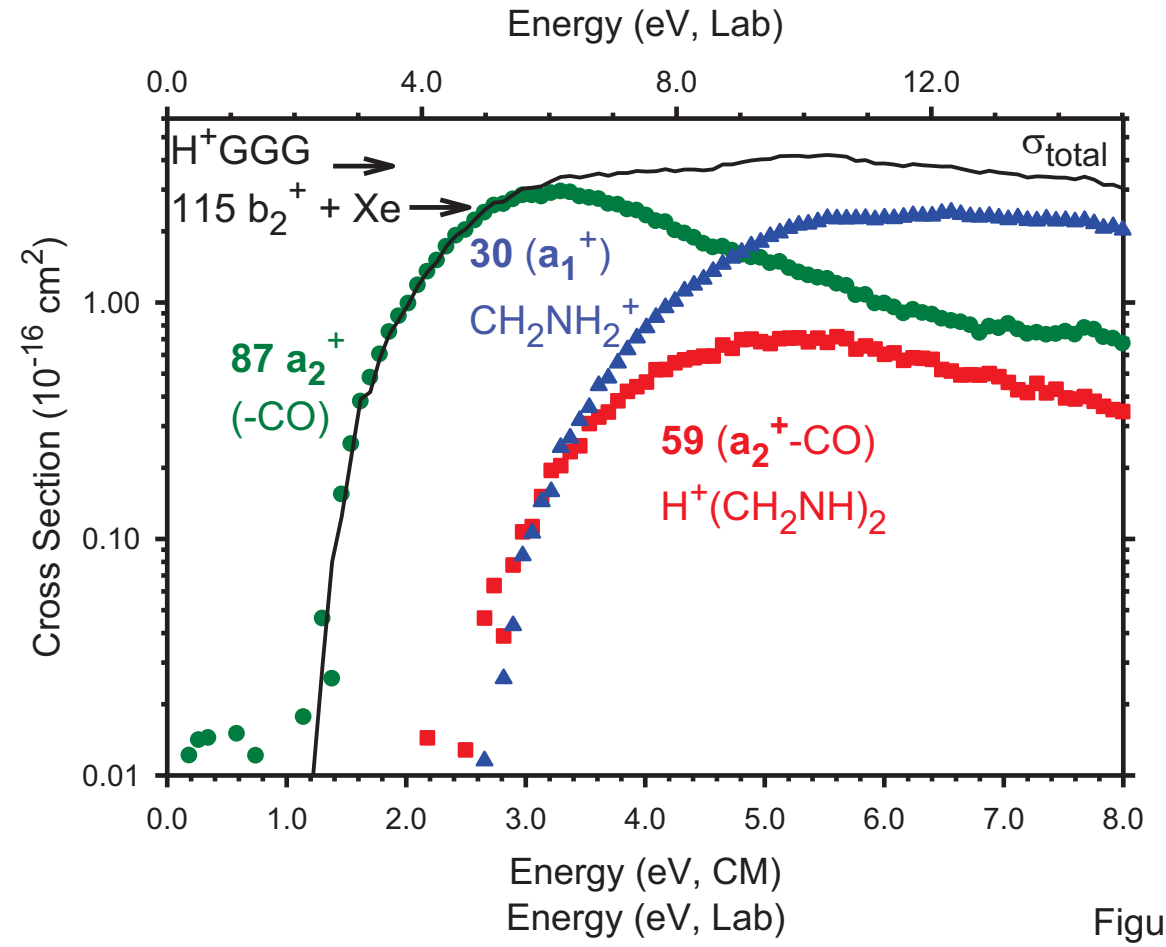

Figure 1a

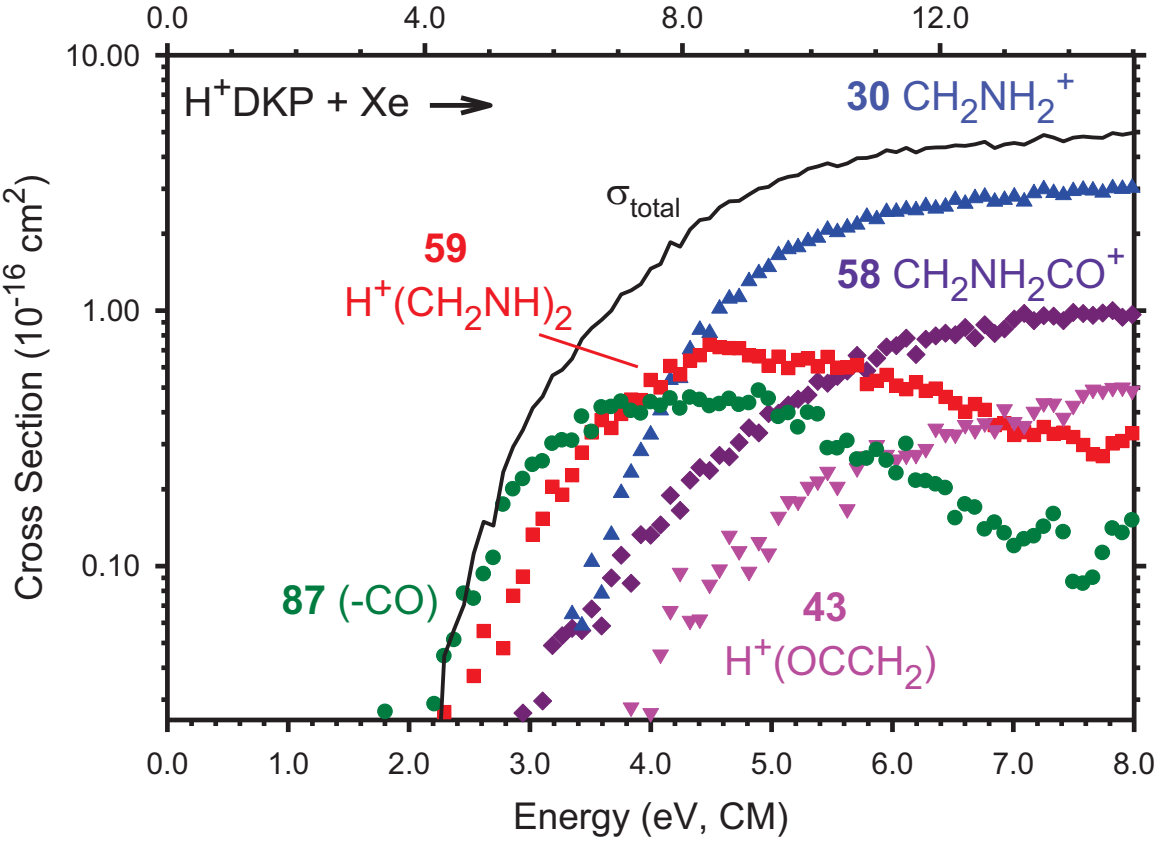

Figure 1b

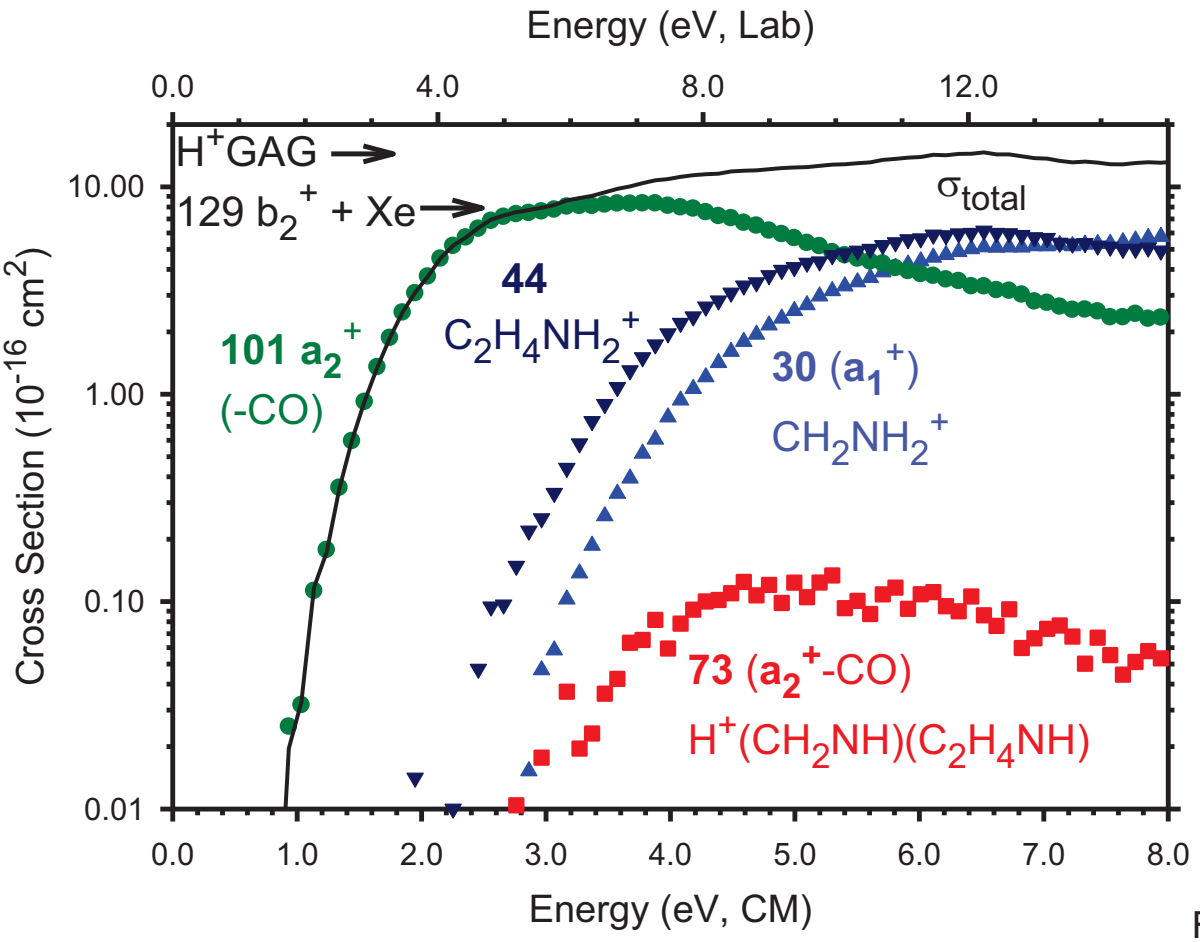

Figure 1c

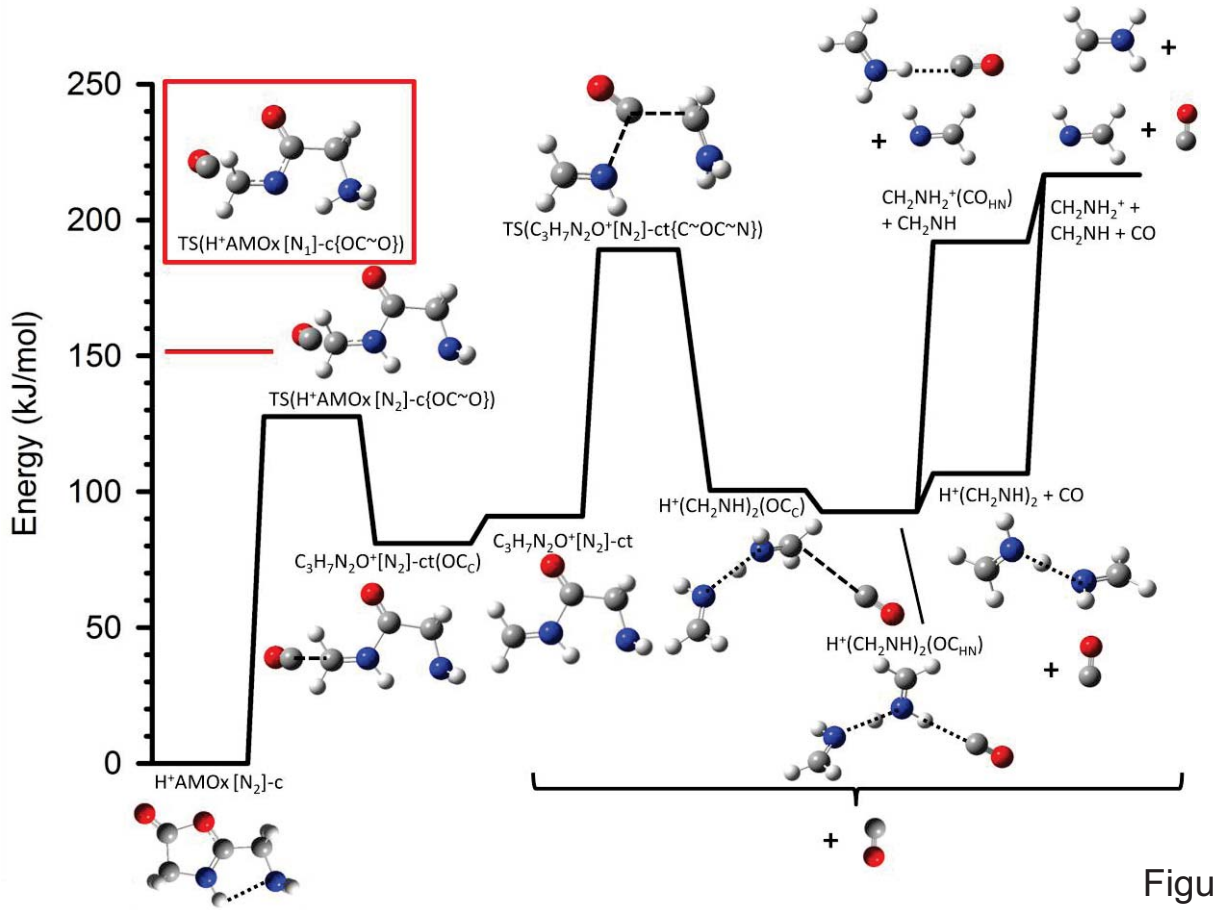

Figure 2

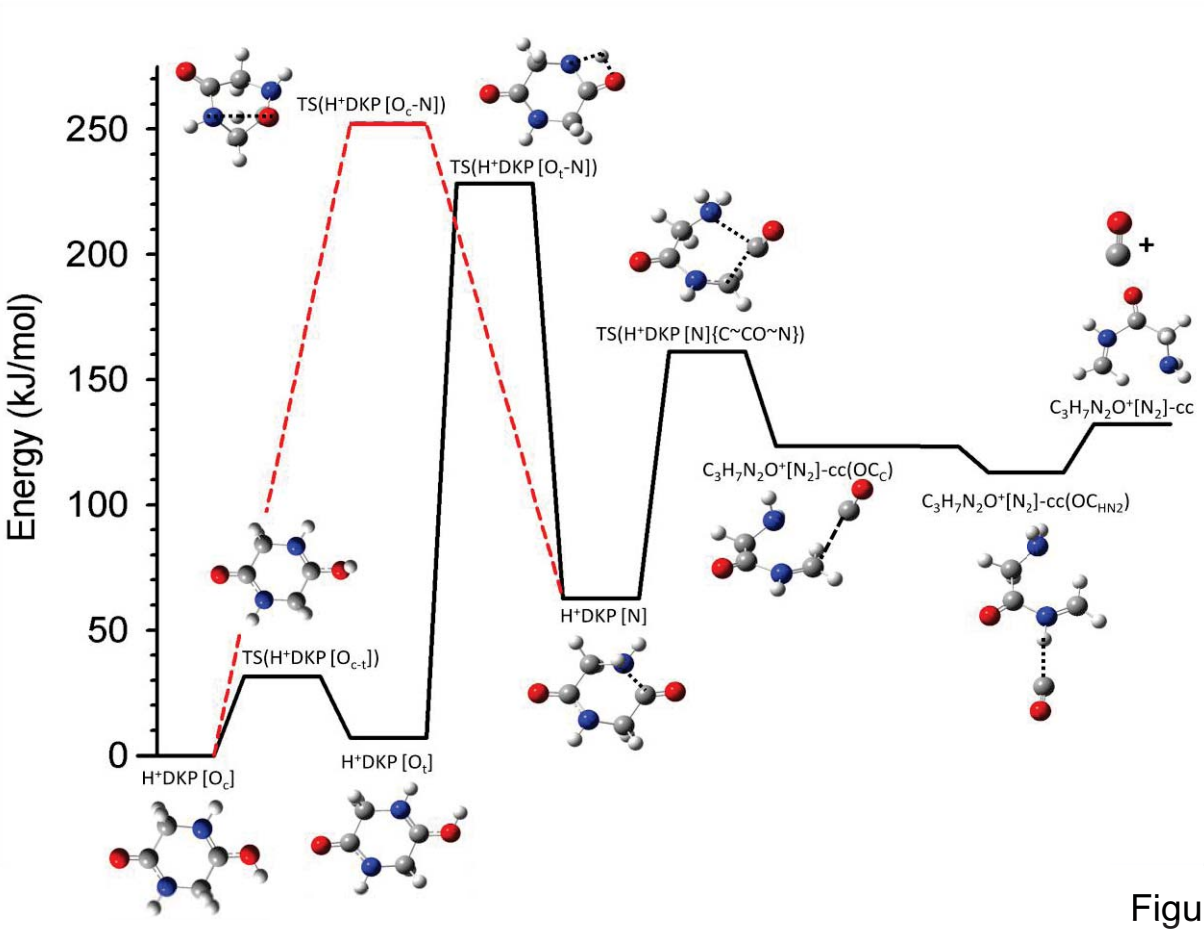

Figure 3

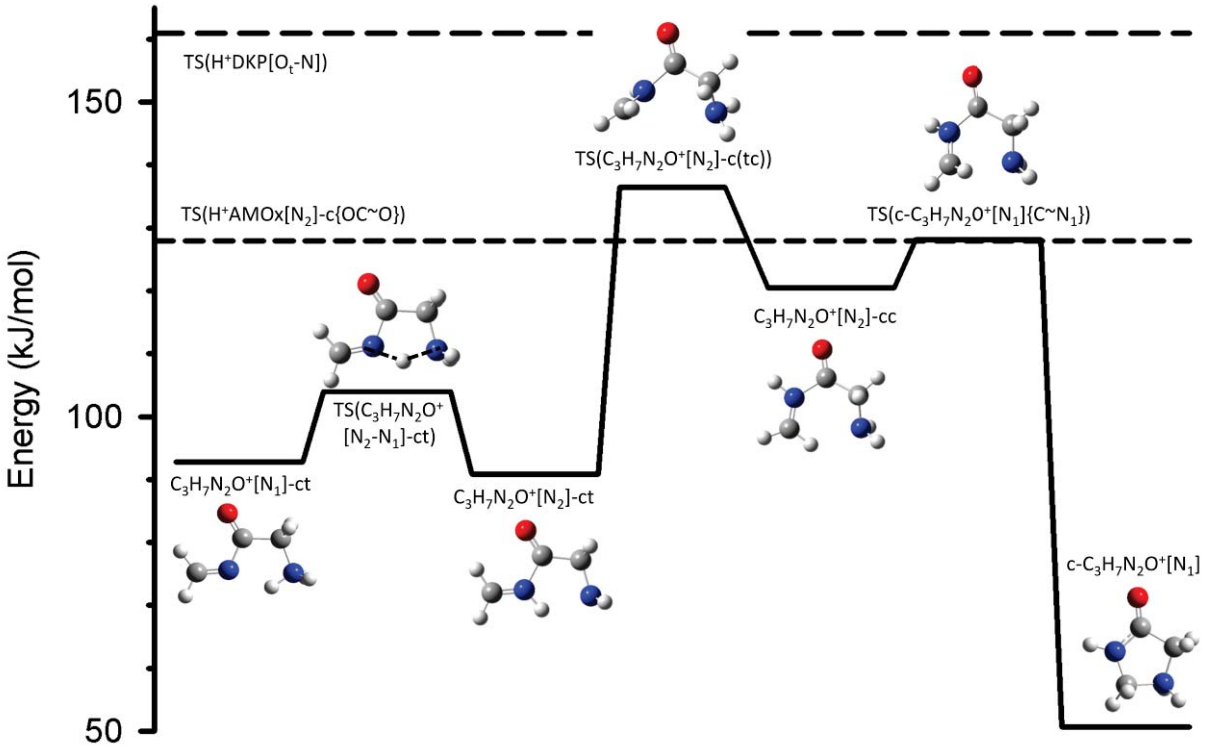

Figure 4

Supplementary Information

for

The Simplest b_2^+ Ion: Determining Its Structure from Its Energetics by a Direct Comparison of the Threshold Collision-induced Dissociation of Protonated Oxazolone and Diketopiperazine

by P. B. Armentrout and Amy A. Clark

Analysis of previous experiments

Siu and coworkers [1] suggest they operate under single collision conditions by stating that at their highest collision gas pressures "an ion that has a collision cross-section of 100 Å^2 will have, on average, undergone one collision in q2 with argon", where q2 designates their rf only quadrupole collision region. Calculations indicate that this statement means that 50% of the ions undergo one collision and 50% undergo no collisions. What this definition fails to recognize is that subsequent collisions can also occur. Presuming that the cross section remains at 100 Å^2 for subsequent reaction collisions, 25% of all ions undergo only one collision, 12% undergo two collisions, 6% undergo three collisions, and 6% undergo more collisions. Generally, in our laboratory, "single collision conditions" refer to a pressure where <10% of the ions undergo one collision, such that only 1% undergo more than one collision. This makes corrections for multiple collisions straightforward to achieve. In order to reach true "single collision conditions" for a cross section of 100 Å^2, Siu and coworkers would need to operate what they call their CGT (collision-gas thickness, or $n\ell$, where n is the number density of the collision gas and ℓ is the length of the collision cell) at 10^{13} atoms/cm^2, which is one order of magnitude smaller than their largest CGT and a factor of 2.5 smaller than the smallest CGT utilized. In truth, the cross sections for these ions are unlikely to be this large such that larger CGT values can be used and still correspond to single collision conditions. In the present system, our TCID data are collected at CGT values of approximately 50, 25, and 12 × 10^{12} atoms/cm^2, or half the values used by Siu and coworkers, where contributions from three or more collisions are negligible.

By operating in this higher pressure regime, their ions are undergoing extensive

scattering because of multiple collisions. Also contributing to the loss of ions (reactants and products) will be the lower trapping efficiency of the quadratic radial trapping field in a quadrupole (compared to the octopole trapping field which varies as the sixth power of the radius) [2,3]. Such effects may mean that a simple exponential fit of the pressure data (which they use to extrapolate their data to zero pressure) is not accurate. These considerations explain two observations made in the paper of Siu and coworkers. 1) The authors state they did not use Xe as a collision gas because the data are too scattered. As we have shown several times [4,5], collisions with Xe deposit energy more efficiently than those with Ar, such that the CID cross sections rise more rapidly, leading to more easily interpreted thresholds. This is because Xe is more massive and polarizable such that the collision is longer-lived and intrinsically more likely. At the higher pressures used by Siu and coworkers, this enhanced collision probability, coupled with the quadratic radial trapping field of a quadrupole, apparently leads to excessive loss of their ions, leading to smaller signals and more scattered data. Use of the lighter Ar allows the scattering to occur in a more forward laboratory direction such that more ions are observed, even though the efficiency of the energy transfer and thus the fragmentation is reduced. 2) The cross section reported for dissociation of H^+GGG with Ar is anomalously large, nearly 200 $Å^2$ at 4 eV. Such a cross section corresponds to the Langevin-Gioumousis-Stevenson (LGS) collision cross section with Ar at the very low energy of 0.01 eV. At 4 eV, the LGS cross section with Ar is 10 $Å^2$, but at these energies, the size of the ion is important such that a hard sphere (HS) cross section is a better estimate. A generous estimate of the hard sphere cross section for H^+GGG + Ar (averaged over various orientations of the ion) using the theoretically calculated ground state structure is 100 $Å^2$ (and even for the static orientation giving the maximum profile, it's only 140 $Å^2$). However, this can only correspond to the observed cross section if *every* collision leads to dissociation. For a process that is endothermic, grazing collisions (which are included in this hard sphere estimate) cannot possibly cause dissociation, such that these estimates are upper limits. A simple line-of-centers estimate for a process that is endothermic by 1.37 eV (as reported by Siu and coworkers for this process) indicates that only 66% (= 1 - E_0/E) of the HS

collisions can supply enough energy to induce dissociation at 4 eV. Even this estimate is too large because of kinetic shifts, which would reduce the effective cross section to 30% of the HS cross section (estimated using the threshold energy reported by Siu and coworkers). Indeed, measurements in our laboratory of the cross section for dissociation of H^+GGG + Xe (which should have a slightly larger hard-sphere cross section than Ar) obtain a maximum cross section for the b_2^+ fragment ion of ~10 $Å^2$ at ~3 eV (along with appreciable amounts of the y_2^+ fragment and minor amounts of six other products, none of which are reported by Siu and coworkers).[6] We believe that the b_2^+ cross section observed by Siu and coworkers is too large (by over an order of magnitude) because reactant ions are being lost because of scattering, inflating the apparent cross section for dissociation. However, this also means that product ions are likely to be lost to scattering as well (in part because they move more slowly than the reactant ions and therefore spend more time in the collision cell). Coupled with inaccurate extrapolation to zero pressure conditions (noted above) and the inefficient quadratic radial trapping field of a quadrupole, these factors affect the shape of the cross section measured, which may obscure the correct threshold dependence. Unfortunately, such possibilities cannot be checked easily as no fitting parameters for the cross sections are reported in this paper except for the threshold energies. Hence the shape and magnitudes of the cross sections measured cannot be reproduced except for the single case shown ($H^+GGG + Ar \rightarrow b_2^+$).

It can also be noted that the kinetic energy distribution of the ions in this study are substantially broader (FWHM = 2 eV in the laboratory frame) than those obtained here (0.1 – 0.2 eV). This is partly a consequence of the quadratic radial trapping field, which distorts the energy distribution of the ions, but may also reflect source conditions. Such broadening will spread out the onset for fragmentations. Coupled with the more inefficient dissociation probability, these effects lead to a very slow onset for the dissociation threshold. Indeed comparison of the reported cross section for $H^+GGG + Ar \rightarrow b_2^+$ compared to our own data using Xe shows their apparent dissociation onset is shifted to higher energies by about 1.0 eV.

The difficulty with modeling slowly rising cross sections is that the *n* parameter of Eq.

UU IR Author Manuscript

(S1), see below, is necessarily large, with the optimum value used depending critically on the range of data chosen for reproduction. In such cases, a large range of n values can be used to reproduce the data with a commensurate large range of threshold energies (larger n leading to smaller E_0 values). In our modeling procedure, the uncertainty in the value of n reported includes the range of values capable of reproducing the data and propagates to resultant variations in the threshold energies. Although the discussion of systematic uncertainties applied by the Siu group is extensive, this discussion does not include such variations, and the range of n values applied is not provided for any system.

General Experimental Procedures

The electrospray ionization (ESI) source [7-10] is operated using a 50:50 by volume H_2O/MeOH solution with ~10^{-4} M GGG, GAG, or DKP and ~10^{-4} M acetic acid (all chemicals purchased from Sigma-Aldrich), syringe-pumped at a rate of 0.04 mL/hr into a 35 gauge stainless steel needle biased at ~2000 V. Ionization occurs over the ~5 mm distance from the tip of the needle to the entrance of the capillary, biased at ~35 V. Ions are directed by a capillary heated to 80 °C into a radio frequency (rf) ion funnel [11], wherein they are focused into a tight beam. Ions exit the ion funnel and enter an rf hexapole ion guide that traps them radially. To generate b_2^+ ions, H^+GGG or H^+GAG is dissociated using an in-source fragmentation technique that uses electrodes placed between the hexapole rods [12]. These b_2^+ and H^+DKP ions undergo multiple collisions (>10^4) with the ambient gas in the hexapole and become thermalized. In either case, ions emitted from the source are assumed to have internal energies described by a Maxwell-Boltzmann distribution of rovibrational states at 300 K, as characterized in previous experiments [7,9,10,12-16].

Ions are extracted from the source and mass selected using a magnetic momentum analyzer. The mass-selected ions are decelerated to a well-defined kinetic energy and focused into a rf octopole ion guide that traps the ions radially [17,18]. The ion guide minimizes losses of the reactant and any product ions resulting from scattering. The octopole passes through a

static gas cell containing xenon, which is used as the collision gas for reasons described elsewhere [4,19]. After collision, the reactant and product ions drift to the end of the octopole where they are extracted and focused into a quadrupole mass filter for mass analysis. The ions are detected with a high voltage dynode, scintillation ion detector [20] and the signal is processed using standard pulse counting techniques.

Ion intensities, measured as a function of collision energy, are converted to absolute cross sections as described previously [21]. Product branching ratios are calculated from the absolute cross sections. The uncertainty in these relative cross sections is about ±5% and that for the absolute cross sections is about ±20%. The ion kinetic energy distribution is measured to be Gaussian and has a typical fwhm of 0.1 – 0.2 eV (lab). Uncertainties in the absolute energy scale are about ±0.05 eV (lab). Ion kinetic energies in the laboratory (lab) frame are converted to energies in the center-of-mass (CM) frame using $E_{CM} = E_{lab}\, m/(m+M)$, where M and m are the masses of the ionic and neutral reactants, respectively.

Thermochemical Analysis

Threshold regions of the CID reaction cross sections are modeled using Eq. (S1),

$$\sigma_j(E) = (n\sigma_{0,j}/E)\sum g_i \int_{E_{0,j}-E_i}^{E} [k_j(E^*)/k_{tot}(E^*)]\{1-e^{-k_{tot}(E^*)\tau}\}(E-\varepsilon)^{n-1} d(\varepsilon) \qquad \text{(S1)}$$

where $\sigma_{0,j}$ is an energy-independent scaling factor for channel j, n is an adjustable parameter that describes the efficiency of collisional energy transfer [22], E is the relative kinetic energy of the reactants, $E_{0,j}$ is the threshold for dissociation of the ground electronic and rovibrational state of the reactant ion at 0 K for channel j, τ is the experimental time for dissociation (~5×10^{-4} s in the extended dual octopole configuration as measured by time-of-flight studies [22]), ε is the energy transferred from translation during the collision, and E^* is the internal energy of the energized molecule (EM) after the collision, i.e., $E^* = \varepsilon + E_i$. The summation is over the rovibrational states of the reactant ions, i, where E_i is the excitation energy of each state and g_i is the fractional population of those states ($\sum g_i = 1$). The Beyer-Swinehart algorithm [23-25] is used to evaluate

the number and density of the rovibrational states and the relative populations g_i are calculated for a Maxwell-Boltzmann distribution at 300 K. The term $k_j(E^*)$ is the unimolecular rate coefficient for dissociation of the EM to product channel j. The rate coefficients $k_j(E^*)$ and $k_{tot}(E^*)$ are defined by Rice–Ramsperger–Kassel–Marcus (RRKM) theory as in Eq. (S2) [26,27],

$$k_{tot}(E^*) = \sum_j k_j(E^*) = \sum_j d_j N_j^{\dagger}(E^* - E_{0,j}) / h\rho(E^*) \quad \text{(S2)}$$

where d_j is the reaction degeneracy of channel j, $N^{\dagger}_j(E^* - E_{0,j})$ is the sum of rovibrational states of the transition state (TS) for channel j at an energy $E^* - E_{0,j}$, and $\rho(E^*)$ is the density of states of the EM at the available energy, E^*. These rate coefficients allow both kinetic shifts and competition between multiple parallel channels to be modeled [28,29].

The decompositions studied here involve sequential dissociation pathways, for which accurate modeling requires additional assumptions, as described previously [30]. The difficulty in analyzing sequential thresholds lies in the fact that the initial dissociation process takes away an unknown distribution of energies in translational modes of the initial products, as well as internal modes of the neutral product. This leaves an unknown distribution of internal energies in the ionic product that undergoes further dissociation. The procedure used to handle this effect uses Eq. (S1) to reproduce the cross section for the product of the primary reaction, which excludes subsequent dissociation, $\sigma_{CID}(E)$, combined with the probability for further dissociation, $P_{D2} = 1 - \exp[-k_{2tot}(E_2^*)\tau_2]$. Here k_{2tot}, E_2^*, and τ_2 are the total rate coefficient for the secondary dissociation, the energy available to the secondary EM, and the time available for the secondary dissociation, respectively. This partitions the total CID cross section into that for the non-dissociating products, σ_1, and that for the sequential dissociation product ion, σ_2, as described in Eq. (S3).

$$\sigma_1(E) = \sigma_{CID}(E)(1 - P_{D2}) \quad \text{(S3a)}$$

$$\sigma_2(E) = \sigma_{CID}(E)P_{D2} \quad \text{(S3b)}$$

Here, the rate coefficients are again calculated using RRKM theory, Eq. (S2), for the new EM. The energy available to this EM is defined statistically, accomplished by methods described in

UU IR Author Manuscript

detail elsewhere [30], and recently extended to multiple sequential channels [31]. The combination of sequential and competitive modeling generally allows accurate reproduction of all experimental reaction cross sections.

Several effects that obscure the interpretation of the data must be accounted for during data analysis in order to produce accurate thermodynamic information. The first effect involves energy broadening resulting from the thermal motion of the neutral collision gas and the kinetic energy distribution of the reactant ion. This is accounted for by explicitly convoluting the model over both kinetic energy distributions, as described elsewhere in detail [21]. The second effect considers that Eq. (S1) only models cross sections that represent products formed as the result of a single collision event. To ensure rigorous single collision conditions, data are collected at three pressures of Xe, generally about 0.20, 0.10, and 0.05 mTorr, and the resulting cross sections evaluated for pressure effects and extrapolated to zero pressure when necessary [32]. The third effect arises from the lifetime for dissociation, which leads to a delayed onset for the CID threshold, a kinetic shift, which becomes more noticeable as the size of the molecule increases. These kinetic shifts are estimated by the incorporation of RRKM theory as shown in Eq. (S1) and as described in detail elsewhere [28]. To evaluate the rate coefficient in Eq. (S1), sets of rovibrational frequencies for the EM and all TSs are required and are taken from quantum chemical calculations detailed in the next section. The transitional frequencies for loose TSs are treated as rotors, a treatment that corresponds to a phase space limit (PSL), as described in detail elsewhere [28,29]. The 2D external rotations in these cases are treated adiabatically but with centrifugal effects included [25], and the adiabatic 2D rotational energy is treated using a statistical distribution with an explicit summation over all the possible values of the rotational quantum number [28,29]. For reactions where a tight TS is required, all molecular parameters are taken from theoretical results. Although originally developed primarily for systems with loose TSs, we have demonstrated that this modeling procedure is capable of accurately reproducing threshold information for tight TSs [33], as well as competition between loose and tight TSs [14,34,35]. We additionally determine the entropy of activation for each dissociation

UU IR Author Manuscript

channel as described in detail elsewhere [29]. These $\Delta S^{\ddagger}$ quantities, which are energy (or temperature) dependent, are tabulated at 1000 K.

The model cross sections of Eq. (S1) and (S3) are convoluted with the kinetic energy distribution of the reactants [21] and compared to the data. A nonlinear least-squares analysis is used to provide optimized values for $\sigma_{0,j}$, n, and $E_{0,j}$. The uncertainty associated with $E_{0,j}$ is estimated from the range of threshold values determined from different data sets with variations in the parameter n, variations in vibrational frequencies (±10%), changes in τ by factors of 2, and the uncertainty of the absolute energy scale, 0.05 eV (lab). In deriving the final optimized reaction energies at 0 K for the loose TS reactions, we assume that the measured threshold $E_{0,j}$ values for dissociation are from ground state reactant to ground state ion and neutral reaction products. Given the relatively long experimental time frame (~5×10^{-4} s), dissociating products should be able to rearrange to their low energy conformations after collisional excitation.

Computational Details

Model structures, vibrational frequencies, and energetics for all reaction species, including all transition state and intermediate species, were calculated using Gaussian 09 [36]. Optimizations of all low-lying structures were performed at the B3LYP/6-311+G(d,p) level. A series of relaxed potential energy surface (PES) scans at this level were performed in order to identify the elementary steps of the decomposition of H^+AMOx and H^+DKP. Transition state and intermediate structures occurring along the PESs were then optimized at this level, where it was verified that each transition state contains one imaginary frequency and each intermediate is vibrationally stable. Each rate-limiting transition state was further examined with an intrinsic reaction coordinate (IRC) calculation to verify that it connects the appropriate intermediates. Rotational constants were obtained from the optimized structures, and all vibrational frequencies were also calculated at this level. When used in internal energy determinations or for RRKM calculations, the vibrational frequencies were scaled by 0.99 [37]. Zero-point vibrational energy (ZPE) corrections were additionally determined using the scaled vibrational frequencies. Single

UU IR Author Manuscript

point energies of all reactants, products, and key intermediates and transition states were determined at the B3LYP and MP2(full) levels using the 6-311+G(2d,2p) basis set. Recent work has shown that these levels of theory provide accurate comparisons with experimental energetics for such protonated systems, with mean absolute deviations of about 10 kJ/mol [31,35,38].

We also directly compared these results with those calculated by Siu and coworkers [1,39] at the B3LYP/6-31++G(d,p) level, where their previous work has also suggested satisfactory agreement with experiment, again within about 8 – 13 kJ/mol (although this conclusion appears to be based primarily on proton affinity comparisons). To reassess the accuracy of this approach with that chosen here, we compare this level of theory with our previous results for calculations on G, H^+G, CH_2NH, $CH_2NH_2^+$, H_2O, and CO [38] in Table S1. These allow the proton affinities (PA) of glycine and CH_2NH and the endothermicity for the reaction, $H^+G \rightarrow CH_2NH_2^+ + H_2O + CO$, to be compared with independently measured experimental values (none of which are from our laboratory). The three approaches reported in the present work, B3LYP/6-311+G(d,p), B3LYP/6-311+G(2d,2p)//B3LYP/6-311+G(d,p), and MP2(full)/6-311+G(2d,2p)//B3LYP/6-311+G(d,p), give values for these PAs and reaction energy with mean absolute deviations (MADs) between 1.2 and 3.4 kJ/mol, Table S1. In contrast, the B3LYP/6-31++G(d,p) approach yields a MAD of either 5.2 or 6.9 kJ/mol depending on whether an experimental [40] or very high level (W2) theoretical value for PA(CH_2NH) [41] is used for comparison. Calculations also performed at the B3LYP/6-31G(d,p), B3LYP/6-31+G(d,p), and B3LYP/6-311++G(d,p) and B3LYP/6-311++G(2d,2p) level show that the better agreement with the literature values is achieved by using the triple-zeta basis set and that diffuse functions on hydrogen do not alter the energies appreciably (~0.1 kJ/mol). In particular, we note that the 6-31G(d,p), 6-31+G(d,p), and 6-31++G(d,p) basis sets yield energies for the decomposition reaction of protonated glycine that lie 50, 11, and 12 kJ/mol, respectively, above the best experimental literature thermochemistry [38], whereas any of the triple-zeta results used here lie within 2.4 kJ/mol of the experimental value. Such differences are also found in the calculated thermochemistry for the present systems; B3LYP/6-31++G(d,p) results are an average

of 16 ± 10 kJ/mol higher than B3LYP/6-311+G(d,p) results.

Oxygen-protonated AMOx

Table S3 lists the energies of the various oxygen-protonated species, shown in Figure S2, along with transition states linking them. If the carbonyl oxygen (O_2) is protonated, we find four conformers of AMOx. The two lowest of these has the proton lying cis to the ring oxygen [O_{2c}], whereas in the other two, it is trans [O_{2t}]. The intramolecular OH•OC hydrogen bond stabilizes the former by about 10 kJ/mol. The amino methyl side-chain can be oriented in two positions, either c_t or g_t, where the subscript indicates that the amino group has its lone-pair in a trans orientation relative to the CC bond. The g_t conformers lie 2 – 3 kJ/mol higher in energy than the c_t conformers for both [O_{2c}] and [O_{2t}]. In all cases, protonation at this point weakens the C-O bond of the ring (essentially incipient formation of a terminal carboxylic acid group) such that this bond distance is 1.54 – 1.55 Å for the [O_{2t}] conformers and 1.59 – 1.61 Å for the [O_{2c}] conformers, compared to 1.307 Å in the H^+AMOx GS. Indeed, the cyclic form of the oxazolone ring is stabilized for [O_{2c}]-g_t by a NH•O hydrogen bond. In [O_{2c}]-c_t, this stabilization is lacking and we find that this structure is not stable using the 6-311+G(d,p) basis set, but can only be found using double-zeta basis sets, as used by previous authors [1,39,42]. The structure shown in Figure S2 was determined using a 6-31+G(d,p) basis set. For the triple-zeta basis set, [O_{2c}]-c_t ring opens to form an alklyated nitrile with a near linear CNCC central portion of the molecule. This *N*-carboxymethyl-2-aminoacetonitrile (CAAN) is a species previously located by Balta et al. [42] and called a retro-Ritter product by Reid et al. [43]. CAAN[O_{2c}]-t and CAAN[O_{2t}]-t have C-O bond distances of 3.240 and 3.117 Å and lie 72 – 76 and 105 – 110 kJ/mol, respectively, above the H^+AMOx GS.

If the ring oxygen (O_1) is protonated, the OC-O bond of the ring cleaves forming an acylium ion stabilized by interaction with the hydroxyl group. There are three of these [O_1] conformers having different side chain orientations, t, c_t, and c, lying 118 – 128, 160 – 171, and 162 – 174 kJ/mol, respectively, above the GS. The former is stabilized by the OH•NH_2

UU IR Author Manuscript

hydrogen bond, which is also evident in the longer OC-OH bond distance of 2.637 Å compared to 2.577 and 2.589 Å for the c_t and c conformers. Alternatively, ring-protonated AMOx can break the other O-C bond in the ring leading to the open nitrile structures, CAAN[O_{1c}]-g and t, lying 82 – 86 and 84 – 87 kJ/mol above the GS. The latter complex is related to the CAAN[O_{2c}]-t by rotation of the carboxylic acid group.

Of the transition states located, the key one is TS(H^+AMOx[N_1-O_1]-t), which transfers the proton from the terminal nitrogen to the ring oxygen and. This is the lowest energy pathway found that converts from N-protonated to O-protonated species, lying 117 – 127 kJ/mol above the H^+AMOx GS. Notably, although the H^+AMOx[O_1]-t species can be located (lying 3.9 – 5.4 kJ/mol below the TS before zero point energy (ZPE) corrections are made). Once these corrections are made, the TS lies below this species by 0.7 – 2.3 kJ/mol. Thus, the proton spontaneously reverts back to the nitrogen. In order to form a stable O-protonated form, the side chain must rotate back over TS(H^+AMOx[O_1]-(t-c)) at 166 – 177 kJ/mol above the GS, Table S3, such that this is the rate-limiting TS for production of stable oxygen-protonated conformers. This is sufficiently high in energy that such conformers are not important in the dissociation of H^+AMOx.

Theoretical Results for Direct $b_2^+ \rightarrow a_1^+$ Decomposition

Siu and coworkers elucidated a mechanism for directly forming the $CH_2NH_2^+$ (a_1^+) ion from b_2^+ [1,39]. Our exploration of this mechanism is shown in Figure S4 and differs from that reported earlier in the initial steps. Table S6 lists the energies of the various species involved. Despite repeated attempts to relocate the rate-limiting TS reported by Siu and coworkers (including use of both the 6-31++G(d,p) and 6-311+G(d,p) basis sets as well as starting points constructed to mimic that reported in the Supporting information of their paper), we could never find a TS (**1→6**) that directly connected H^+AMOx[N_2]-c (**1**) with the c-$C_3H_4NO_2^+$[N]$(CH_2NH)_{CHN}$ complex (**6**). Rather, H^+AMOx[N_2]-c first transforms to H^+AMOx[N_2]-g_t, which removes the stabilizing N_2H•N_1 hydrogen bond. Then the system passes over TS(H^+AMOx[N_2]-g_t(C~C)) in

which the carbon bond to the amino-methyl group is broken. This TS lies 160 – 164 (DFT) or 189 (MP2) kJ/mol above the H^+AMOx GS, compared to the 174 kJ/mol value that Siu and coworkers found for TS(**1**→**6**). Our TS is partially stabilized by a NH•O(ring) hydrogen bond (2.23 Å), which is not present in the structure reported by Siu and coworkers. This TS leads to a $(c\text{-}C_3H_3NO_2)(CH_2NH_2^+)_{OHN}$ complex that retains the NH•O(ring) hydrogen bond (1.83 Å). Lying only 1 – 3 kJ/mol higher in energy (and 7 – 12 kJ/mol below the rate-limiting TS) is $TS(cC_3H_3NO_2)(CH_2NH_2^+)_{(OC)HN}$, in which the NH•O(ring) bond is broken and replaced by N•HC, thereby forming a covalent CH bond and the relatively stable $(c\text{-}C_3H_4NO_2^+[N])(CH_2NH)_{CHN}$ complex (**6**). From here, the mechanism shown in Figure S4 matches that of Siu and coworkers [1]. The CH_2NH species transfers from the N•HC hydrogen bond to a more stable N•HN bond, where the proton is equally shared between the $c\text{-}C_3H_3NO_2$ and CH_2NH units as indicated by energy differences of 0 – 2 (**0**) kJ/mol. In agreement with Siu and coworkers, the TS between having the proton localized on either unit actually lies lower in energy once zero point corrections are made, by 3 – 5 (**5**) kJ/mol. Thus, dissociation of this complex can easily form both $CH_2NH_2^+$ + $c\text{-}C_3H_3NO_2$ and $c\text{-}C_3H_4NO_2^+[N]$ + CH_2NH, with the former products being favored by 20 – 23 (**25**) kJ/mol. The latter product (*m/z* 86) was not observed either here or by Siu and coworkers, but in our work, it could be masked by the much more intense primary product ion at *m/z* 87. In either case, the products are limited by the rate-limiting $TS(H^+AMOx[N_2]\text{-}g_t(C\sim C))$ at 160 – 189 kJ/mol. This is 32 – 63 (**36**) kJ/mol above the TS for decarbonylation of H^+AMOx, and in addition, the former TS is tighter than the latter with entropies of activation of 23 versus 42 J/K mol. Thus, direct cleavage of $b_2^+ \rightarrow a_1^+$ in reaction (3b) will not compete very effectively with formation of a_2^+ in reaction (1) at low energies.

Siu and coworkers also located another means of forming a_1^+ directly from b_2^+ that involves synchronously breaking three bonds, leading to direct formation of $CH_2NH_2^+$ + H_2CCO + HNCO. This $TS(H^+AMOx[N_2]\text{-}c\{OC\sim O,C\sim N,C\sim C\})$ (**1**→**5**) was very high in energy, 299.2 kJ/mol, and therefore was not explored further here.

For the b_2^+ ion derived from H^+GAG, the ring in H^+AMOx is methylated. In agreement

UU IR Author Manuscript

with Siu and coworkers, we find the TS for direct formation of $CH_2NH_2^+$ (a_1^+) from H^+MAMOx, TS(H^+MAMOx[N_2]-g_t{C~C}) (**1→8**), lies 6 (**7**) kJ/mol above the analogous TS in the H^+AMOx system, Table S6, which Siu and coworkers attribute to better charge stabilization of the associated b_2^+ ion. Because the mechanism shown in Figure S4 forms the $CH_2NH_2^+$ (a_1^+) ion involving the terminal nitrogen, an analogous mechanism for ring-methylated H^+MAMOx cannot form $C_2H_4NH_2^+$. As noted above, the very similar shapes and magnitudes of the $C_2H_4NH_2^+$ and $CH_2NH_2^+$ cross sections in Figure 1c with each other and with that for $CH_2NH_2^+$ in Figure 1a indicates that these species are dominantly formed by similar mechanisms. This is consistent with the decomposition of the proton-bound H^+(CH_2NH)(RCHNH) complex (where R = H or CH_3) but not with the direct $b_2^+ \rightarrow a_1^+$ mechanism. Therefore interpretation of the threshold for appearance of the a_1^+ ion via this mechanism, whether in competition with a_2^+ formation or not, as suggested by Siu and coworkers, is inconsistent with our results. Harrison and coworkers reached the same conclusion for the methylated b_2^+ ion [44].

To further verify this result, we analyzed the data for b_2^+(H^+GGG) as a competition between a_2^+ and a_1^+ formation. Both channels could be reproduced with high fidelity (with only small changes in the parameters for a_2^+ formation), however, the cross section for a_1^+ formation had to be scaled upwards by a factor between $8 - 150 \times 10^3$, a nonphysical result that could indicate the calculated TS is too tight. However, as noted above, the $\Delta S^{\ddagger}_{1000}$ value is 23 J/K mol, which is not that much tighter than for the a_2^+ channel, 42 J/K mol. Such a scaling factor can sometimes be removed by scaling the frequencies instead. In order to reproduce the data in this fashion, the vibrational frequencies (arbitrarily chosen as < 625 cm^{-1}) for the TS needed to be scaled by $0.3_5 \pm 0.1$, which leads to a $\Delta S^{\ddagger}_{1000}$ value of 102 J/K mol, much larger than most phase-space-limit TSs (a product-like TS that is the loosest reasonable TS). In these models, the thresholds for a_1^+ formation are similar, 2.29 ± 0.12 and 2.21 ± 0.20 eV, Table S5, well above the values obtained by Siu and coworkers, 1.69 +0.08/-0.12 eV with competition and 1.85 +0.09/-0.13 eV when competition was ignored. We also note that our thresholds are inconsistent with the theoretically calculated energies of TS(H^+MAMOx[N_2]-g_t{C~C}), 160 – 189 kJ/mol. For

UU IR Author Manuscript

completeness, we also tried using the parameters of Siu and coworkers (with no scaling of the cross section or frequencies) to reproduce our data, but this gives a cross section for the a_1^+ ion that has the wrong shape and is an order of magnitude too small above 4 eV even though the threshold is much too low compared to our data. Overall, we conclude that although this pathway may contribute to the total a_1^+ cross sections at high energies, it cannot be the primary pathway for its formation.

Theoretical Results for Alternate Decomposition Pathways of H^+DKP: Reactions (12) and (14)

The lowest energy pathway found for reactions (12) and (14) is shown in Figure S5. It starts with the c-$C_3H_7N_2O^+[N_1]$ product ion formed after decarbonylation of H^+DKP, Figure 4. Cleavage of the CN bond assisted by backside attack of the oxygen forms an epoxide, c-$CH_2C(O)NHCH_2NH_2^+[N_1]$-c, with a transition state lying 226 – 236 kJ/mol above H^+DKP. Rotating the terminal amino-methyl group to a trans position costs little energy, 9 – 11 kJ/mol, and forms c-$CH_2C(O)NHCH_2NH_2^+[N_1]$-t. From here, a proton can transfer from the central CH_2 group to the terminal CH_2 group over the rate-limiting transition state at 287 – 328 kJ/mol, which is 14 – 27 kJ/mol lower than that for the pathway to reactions (11) and (13). This process forms the ketone $CH_3C(=O)NHCHNH_2^+[N_1]$-tc, which is the most stable of the $C_3H_7N_2O^+$ isomers examined here, lying 60 – 81 kJ/mol below the cyclic form (and along with the CO product, 11 – 16 kJ/mol below H^+DKP). (As noted in the text, the $CH_3C(=O)NHCHNH_2^+$ isomer was not considered by Siu and coworkers [45] or Bythell et al. [46] in their IRMPD studies of the a_2^+ ion, even though it is lower in energy and can be derived directly from the cyclic species c-$C_3H_7N_2O^+[N]$ with an energy barrier lower than those leading to some isomers that were considered.) From this species, cleavage of the CN bond passes over TS($CH_3C(=O)NHCHNH_2^+[N_1]$-tc{C~N}) to form the products of reaction (14) and proton transfer yields those of reaction (12). As these products lie 226 – 239 and 83 – 125 kJ/mol, respectively, below the rate-limiting TS, formation of these species should be facile once the H atom transfer TS is surmounted. Ultimately, although the rate-limiting TS for this pathway is

UU IR Author Manuscript

lower in energy than that for reactions (11) and (13), it appears to be inactive because the $H_2NCHNH_2^+$ (*m/z* 45) product ion is not observed and the large difference in the relative energies of reactions (12) and (14) disfavors appreciable formation of the CH_3CO^+ product ion. This observation can probably be understood by realizing that the $C_3H_7N_2O^+$ product (whether in the linear or cyclic conformation) can dissociate by decarbonylation much more easily than by reactions (12) and (14). The former process is restricted by TS($C_3H_7N_2O^+[N_2]$-ct{C~OC~N}) at 201 – 216 kJ/mol above H^+ DKP, whereas the latter lies 85 – 112 kJ/mol higher in energy.

References

[1] H. El Aribi, C.F. Rodriquez, D.R.P. Almeida, Y. Ling, W.W.-N. Mak, A.C. Hopkinson, K.W.M. Siu, J. Am. Chem. Soc. 125 (2003) 9229.
[2] D. Gerlich, Adv. Chem. Phys. 82 (Part 1) (1992) 1.
[3] K.M. Ervin, P.B. Armentrout, J. Chem. Phys. 83 (1985) 166.
[4] N. Aristov, P.B. Armentrout, J. Phys. Chem. 90 (1986) 5135.
[5] D.A. Hales, P.B. Armentrout, J. Cluster Science 1 (1990) 127.
[6] A. Mookherjee, M.J. Van Stipdonk, P.B. Armentrout, work in progress.
[7] R.M. Moision, P.B. Armentrout, J. Am. Soc. Mass Spectrom. 18 (2007) 1124.
[8] R.M. Moision, P.B. Armentrout, J. Phys. Chem. A 106 (2002) 10350.
[9] A.L. Heaton, R.M. Moision, P.B. Armentrout, J. Phys Chem. A 112 (2008) 3319.
[10] A.L. Heaton, P.B. Armentrout, J. Phys. Chem. B 112 (2008) 12056.
[11] T. Kim, A.V. Tolmachev, R. Harkewicz, D.C. Prior, G. Anderson, H.R. Udseth, R.D. Smith, Anal. Chem. 72 (2000) 2247.
[12] D.R. Carl, R.M. Moision, P.B. Armentrout, J. Am. Soc. Mass Spectrom. 20 (2009) 2312.
[13] S.J. Ye, R.M. Moision, P.B. Armentrout, Int. J. Mass Spectrom. 240 (2005) 233.
[14] A.L. Heaton, P.B. Armentrout, J. Am. Chem. Soc. 130 (2008) 10227.
[15] A.L. Heaton, S.J. Ye, P.B. Armentrout, J. Phys. Chem. A 112 (2008) 3328.
[16] S.J. Ye, P.B. Armentrout, J. Phys. Chem. A 112 (2008) 3587.
[17] E. Teloy, D. Gerlich, Chem. Phys. 4 (1974) 417.
[18] D. Gerlich, Adv. Chem. Phys. 82 (1992) 1.
[19] N.F. Dalleska, K. Honma, L.S. Sunderlin, P.B. Armentrout, J. Am. Chem. Soc. 116 (1994) 3519.
[20] N.R. Daly, Rev. Sci. Instrum. 31 (1960) 264.
[21] K.M. Ervin, P.B. Armentrout, J. Chem. Phys. 83 (1985) 166.
[22] F. Muntean, P.B. Armentrout, J. Chem. Phys. 115 (2001) 1213.
[23] T.S. Beyer, D.F. Swinehart, Commun. ACM 16 (1973) 379.
[24] S.E. Stein, B.S. Rabinovitch, J. Chem. Phys. 58 (1973) 2438.
[25] S.E. Stein, B.S. Rabinovitch, Chem. Phys. Lett. 49 (1977) 183.
[26] R.G. Gilbert, S.C. Smith, Theory of Unimolecular and Recombination Reactions, Blackwell Scientific, London, 1990.
[27] P.J. Robinson, K.A. Holbrook, Unimolecular Reactions, Wiley Interscience, New York, 1972.
[28] M.T. Rodgers, K.M. Ervin, P.B. Armentrout, J. Chem. Phys. 106 (1997) 4499.
[29] M.T. Rodgers, P.B. Armentrout, J. Chem. Phys. 109 (1998) 1787.
[30] P.B. Armentrout, J. Chem. Phys. 126 (2007) 234302.
[31] P.B. Armentrout, A.L. Heaton, J. Am. Soc. Mass Spectrom. (2011) in press.

[32] D.A. Hales, L. Lian, P.B. Armentrout, Int. J. Mass Spectrom. Ion Processes 102 (1990) 269.
[33] F. Muntean, P.B. Armentrout, J. Phys. Chem. B. 106 (2002) 8117.
[34] F. Muntean, P.B. Armentrout, J. Phys. Chem. A 107 (2003) 7413.
[35] A.L. Heaton, P.B. Armentrout, J. Am. Soc. Mass Spectrom. 20 (2009) 852.
[36] M.J. Frisch, G.W. Trucks, H.B. Schlegel, G.E. Scuseria, M.A. Robb, J.R. Cheeseman, J.A. Montgomery, Jr., T. Vreven, K.N. Kudin, J.C. Burant, J.M. Millam, S.S. Iyengar, J. Tomasi, V. Barone, B. Mennucci, M. Cossi, G. Scalmani, N. Rega, G.A. Petersson, H. Nakatsuji, M. Hada, M. Ehara, K. Toyota, R. Fukuda, J. Hasegawa, M. Ishida, T. Nakajima, Y. Honda, O. Kitao, H. Nakai, M. Klene, X. Li, J.E. Knox, H.P. Hratchian, J.B. Cross, C. Adamo, J. Jaramillo, R. Gomperts, R.E. Stratmann, O. Yazyev, A.J. Austin, R. Cammi, C. Pomelli, J.W. Ochterski, P.Y. Ayala, K. Morokuma, G.A. Voth, P. Salvador, J.J. Dannenberg, V.G. Zakrzewski, S. Dapprich, A.D. Daniels, M.C. Strain, O. Farkas, D.K. Malick, A.D. Rabuck, K. Raghavachari, J.B. Foresman, J.V. Ortiz, Q. Cui, A.G. Baboul, S. Clifford, J. Cioslowski, B.B. Stefanov, G. Liu, A. Liashenko, P. Piskorz, I. Komaromi, R.L. Martin, D.J. Fox, T. Keith, M.A. Al-Laham, C.Y. Peng, A. Nanayakkara, M. Challacombe, P.M.W. Gill, B. Johnson, W. Chen, M.W. Wong, C. Gonzalez, J.A. Pople, Gaussian 03, revision B.02, Gaussian, Inc., Pittsburgh, PA, 2003.
[37] J.A. Montgomery, Jr., M.J. Frisch, J.W. Ochterski, G.A. Petersson, J. Chem. Phys. 110 (1999) 2822.
[38] P.B. Armentrout, A.L. Heaton, S.J. Ye, J. Phys. Chem. A. (2011) in press.
[39] H. El Aribi, G. Orlova, C.F. Rodriquez, D.R.P. Almeida, A.C. Hopkinson, K.W.M. Siu, J. Phys. Chem. B 108 (2004) 18743.
[40] G. Bouchoux, J.-Y. Salpin, Rapid Commun. Mass Spectrom. 13 (1999) 932.
[41] G.D. Oliveira, J.M.L. Martin, I.K.C. Silwal, J.F. Liebman, J. Computational Chem. 22 (2001) 1297.
[42] B. Balta, M. Basma, V. Aviyente, C. Zhub, C. Lifshitz, Int. J. Mass Spectrom. 201 (2000) 69.
[43] G.E. Reid, R.J. Simpson, R.A.J. O'Hair, J. Am. Soc. Mass Spectrom. 9 (1998) 945.
[44] A.G. Harrison, I.G. Csizmadia, T.-H. Tang, J. Am. Soc. Mass Spectrom. 11 (2000) 427.
[45] U.H. Verkerk, C.-K. Siu, J.D. Steill, H. El Aribi, J. Zhao, C.F. Rodriguez, J. Oomens, A.C. Hopkinson, K.W.M. Siu, J. Phys. Chem. Lett. 1 (2010) 868.
[46] B.J. Bythell, P. Maitre, B. Paizs, J. Am. Chem. Soc. 132 (2010) 14766.
[47] E. Uggerud, Theor. Chem. Acc. 97 (1997) 313.
[48] E.P.L. Hunter, S.G. Lias, J. Phys. Chem. Ref. Data 27 (1998) 413.
[49] S. Hammerum, T.I. Sølling, J. Am. Chem. Soc. 121 (1999) 6002.
[50] B. Paizs, M. Schnolzer, U. Warnken, S. Suhaib, A.G. Harrison, Phys. Chem. Chem. Phys. 6 (2004) 2691.
[51] R.A.L. Peerboom, S. Ingemann, N.M.M. Nibbering, J.F. Liebman, J. Chem. Soc. Perkin 2 (1990) 1825.
[52] R.A.J. O'Hair, P.S. Broughton, M.L. Styles, B.T. Frink, C.M. Hadad, J. Am. Soc. Mass Spectrom. 11 (2000) 687.
[53] B. Balta, V. Aviyente, C. Lifshitz, J. Am. Soc. Mass Spectrom. 14 (2003) 1192.

TABLE S1: Comparison of 0 K theoretical and experimental values for proton affinities (PA) of glycine (G) and CH_2NH and H^+G fragmentation.

	This work										Literature	
Process	B3LYP /TZ+[a]	MP2 /TZ+[b]	B3LYP// B3LYP[c]	B3LYP/ TZ++[d]	B3P86// B3LYP[e]	MP2// B3LYP[f]	MP2// MP2[g]	B3LYP /DZ[h]	B3LYP /DZ+[h]	B3LYP /DZ++[h]	theory	experiment
PA(G)	878.8	881.3	881.4	881.0	888.8	879.6	878.9	908.1	881.3	881.4	925 (MP2)[i] 895 (G2)[i]	880.5 ± 8[j]
PA(CH_2NH)	863.3	860.9	862.9	862.6	868.0	858.7	858.4	881.7	865.5	865.2	862.2 ± 3.0[k]	846.9 ± 8[i] 848 ± 8[l] 856.9 ± 6.3[m]
$H^+G \rightarrow$ $CH_2NH_2^+$ + H_2O + CO	137.1	130.7	137.1	136.9	184.1	136.6	134.7	189.0	150.4	150.6	199.2 (B3LYP)[n] 118.4 (QCISD)[n] 172.8 (MP2)[n] 154 (MP2)[i]	139.0 ± 8.2[o]
MAD[p]	**1.6**	3.5	**1.2**	1.1	19.7	**2.3**	3.3	32.4	5.2	5.2		
MAD[q]	**3.4**	4.4	**3.0**	2.8	21.4	**1.8**	2.5	34.1	6.9	6.9		

[a] B3LYP/6-311+G(d,p). [b] MP2(full)/6-311+G(d,p). [c] B3LYP/6-311+G(2d,2p)//B3LYP/6-311+G(d,p). [d] B3LYP/6-311++G(2d,2p). [e] B3P86/6-311+G(2d,2p)//B3LYP/6-311+G(d,p). [f] MP2(full)/6-311+G(2d,2p)//B3LYP/6-311+G(d,p). [g] MP2(full)/6-311+G(2d,2p)// MP2(full)/6-311+G(d,p). [h] B3LYP/6-31G(d,p), B3LYP/6-31+G(d,p), and B3LYP/6-31++G(d,p). [i] Uggerud [47]: MP2/6-31G(d,p) and G2(MP2). [j] Hunter and Lias [48]. [k] W2 theory [41]. See also Hammerum and Sølling [49] and Paizs et al. [50]. [l] Peerboom et al. [51]. [m] Bouchoux and Salpin [40]. [n] O'Hair et al. [52]. 298 K values adjusted to 0 K. B3LYP/6-31G(d), QCISD(T)/6-31+G(d,p)//B3LYP/6-31G(d), MP2/6-31G(d). [o] Evaluated from literature heats of formation, see [38]. [p] Mean absolute deviation from experimental values and W2 value for PA(CH_2NH). [q] Mean absolute deviation from experimental values. PA(CH_2NH) from [40]. Bold indicates levels of theory used in the present study.

Table S2. Relative theoretical energies (kJ/mol) at 0 K of H^+AMOx and H^+DKP conformers and transition states (and their imaginary frequencies in cm^{-1}) connecting them.[a]

Species	B3LYP[b]	B3LYP// B3LYP[b]	MP2(full) //B3LYP[b]	Lit	imag freq
H^+AMOx[N_2]-c	0.0	0.0	0.0	0.0[c,d]	
H^+AMOx[N_1]-c	24.0	24.2	13.0	23.8[c]	
H^+AMOx[N_2]-g	29.4	28.5	30.7		
H^+AMOx[N_2]-g_t	33.6	31.6	35.9		
H^+AMOx[N_1]-t	43.0	44.7	33.4		
TS(H^+AMOx[N_2]-(cg))	29.9	29.1	31.2		69
TS(H^+AMOx[N_2]-g_{c-t})	45.6	43.1	47.6		306
TS(H^+AMOx[N_2-N_1]-c)	37.2	38.6	29.5		1269
TS(H^+AMOx[N_2]-(cg_t))	39.6	38.1	42.9		100
TS(H^+AMOx[N_1]-(ct))	50.9	51.2	40.7		79
H^+DKP[O_c]	-11.7 (0.0)	-11.9 (0.0)	-7.3 (0.0)	-12.6[d]	
H^+DKP[O_t]	-4.7 (7.0)	-4.4 (7.5)	0.0 (7.4)		
H^+DKP[N]	51.1 (62.8)	55.8 (67.8)	45.3 (52.7)	54.0[d]	
TS(H^+DKP[O_{c-t}])	19.8 (31.6)	19.2 (31.1)	25.8 (33.1)		555
TS(H^+DKP[O_t-N])	216.5 (228.2)	219.5 (231.3)	216.5 (223.8)		1833
TS(H^+DKP[O_c-N])	240.7 (252.4)	243.1 (255.0)	230.2 (237.5)		1735

[a] Values are relative to H^+AMOx[N_2]-c. Values in parentheses show the energies relative to H^+DKP[O_c]. [b] Values from the present study at the B3LYP/6-311+G(d,p), B3LYP/6-311+G(2d,2p)//B3LYP/6-311+G(d,p), and MP2(full)/6-311+G(2d,2p)//B3LYP/6-311+G(d,p) levels of theory. [c] B3LYP/6-31++G(d,p) results from Siu and coworkers [1]. [d] B3LYP/6-31+G(d,p) results from Balta et al. [53].

UU IR Author Manuscript

Table S3. Relative theoretical energies (kJ/mol) at 0 K of oxygen-protonated H^+AMOx conformers and transition states (and their imaginary frequencies in cm^{-1}) connecting them.[a]

Species	B3LYP[b]	B3LYP// B3LYP[b]	MP2(full) //B3LYP[b]	Lit[c]	imag freq
H^+AMOx[N_2]-c	0.0	0.0	0.0	0.0	
CAAN[O_{2c}]-t	74.8	75.5	72.2	72.0	
CAAN[O_{1c}]-g	83.9	86.0	82.0		
CAAN[O_{1c}]-t	85.8	87.2	84.2		
CAAN[O_{2t}]-t	109.9	107.0	105.3		
H^+AMOx[O_{2c}]-c_t [d]	116.6	111.4	119.2	113.4	
H^+AMOx[O_{2c}]-g_t	118.5	113.6	121.1		
H^+AMOx[O_1]-t	125.8	128.0	118.0		
H^+AMOx[O_{2t}]-c_t	130.0	122.2	129.6		
H^+AMOx[O_{2t}]-g_t	132.5	125.2	132.3		
H^+AMOx[O_1]-c_t	171.3	171.2	160.7		
H^+AMOx[O_1]-c	173.6	173.1	162.3		
TS(H^+AMOx[$O_{2c\text{-}1c}$]-t) (rotation -)	94.9	95.7	93.5		50
TS(H^+AMOx[$O_{2c\text{-}1c}$]-t) (rotation +)	95.1	95.9	93.6		50
CAAN[O_{1c}]-(g-t)	106.3	106.7	103.0		343
CAAN[O_{2t}]-(t-c-t)	113.2	110.2	108.7		8
TS(H^+AMOx[O_{2c}]-g_t-CAAN[O_{2c}]-t)	117.3	113.2	121.4		173
TS(H^+AMOx[N_1-O_1]-t)	123.5	126.8	117.3		396
TS(H^+AMOx[O_{2t}]-t-CAAN[O_{2c}]-t)	126.8	125.4	124.0		559
TS(H^+AMOx[O_{2c}]-(g^+_t-g^-_t)	128.2	123.2	130.4		89
TS(H^+AMOx[O_{2t}]-c_t-CAAN[O_{2t}]-t)	132.2	126.0	136.6		157
TS(H^+AMOx[O_{2t}]-(c-g_t)	139.2	131.8	139.8		75

TS(CAAN[O_{2t}-O_{1t}-O_{2t}]-t)	141.0	137.9	139.7	51
TS(H^+AMOx[O_{2t}]-(g^+_t-g^-_t)	141.3	134.0	141.1	89
TS(H^+AMOx[O_{2t-c}]-c)	169.1	162.6	173.9	715
TS(H^+AMOx[O_1]-(t-c))	176.9	177.2	166.2	77
TS(H^+AMOx[O_1]-(c-c_t))	179.3	178.6	168.2	242
TS(CAAN[O_{1c}]-t-H^+AMOx[O_{1c}]-c_t)	198.5	200.0	201.5	366
TS(CAAN[O_{1c}]-g-H^+AMOx[O_{1c}]-c)	202.4	203.9	205.4	362
TS(H^+AMOx[O_{2c}]-t -CAAN[O_{1c}]-t)	242.6	241.2	236.2	1990

[a] Values are relative to H^+AMOx[N_2]-c. [b] Values from the present study at the B3LYP/6-311+G(d,p), B3LYP/6-311+G(2d,2p)//B3LYP/6-311+G(d,p), and MP2(full)/6-311+G(2d,2p)//B3LYP/6-311+G(d,p) levels of theory. [c] B3LYP/6-31+G(d,p) values from Balta et al. [53]. [d] Geometry optimized at B3LYP/6-31+G(d,p) level. Collapses to CAAN[O_{2c}]-t at the present level of theory.

Table S4. Relative theoretical energies (kJ/mol) at 0 K of H^+AMOx and H^+DKP fragmentation intermediates, products, and transition states (and their imaginary frequencies in cm^{-1})

Species	B3LYP[a]	B3LYP// B3LYP[a]	MP2(full) //B3LYP[a]	Literature[b]	imag freq
H^+AMOx[N_2]-c	0.0	0.0	0.0	0.0 (**1**)	
TS(H^+AMOx[N_2]-c{OC~O})	127.8	131.7	126.4	137.7 (**1**→**2**)	338
TS(H^+AMOx[N_1]-c{OC~O})	151.4	154.4	147.1		386
TS(H^+DKP[N]{C~CO~N})	149.5	154.3	150.6		276
	(*161.2*)	(*166.1*)	(*157.9*)		
c-$C_3H_7N_2O^+$[N_1]($CO_{N1H•Cu}$)	27.5	31.9	9.5		
c-$C_3H_7N_2O^+$[N_1]($CO_{N1H•Cd}$)	27.7	32.3	10.5		
c-$C_3H_7N_2O^+$[N_1]($CO_{N2H•C}$)	37.4	41.9	21.5		
$C_3H_7N_2O^+$[N_1]-ct(OC_{HN1})	72.8	77.1	67.6		
$C_3H_7N_2O^+$[N_2]-ct(OC_{HN2})	80.0	84.7	75.7		
$C_3H_7N_2O^+$[N_2]-ct(OC_{HC})	80.8	85.9	81.5		
$C_3H_7N_2O^+$[N_2]-ct(OC_C)	81.0	86.1	80.4	92.5 (**2**)	
$C_3H_7N_2O^+$[N_2]-ct(OC_{HN1})	82.3	87.3	82.4		
$C_3H_7N_2O^+$[N_1]-ct(OC_C)	88.1	92.8	85.4		
$C_3H_7N_2O^+$[N_2]-cc(OC_{HN2})	112.9	117.0	104.6		
$C_3H_7N_2O^+$[N_2]-cc(OC_C)	123.4	127.9	116.6		
$C_3H_7N_2O^+$[N_2]-cc(OC_{HN1})	123.6	128.1	118.1		
TS($C_3H_7N_2O^+$[N_2]-ct(CO_{HN1-HC}))	81.0	86.1	80.7		20
TS($C_3H_7N_2O^+$[N_2]-ct(CO_{C-HC}))	82.2	87.3	83.2		29
TS($C_3H_7N_2O^+$[N_2]-ct($CO_{HN2-HN1}$))	84.8	89.8	82.5		24
TS($C_3H_7N_2O^+$[N_1]-ct(CO_{HN1-C}))	89.5	94.1	85.2		18

TS($C_3H_7N_2O^+[N_1\text{-}N_2]$-ct($CO_{HN1}$))	90.6	96.7	90.7		1139
TS(c-$C_3H_7N_2O^+[N_1]${C~N_1}(CO_{HN2}))	109.3	114.1	113.3		183
TS(c-$C_3H_7N_2O^+[N_1]${C~N_1}(CO_{HN1}))	118.5	123.1	123.6		176
TS($C_3H_7N_2O^+[N_2]$-cc($CO_{HN2\text{-}HN1}$))	125.3	129.7	116.8		33
TS($C_3H_7N_2O^+[N_2]$-cc($CO_{C\text{-}HN2}$))	123.4	127.8	118.4		25
c-$C_3H_7N_2O^+[N_1]$ + CO	50.8	55.4	41.9	59.4 (**4**)	
$C_3H_7N_2O^+[N_2]$-ct + CO	91.0	96.1	96.8	102.5 (**3**)	
$C_3H_7N_2O^+[N_1]$-ct + CO	92.8	97.4	95.4		
$C_3H_7N_2O^+[N_2]$-cc + CO	120.6	125.0	125.5	132.2 (**12**)	
$H^+(CH_2NH)_2(OC_{HN})$ + CO	92.6	96.6	94.4		
$H^+(CH_2NH)_2(OC_C)$ + CO	100.6	104.9	103.8	120.5 (**14**)	
TS($C_3H_7N_2O^+[N_2\text{-}N_1]$-ct) + CO	104.1	110.4	110.7		1157
TS(c-$C_3H_7N_2O^+[N_1]${C~N_1}) + CO	128.3	133.1	140.3	139.7 (**4**→**12**)	182
TS($C_3H_7N_2O^+[N_2]$-c(tc)) + CO	136.6	139.5	138.1	150.2 (**3**→**4**)	114
TS($C_3H_7N_2O^+[N_2]$-ct{C~OC~N}) + CO	189.2	192.4	208.5	208.8 (**3**→**14**)	190
$H^+(CH_2NH)_2$ + 2 CO	106.8	111.3	115.8	126.4 (**15**)	
$H^+(CH_2NH)CO$ + CO + CH_2NH	191.9	192.9	195.9		
	(*203.7*)	(*204.7*)	(*203.3*)		
$CH_2NH_2^+$ + OCNH + CH_2CO	146.0	150.6	193.2	174.9 (**5**)	
$CH_2NH_2^+$ + CH_2NH + 2 CO	216.7	218.2	227.4	238.1	
	(*228.4*)	(*230.1*)	(*234.7*)		

[a] Values from the present study at the B3LYP/6-311+G(d,p), B3LYP/6-311+G(2d,2p)// B3LYP/6-311+G(d,p), and MP2(full)/6-311+G(2d,2p)//B3LYP/6-311+G(d,p) levels of theory. Values in italics are relative to $H^+DKP[O_c]$.

[b] B3LYP/6-31++G(d,p) values from Siu and coworkers [1]. Designations in parentheses are the names used by these authors.

TABLE S5: Fitting Parameters of Eq. (S1), Threshold Energies (eV) at 0 K, and Entropies of Activation (J/K mol) at 1000 K[a]

Reaction	Reactant	Products[b]	TS[c]	σ_0	n	E_0	$\Delta S^{\ddagger}_{1000}$
4	H^+DKP	$C_3H_7N_2O^+ + CO$	H^+DKP[O_t-N]	3.8 (0.8)	1.4 (0.2)	2.17 (0.18)	-15 (2)
6		$CH_3CO^+ + OCNH + CH_2NH$	$H^+CH_2CONHCH_2[O_c]\{C\sim N\}$			~2.77 (0.20)	24 (2)
1	b_2^+ (H^+GGG)	$a_2^+ + CO$	H^+AMOx{OC~O}	6.5 (2.4)	1.2 (0.2)	1.56 (0.12)	42 (2)
7	b_2^+ (H^+GAG)	$a_2^+ + CO$	H^+MAMOx{OC~O}	16.7 (4.6)	1.1 (0.2)	1.44 (0.10)	34 (2)
4	H^+DKP	$a_2^+ + CO$	H^+DKP[O_t-N]	5.4 (3.4)	1.4 (0.4)	2.11 (0.20)	-15 (2)
2		$\rightarrow H^+(CH_2NH)_2 + 2\ CO$	$C_3H_7N_2O^+\{C\sim OC\sim N\}$	5.7 (3.6)		2.97 (0.28)	40 (2)
5	H^+DKP	$CH_2NH_2^+(CO) + CH_2NH + CO$	$C_3H_7N_2O^+\{C\sim OC\sim N\}$	1.7 (01.0)	1.7 (0.2)	2.64 (0.16)	40 (2)
2		$H^+(CH_2NH)_2 + 2\ CO$	$C_3H_7N_2O^+\{C\sim OC\sim N\}$	3.7 (1.6)		2.58 (0.16)	40 (2)
3a		$\rightarrow CH_2NH_2^+ + CH_2NH + 2\ CO$	PSL	4.3 (2.4)		3.37 (0.12)	43 (10)
1	b_2^+ (H^+GGG)	$a_2^+ + CO$	H^+AMOx{OC~O}	5.8 (1.4)	1.2 (0.4)	1.55 (0.14)	42 (2)
2		$\rightarrow H^+(CH_2NH)_2 + 2\ CO$	$C_3H_7N_2O^+\{C\sim OC\sim N\}$	5.6 (2.0)		2.86 (0.28)	40 (2)
2	b_2^+ (H^+GGG)[d]	$H^+(CH_2NH)_2 + 2\ CO$	$C_3H_7N_2O^+\{C\sim OC\sim N\}$	4.0 (1.8)	1.5 (0.6)	2.50 (0.30)	40 (2)
3a		$\rightarrow a_1^+ + CH_2NH + 2\ CO$	PSL	3.7 (1.6)		2.92 (0.42)	43 (10)
1	b_2^+ (H^+GGG)[e]	$a_2^+ + CO$	H^+AMOx{OC~O}	6.9 (2.8)	1.1 (0.2)	1.58 (0.10)	42 (2)
3b		$a_1^+ + cC_3H_3NO_2$	H^+AMOx[N_2]-g_t{C~C}	2.7 (3.9) $\times 10^5$		2.29 (0.24)	23 (2)
				6.9 (2.8)[g]		2.21 (0.40)	102 (20)
7	b_2^+ (H^+GAG)	$a_2^+ + CO$	H^+MAMOx{OC~O}	16.7 (4.6)	1.1 (0.2)	1.44 (0.12)	34 (2)

8		→ $H^+(CH_2NH)(C_2H_4NH)$ + 2 CO	$C_4H_9N_2O^+${C~OC~N}	17.8 (6.0)		3.04 (0.18)	54 (2)
8	b_2^+ (H^+GAG)[f]	$H^+(CH_2NH)(C_2H_4NH)$ + 2 CO	$C_4H_9N_2O^+${C~OC~N}	4.5 (2.2)	1.4 (0.2)	2.62 (0.08)	54 (2)
9a		→ $C_2H_4NH_2^+$ + CH_2NH + 2 CO	PSL	13.2 (4.6)		2.62 (0.08)	34 (10)
9a	b_2^+ (H^+GAG)[e,h]	$C_2H_4NH_2^+$ + CH_2NH + 2 CO	PSL	8.2 (5.0)	1.8 (0.4)	2.73 (0.30)	32 (10)
10a		a_1^+ + C_2H_4NH + 2 CO	PSL			2.91 (0.30)	35 (10)

[a] Uncertainties (2 standard deviations) in parentheses. [b] Arrow indicates a sequential process coming after the previous entry. [c] H^+AMOx{OC~O} = TS(H^+AMOx[N_2]-c{OC~O}). H^+MAMOx{OC~O} = TS(H^+MAMOx[N_2]-ctg{OC~O}). $C_3H_7N_2O^+${C~OC~N} = $C_3H_7N_2O^+$[N_2]-ct{C~OC~N}. $C_4H_9N_2O^+${C~OC~N} = $C_4H_9N_2O^+$[N_2]-ctt{C~OC~N}. H^+AMOx{C~C} = H^+AMOx[N_2]-g_t{C~C}. PSL = loose phase space limit. [d] EM = $C_3H_7N_2O^+$[N_2]-ct. [e] Competition between the indicated TSs is included in the modeling. [f] EM = $C_4H_9N_2O^+$[N_2]-ctt. [g] Frequencies of TS below 625 cm^{-1} scaled by 0.3 – 0.4. [h] EM = $(C_2H_4NH)H^+(CH_2NH)$.

Table S6. Relative theoretical energies (kJ/mol) at 0 K of intermediates, products, and transition states (and their imaginary frequencies in cm^{-1}) involved in direct formation of $CH_2NH_2^+$ (a_1^+) from H^+AMOx (b_2^+) and H^+MAMOx (b_2^+)

Species	B3LYP[a]	B3LYP// B3LYP[a]	MP2(full) //B3LYP[a]	Literature[b]	imag freq
H^+AMOx[N_2]-c / *H^+MAMOx[N_2]-c*	0.0	0.0	0.0	0.0 (**1**)	
(c-$C_3H_3NO_2$)($CH_2NH_2^+$)$_{NHN}$	48.6	50.5	62.3	49.4 (**8**)	
(c-$C_3H_4NO_2^+$)(CH_2NH)$_{NHN}$	48.6	50.1	64.0	49.4 (**7**)	
(c-$C_3H_4NO_2^+$)(CH_2NH)$_{CHN}$	84.5	85.4	104.6	86.6 (**6**)	
(c-$C_3H_3NO_2$)($CH_2NH_2^+$)$_{OHN}$	149.7	155.1	176.0		
TS(c-$C_3H_3NO_2$)H^+(CH_2NH)$_{NHN}$	43.5	45.8	58.7	44.4 (**7→8**)	764
TS(c-$C_3H_4NO_2^+$)(CH_2NH)$_{(CN)HN}$	87.7	88.5	106.0	90.0 (**6→7**)	65
TS(c-$C_3H_3NO_2$)($CH_2NH_2^+$)$_{(OC)HN}$	153.0	156.3	177.0		131
TS(H^+AMOx[N_2]-g_t{C~C})	160.0	164.0	189.3	173.6 (**1→6**)[c]	219
TS(H^+MAMOx[N_2]-g_t{C~C})	*166.4*	*170.3*	*195.6*	*180.7* (**1→8**)[c]	*218*
$CH_2NH_2^+$ + c-$C_3H_3NO_2$	130.2	130.2	149.8	131.0 (**9**)	
$CH_2NH_2^+$ + c-$C_4H_5NO_2$	*142.7*	*143.1*	*161.7*	*143.1 (**11**)*	
c-$C_3H_4NO_2^+$ (H^+Ox) + CH_2NH	151.8	149.9	172.5	155.6 (**10**)	
c-$C_4H_6NO_2^+$ (H^+MOx) + CH_2NH	*148.3*	*146.3*	*170.1*		
c-$C_3H_3NO_2$ (carbene) + $CH_2NH_2^+$	245.8	247.1	280.3	244.3 (**11**)	

[a] Values from the present study at the B3LYP/6-311+G(d,p), B3LYP/6-311+G(2d,2p)// B3LYP/6-311+G(d,p), and MP2(full)/6-311+G(2d,2p)//B3LYP/6-311+G(d,p) levels of theory. Values in italics refer to methylated species.

[b] B3LYP/6-31++G(d,p) values from Siu and coworkers [1,39]. Designations in parentheses are the names used by these authors.

[c] This TS is not the same as that found in the present work. See text.

Table S7. Relative theoretical energies (kJ/mol) at 0 K of intermediates, products, and transition states (and their imaginary frequencies in cm^{-1}) involved in formation of CH_3CO^+ from H^+DKP

Species	B3LYP[a]	B3LYP// B3LYP[a]	MP2(full) //B3LYP[a]	imag freq
$H^+DKP[O_c]$	0.0	0.0	0.0	
$TS(H^+DKP[O_c]\{C\sim C,C\sim N\})$	273.8	278.3	272.5	581
$H^+CH_2CONHCH_2[O_c] + OCNH$	123.4	123.7	148.6	
$TS(H^+CH_2CONHCH_2[O_c]\{C\sim N\}) + OCNH$	301.6	305.4	354.8	376
$CH_2NH_2^+ + CH_2CO + OCNH$	157.8	162.5	200.6	
$CH_3CO^+ + CH_2NH + OCNH$	219.7	221.7	235.4	
$c\text{-}C_3H_7N_2O^+[N_1] + CO$	62.5	67.3	49.2	
$TS(c\text{-}C_3H_7N_2O^+[N_1]\{C\sim N\})+ CO$	226.6	229.2	235.8	372
$c\text{-}CH_2C(O)NHCH_2NH_2^+[N_1]\text{-}c + CO$	207.7	211.1	212.4	
$c\text{-}CH_2C(O)NHCH_2NH_2^+[N_1]\text{-}(ct) + CO$	216.7	219.8	223.2	80
$c\text{-}CH_2C(O)NHCH_2NH_2^+[N_1]\text{-}t + CO$	211.6	214.3	218.4	
$TS(c\text{-}CH_2C(O)NHCH_2NH_2^+[N_1]\text{-}t\{C\sim H\sim C\}) + CO$	287.0	289.2	327.9	438
$CH_3C(=O)NHCHNH_2^+[N_1]\text{-}tc + CO$	-16.3	-13.8	-11.3	
$TS(CH_3C(=O)NHCHNH_2^+[N_1]\text{-}tc\{C\sim N\}) + CO$	110.8	116.8	111.1	207
$H_2NCHNH_2^+ + CH_2CO + CO$	58.2	63.1	89.1	
$CH_3CO^+ + H_2NCHNH + CO$	204.0	206.0	202.5	

[a] Values from the present study at the B3LYP/6-311+G(d,p), B3LYP/6-311+G(2d,2p)// B3LYP/6-311+G(d,p), and MP2(full)/6-311+G(2d,2p)//B3LYP/6-311+G(d,p) levels of theory.

Figure Captions

Figure S1. Structures for H^+AMOx and H^+DKP with relative energies in kJ/mol from Table 1. Hydrogen bonds are shown by dashed lines.

Figure S2. Structures for oxygen protonated H^+AMOx with relative energies in kJ/mol from Table 1. Weak bonds are shown by dashed lines.

Figure S3. Potential energy surface for coupling between $[N_2]$ and $[N_1]$ forms of H^+AMOx and their decarbonylation pathways. Geometry optimizations and single point energies of each elementary step are determined at the B3LYP/6-311+G(d,p) level of theory and corrected for ZPE. Short dashed lines indicate hydrogen bonds and longer dashed lines show bonds that are breaking.

Figure S4. Reaction coordinate surface for direct formation of a_1^+ from H^+AMOx. Geometry optimizations and single point energies of each elementary step are determined at the B3LYP/6-311+G(d,p) level of theory and corrected for ZPE. Short dashed lines indicate hydrogen bonds and longer dashed lines show bonds that are breaking or particularly weak interactions.

Figure S5. Reaction coordinate surface for formation of CH_3CO^+ in reaction (12) and for reaction (14). Geometry optimizations and single point energies of each elementary step are determined at the B3LYP/6-311+G(d,p) level of theory and corrected for ZPE. Short dashed lines show bonds that are breaking or weak interactions.

UU IR Author Manuscript

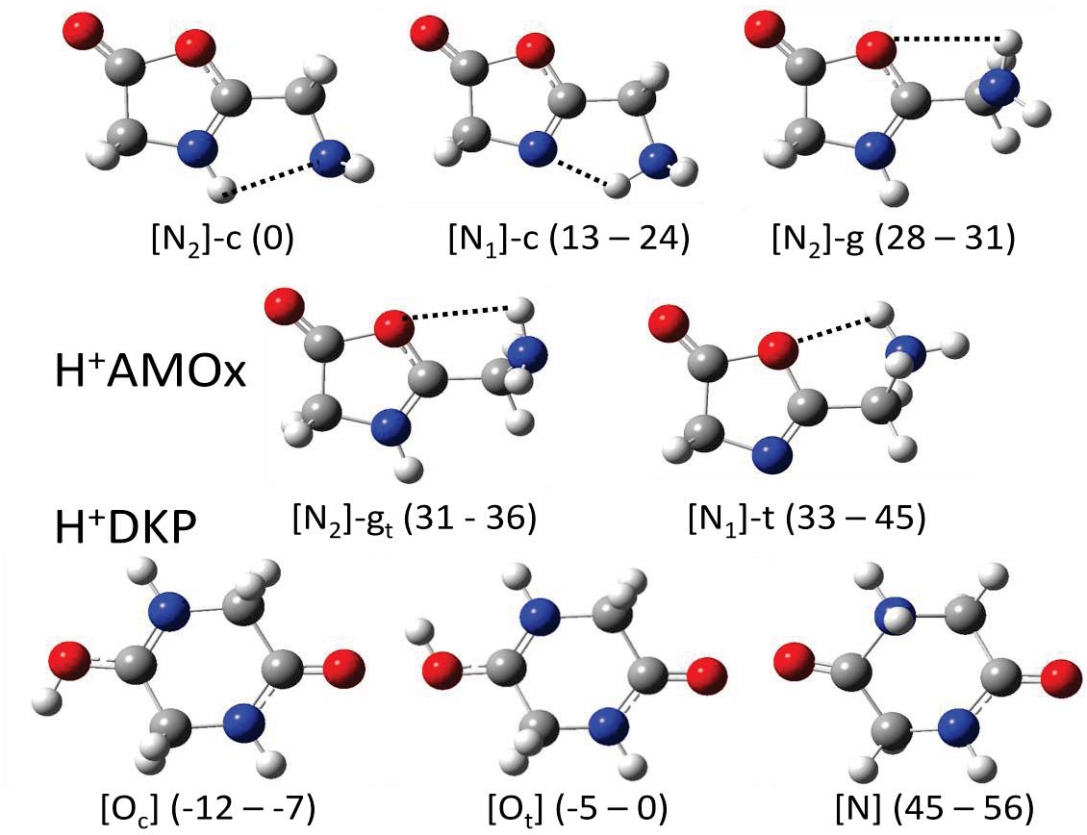

Figure S1

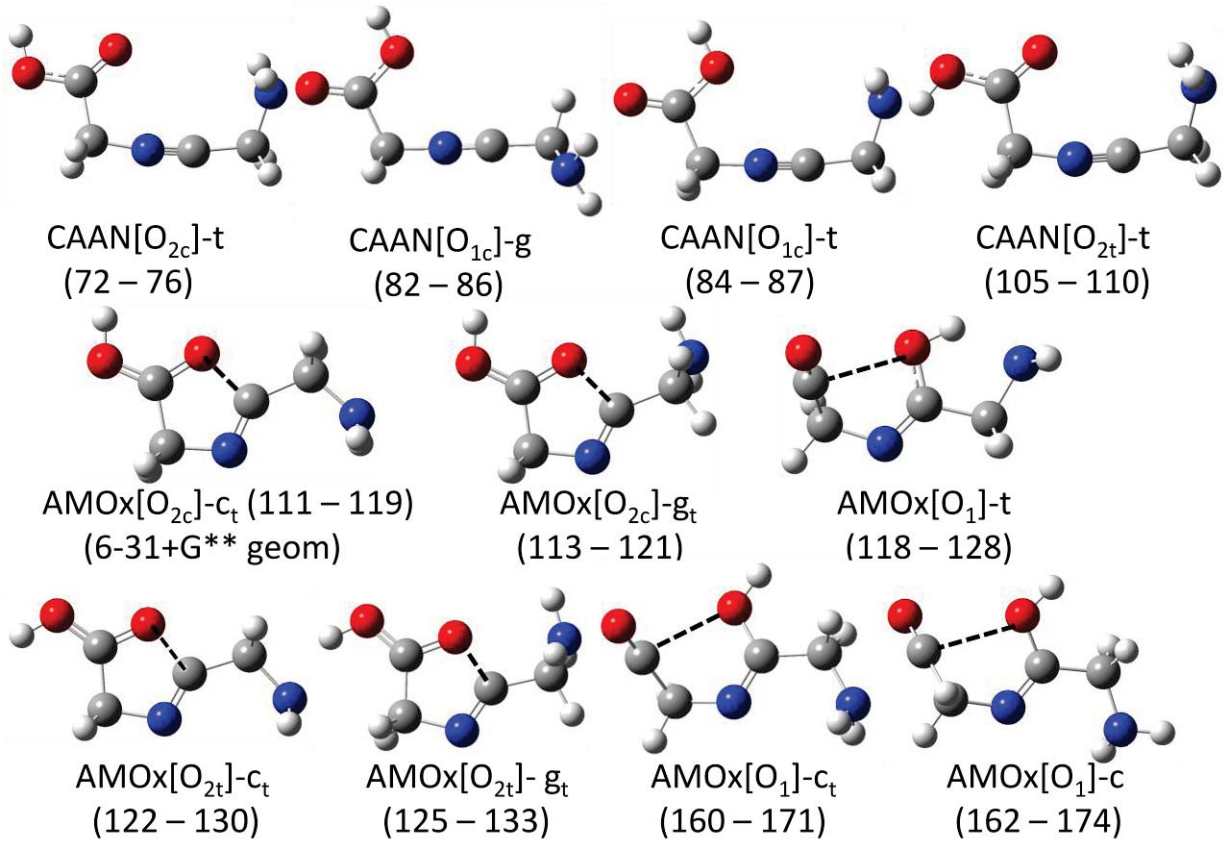

Figure S2

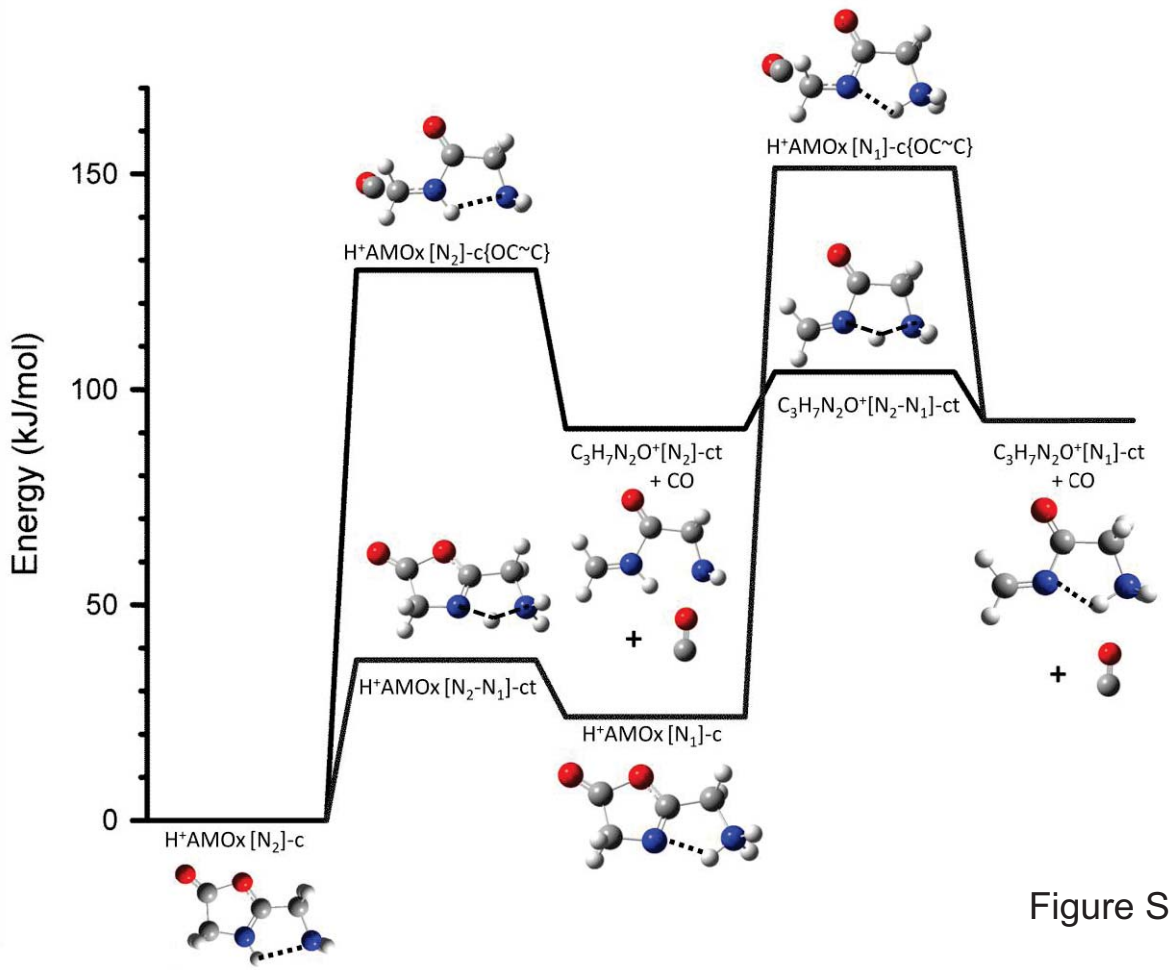

Figure S3

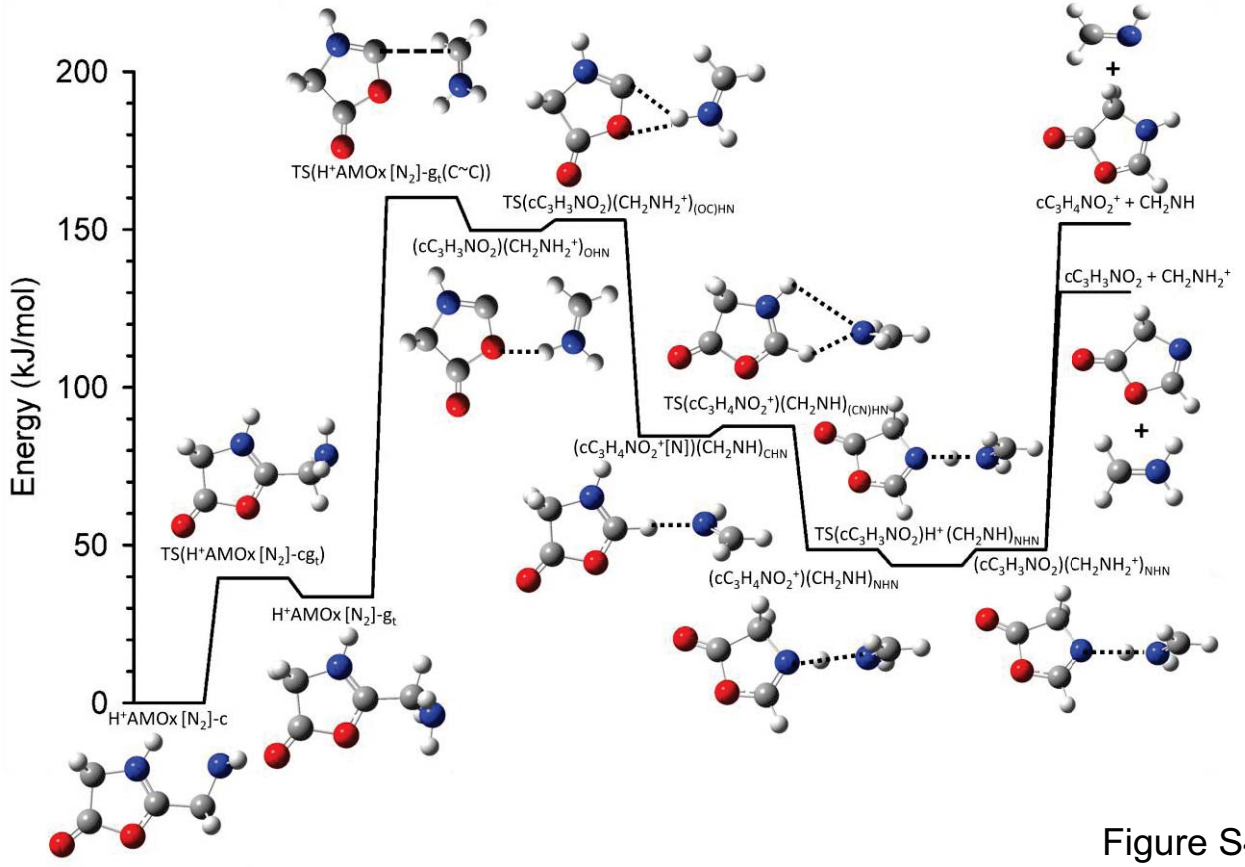

Figure S4

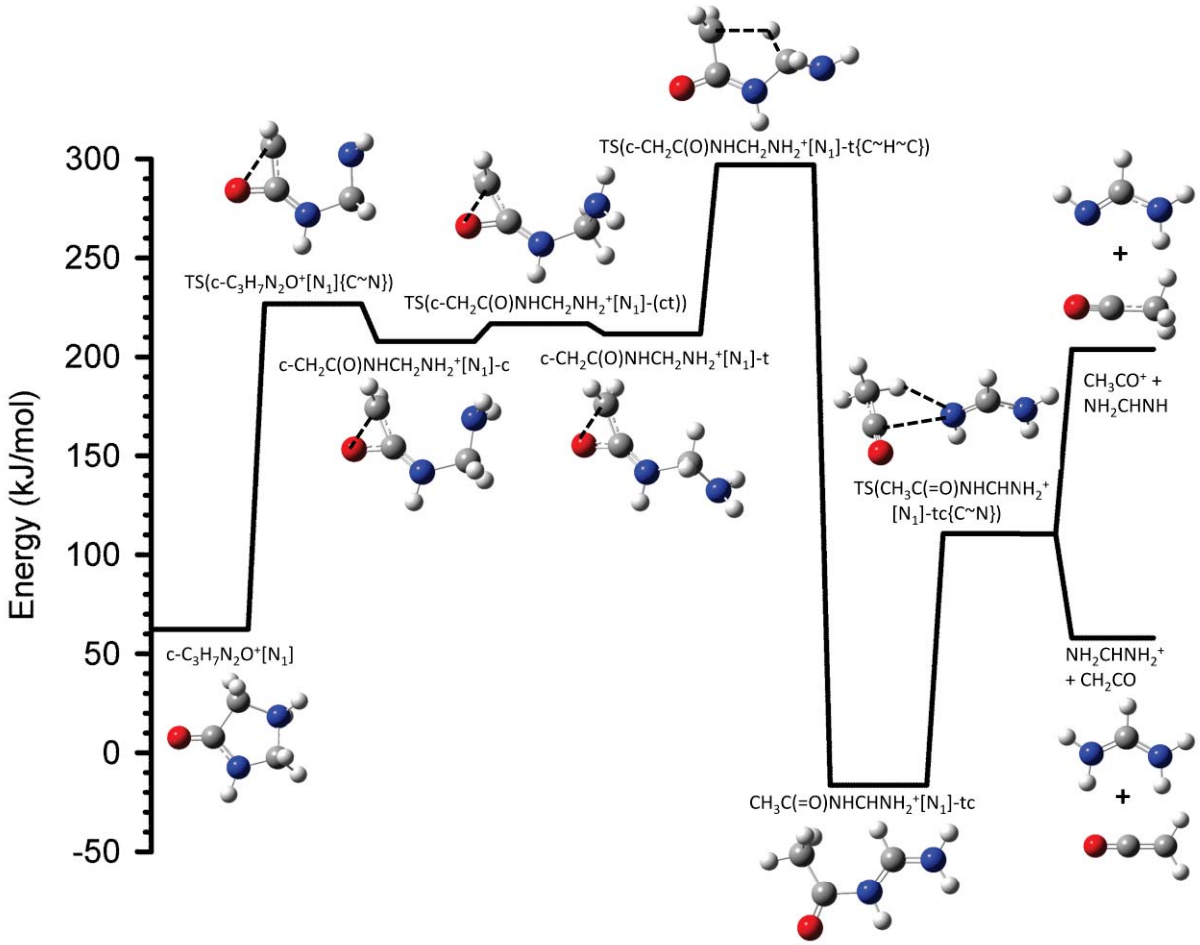

Figure S5

UU IR Author Manuscript

Supplementary Information

for

The Simplest b_2^+ Ion: Determining Its Structure from Its Energetics by a Direct Comparison of the Threshold Collision-induced Dissociation of Protonated Oxazolone and Diketopiperazine

by P. B. Armentrout and Amy A. Clark

Analysis of previous experiments

Siu and coworkers [1] suggest they operate under single collision conditions by stating that at their highest collision gas pressures "an ion that has a collision cross-section of 100 Å^2 will have, on average, undergone one collision in q2 with argon", where q2 designates their rf only quadrupole collision region. Calculations indicate that this statement means that 50% of the ions undergo one collision and 50% undergo no collisions. What this definition fails to recognize is that subsequent collisions can also occur. Presuming that the cross section remains at 100 Å^2 for subsequent reaction collisions, 25% of all ions undergo only one collision, 12% undergo two collisions, 6% undergo three collisions, and 6% undergo more collisions. Generally, in our laboratory, "single collision conditions" refer to a pressure where <10% of the ions undergo one collision, such that only 1% undergo more than one collision. This makes corrections for multiple collisions straightforward to achieve. In order to reach true "single collision conditions" for a cross section of 100 Å^2, Siu and coworkers would need to operate what they call their CGT (collision-gas thickness, or $n\ell$, where n is the number density of the collision gas and ℓ is the length of the collision cell) at 10^{13} atoms/cm^2, which is one order of magnitude smaller than their largest CGT and a factor of 2.5 smaller than the smallest CGT utilized. In truth, the cross sections for these ions are unlikely to be this large such that larger CGT values can be used and still correspond to single collision conditions. In the present system, our TCID data are collected at CGT values of approximately 50, 25, and 12 × 10^{12} atoms/cm^2, or half the values used by Siu and coworkers, where contributions from three or more collisions are negligible.

By operating in this higher pressure regime, their ions are undergoing extensive

UU IR Author Manuscript

scattering because of multiple collisions. Also contributing to the loss of ions (reactants and products) will be the lower trapping efficiency of the quadratic radial trapping field in a quadrupole (compared to the octopole trapping field which varies as the sixth power of the radius) [2,3]. Such effects may mean that a simple exponential fit of the pressure data (which they use to extrapolate their data to zero pressure) is not accurate. These considerations explain two observations made in the paper of Siu and coworkers. 1) The authors state they did not use Xe as a collision gas because the data are too scattered. As we have shown several times [4,5], collisions with Xe deposit energy more efficiently than those with Ar, such that the CID cross sections rise more rapidly, leading to more easily interpreted thresholds. This is because Xe is more massive and polarizable such that the collision is longer-lived and intrinsically more likely. At the higher pressures used by Siu and coworkers, this enhanced collision probability, coupled with the quadratic radial trapping field of a quadrupole, apparently leads to excessive loss of their ions, leading to smaller signals and more scattered data. Use of the lighter Ar allows the scattering to occur in a more forward laboratory direction such that more ions are observed, even though the efficiency of the energy transfer and thus the fragmentation is reduced. 2) The cross section reported for dissociation of H^+GGG with Ar is anomalously large, nearly 200 $Å^2$ at 4 eV. Such a cross section corresponds to the Langevin-Gioumousis-Stevenson (LGS) collision cross section with Ar at the very low energy of 0.01 eV. At 4 eV, the LGS cross section with Ar is 10 $Å^2$, but at these energies, the size of the ion is important such that a hard sphere (HS) cross section is a better estimate. A generous estimate of the hard sphere cross section for H^+GGG + Ar (averaged over various orientations of the ion) using the theoretically calculated ground state structure is 100 $Å^2$ (and even for the static orientation giving the maximum profile, it's only 140 $Å^2$). However, this can only correspond to the observed cross section if *every* collision leads to dissociation. For a process that is endothermic, grazing collisions (which are included in this hard sphere estimate) cannot possibly cause dissociation, such that these estimates are upper limits. A simple line-of-centers estimate for a process that is endothermic by 1.37 eV (as reported by Siu and coworkers for this process) indicates that only 66% (= 1 - E_0/E) of the HS

collisions can supply enough energy to induce dissociation at 4 eV. Even this estimate is too large because of kinetic shifts, which would reduce the effective cross section to 30% of the HS cross section (estimated using the threshold energy reported by Siu and coworkers). Indeed, measurements in our laboratory of the cross section for dissociation of H^+GGG + Xe (which should have a slightly larger hard-sphere cross section than Ar) obtain a maximum cross section for the b_2^+ fragment ion of ~10 $Å^2$ at ~3 eV (along with appreciable amounts of the y_2^+ fragment and minor amounts of six other products, none of which are reported by Siu and coworkers).[6] We believe that the b_2^+ cross section observed by Siu and coworkers is too large (by over an order of magnitude) because reactant ions are being lost because of scattering, inflating the apparent cross section for dissociation. However, this also means that product ions are likely to be lost to scattering as well (in part because they move more slowly than the reactant ions and therefore spend more time in the collision cell). Coupled with inaccurate extrapolation to zero pressure conditions (noted above) and the inefficient quadratic radial trapping field of a quadrupole, these factors affect the shape of the cross section measured, which may obscure the correct threshold dependence. Unfortunately, such possibilities cannot be checked easily as no fitting parameters for the cross sections are reported in this paper except for the threshold energies. Hence the shape and magnitudes of the cross sections measured cannot be reproduced except for the single case shown ($H^+GGG + Ar \rightarrow b_2^+$).

It can also be noted that the kinetic energy distribution of the ions in this study are substantially broader (FWHM = 2 eV in the laboratory frame) than those obtained here (0.1 – 0.2 eV). This is partly a consequence of the quadratic radial trapping field, which distorts the energy distribution of the ions, but may also reflect source conditions. Such broadening will spread out the onset for fragmentations. Coupled with the more inefficient dissociation probability, these effects lead to a very slow onset for the dissociation threshold. Indeed comparison of the reported cross section for $H^+GGG + Ar \rightarrow b_2^+$ compared to our own data using Xe shows their apparent dissociation onset is shifted to higher energies by about 1.0 eV.

The difficulty with modeling slowly rising cross sections is that the *n* parameter of Eq.

UU IR Author Manuscript

(S1), see below, is necessarily large, with the optimum value used depending critically on the range of data chosen for reproduction. In such cases, a large range of n values can be used to reproduce the data with a commensurate large range of threshold energies (larger n leading to smaller E_0 values). In our modeling procedure, the uncertainty in the value of n reported includes the range of values capable of reproducing the data and propagates to resultant variations in the threshold energies. Although the discussion of systematic uncertainties applied by the Siu group is extensive, this discussion does not include such variations, and the range of n values applied is not provided for any system.

General Experimental Procedures

The electrospray ionization (ESI) source [7-10] is operated using a 50:50 by volume H_2O/MeOH solution with ~10^{-4} M GGG, GAG, or DKP and ~10^{-4} M acetic acid (all chemicals purchased from Sigma-Aldrich), syringe-pumped at a rate of 0.04 mL/hr into a 35 gauge stainless steel needle biased at ~2000 V. Ionization occurs over the ~5 mm distance from the tip of the needle to the entrance of the capillary, biased at ~35 V. Ions are directed by a capillary heated to 80 °C into a radio frequency (rf) ion funnel [11], wherein they are focused into a tight beam. Ions exit the ion funnel and enter an rf hexapole ion guide that traps them radially. To generate b_2^+ ions, H^+GGG or H^+GAG is dissociated using an in-source fragmentation technique that uses electrodes placed between the hexapole rods [12]. These b_2^+ and H^+DKP ions undergo multiple collisions (>10^4) with the ambient gas in the hexapole and become thermalized. In either case, ions emitted from the source are assumed to have internal energies described by a Maxwell-Boltzmann distribution of rovibrational states at 300 K, as characterized in previous experiments [7,9,10,12-16].

Ions are extracted from the source and mass selected using a magnetic momentum analyzer. The mass-selected ions are decelerated to a well-defined kinetic energy and focused into a rf octopole ion guide that traps the ions radially [17,18]. The ion guide minimizes losses of the reactant and any product ions resulting from scattering. The octopole passes through a

static gas cell containing xenon, which is used as the collision gas for reasons described elsewhere [4,19]. After collision, the reactant and product ions drift to the end of the octopole where they are extracted and focused into a quadrupole mass filter for mass analysis. The ions are detected with a high voltage dynode, scintillation ion detector [20] and the signal is processed using standard pulse counting techniques.

Ion intensities, measured as a function of collision energy, are converted to absolute cross sections as described previously [21]. Product branching ratios are calculated from the absolute cross sections. The uncertainty in these relative cross sections is about ±5% and that for the absolute cross sections is about ±20%. The ion kinetic energy distribution is measured to be Gaussian and has a typical fwhm of 0.1 – 0.2 eV (lab). Uncertainties in the absolute energy scale are about ±0.05 eV (lab). Ion kinetic energies in the laboratory (lab) frame are converted to energies in the center-of-mass (CM) frame using $E_{CM} = E_{lab}\, m/(m+M)$, where M and m are the masses of the ionic and neutral reactants, respectively.

Thermochemical Analysis

Threshold regions of the CID reaction cross sections are modeled using Eq. (S1),

$$\sigma_j(E) = (n\sigma_{0,j}/E)\sum g_i \int_{E_{0,j}-E_i}^{E} [k_j(E^*)/k_{tot}(E^*)]\{1-e^{-k_{tot}(E^*)\tau}\}(E-\varepsilon)^{n-1} d(\varepsilon) \qquad \text{(S1)}$$

where $\sigma_{0,j}$ is an energy-independent scaling factor for channel j, n is an adjustable parameter that describes the efficiency of collisional energy transfer [22], E is the relative kinetic energy of the reactants, $E_{0,j}$ is the threshold for dissociation of the ground electronic and rovibrational state of the reactant ion at 0 K for channel j, τ is the experimental time for dissociation (~5×10^{-4} s in the extended dual octopole configuration as measured by time-of-flight studies [22]), ε is the energy transferred from translation during the collision, and E^* is the internal energy of the energized molecule (EM) after the collision, i.e., $E^* = \varepsilon + E_i$. The summation is over the rovibrational states of the reactant ions, i, where E_i is the excitation energy of each state and g_i is the fractional population of those states ($\sum g_i = 1$). The Beyer-Swinehart algorithm [23-25] is used to evaluate

the number and density of the rovibrational states and the relative populations g_i are calculated for a Maxwell-Boltzmann distribution at 300 K. The term $k_j(E^*)$ is the unimolecular rate coefficient for dissociation of the EM to product channel j. The rate coefficients $k_j(E^*)$ and $k_{tot}(E^*)$ are defined by Rice–Ramsperger–Kassel–Marcus (RRKM) theory as in Eq. (S2) [26,27],

$$k_{tot}(E^*) = \sum_j k_j(E^*) = \sum_j d_j N_j^{\dagger}(E^* - E_{0,j}) / h\rho(E^*) \quad \text{(S2)}$$

where d_j is the reaction degeneracy of channel j, $N^{\dagger}_j(E^* - E_{0,j})$ is the sum of rovibrational states of the transition state (TS) for channel j at an energy $E^* - E_{0,j}$, and $\rho(E^*)$ is the density of states of the EM at the available energy, E^*. These rate coefficients allow both kinetic shifts and competition between multiple parallel channels to be modeled [28,29].

The decompositions studied here involve sequential dissociation pathways, for which accurate modeling requires additional assumptions, as described previously [30]. The difficulty in analyzing sequential thresholds lies in the fact that the initial dissociation process takes away an unknown distribution of energies in translational modes of the initial products, as well as internal modes of the neutral product. This leaves an unknown distribution of internal energies in the ionic product that undergoes further dissociation. The procedure used to handle this effect uses Eq. (S1) to reproduce the cross section for the product of the primary reaction, which excludes subsequent dissociation, $\sigma_{CID}(E)$, combined with the probability for further dissociation, $P_{D2} = 1 - \exp[-k_{2tot}(E_2^*)\tau_2]$. Here k_{2tot}, E_2^*, and τ_2 are the total rate coefficient for the secondary dissociation, the energy available to the secondary EM, and the time available for the secondary dissociation, respectively. This partitions the total CID cross section into that for the non-dissociating products, σ_1, and that for the sequential dissociation product ion, σ_2, as described in Eq. (S3).

$$\sigma_1(E) = \sigma_{CID}(E)(1 - P_{D2}) \quad \text{(S3a)}$$

$$\sigma_2(E) = \sigma_{CID}(E)P_{D2} \quad \text{(S3b)}$$

Here, the rate coefficients are again calculated using RRKM theory, Eq. (S2), for the new EM. The energy available to this EM is defined statistically, accomplished by methods described in

detail elsewhere [30], and recently extended to multiple sequential channels [31]. The combination of sequential and competitive modeling generally allows accurate reproduction of all experimental reaction cross sections.

Several effects that obscure the interpretation of the data must be accounted for during data analysis in order to produce accurate thermodynamic information. The first effect involves energy broadening resulting from the thermal motion of the neutral collision gas and the kinetic energy distribution of the reactant ion. This is accounted for by explicitly convoluting the model over both kinetic energy distributions, as described elsewhere in detail [21]. The second effect considers that Eq. (S1) only models cross sections that represent products formed as the result of a single collision event. To ensure rigorous single collision conditions, data are collected at three pressures of Xe, generally about 0.20, 0.10, and 0.05 mTorr, and the resulting cross sections evaluated for pressure effects and extrapolated to zero pressure when necessary [32]. The third effect arises from the lifetime for dissociation, which leads to a delayed onset for the CID threshold, a kinetic shift, which becomes more noticeable as the size of the molecule increases. These kinetic shifts are estimated by the incorporation of RRKM theory as shown in Eq. (S1) and as described in detail elsewhere [28]. To evaluate the rate coefficient in Eq. (S1), sets of rovibrational frequencies for the EM and all TSs are required and are taken from quantum chemical calculations detailed in the next section. The transitional frequencies for loose TSs are treated as rotors, a treatment that corresponds to a phase space limit (PSL), as described in detail elsewhere [28,29]. The 2D external rotations in these cases are treated adiabatically but with centrifugal effects included [25], and the adiabatic 2D rotational energy is treated using a statistical distribution with an explicit summation over all the possible values of the rotational quantum number [28,29]. For reactions where a tight TS is required, all molecular parameters are taken from theoretical results. Although originally developed primarily for systems with loose TSs, we have demonstrated that this modeling procedure is capable of accurately reproducing threshold information for tight TSs [33], as well as competition between loose and tight TSs [14,34,35]. We additionally determine the entropy of activation for each dissociation

channel as described in detail elsewhere [29]. These $\Delta S^{\ddagger}$ quantities, which are energy (or temperature) dependent, are tabulated at 1000 K.

The model cross sections of Eq. (S1) and (S3) are convoluted with the kinetic energy distribution of the reactants [21] and compared to the data. A nonlinear least-squares analysis is used to provide optimized values for $\sigma_{0,j}$, n, and $E_{0,j}$. The uncertainty associated with $E_{0,j}$ is estimated from the range of threshold values determined from different data sets with variations in the parameter n, variations in vibrational frequencies (±10%), changes in τ by factors of 2, and the uncertainty of the absolute energy scale, 0.05 eV (lab). In deriving the final optimized reaction energies at 0 K for the loose TS reactions, we assume that the measured threshold $E_{0,j}$ values for dissociation are from ground state reactant to ground state ion and neutral reaction products. Given the relatively long experimental time frame (~5×10^{-4} s), dissociating products should be able to rearrange to their low energy conformations after collisional excitation.

Computational Details

Model structures, vibrational frequencies, and energetics for all reaction species, including all transition state and intermediate species, were calculated using Gaussian 09 [36]. Optimizations of all low-lying structures were performed at the B3LYP/6-311+G(d,p) level. A series of relaxed potential energy surface (PES) scans at this level were performed in order to identify the elementary steps of the decomposition of H^+AMOx and H^+DKP. Transition state and intermediate structures occurring along the PESs were then optimized at this level, where it was verified that each transition state contains one imaginary frequency and each intermediate is vibrationally stable. Each rate-limiting transition state was further examined with an intrinsic reaction coordinate (IRC) calculation to verify that it connects the appropriate intermediates. Rotational constants were obtained from the optimized structures, and all vibrational frequencies were also calculated at this level. When used in internal energy determinations or for RRKM calculations, the vibrational frequencies were scaled by 0.99 [37]. Zero-point vibrational energy (ZPE) corrections were additionally determined using the scaled vibrational frequencies. Single

UU IR Author Manuscript

point energies of all reactants, products, and key intermediates and transition states were determined at the B3LYP and MP2(full) levels using the 6-311+G(2d,2p) basis set. Recent work has shown that these levels of theory provide accurate comparisons with experimental energetics for such protonated systems, with mean absolute deviations of about 10 kJ/mol [31,35,38].

We also directly compared these results with those calculated by Siu and coworkers [1,39] at the B3LYP/6-31++G(d,p) level, where their previous work has also suggested satisfactory agreement with experiment, again within about 8 – 13 kJ/mol (although this conclusion appears to be based primarily on proton affinity comparisons). To reassess the accuracy of this approach with that chosen here, we compare this level of theory with our previous results for calculations on G, H^+G, CH_2NH, $CH_2NH_2^+$, H_2O, and CO [38] in Table S1. These allow the proton affinities (PA) of glycine and CH_2NH and the endothermicity for the reaction, $H^+G \rightarrow CH_2NH_2^+ + H_2O + CO$, to be compared with independently measured experimental values (none of which are from our laboratory). The three approaches reported in the present work, B3LYP/6-311+G(d,p), B3LYP/6-311+G(2d,2p)//B3LYP/6-311+G(d,p), and MP2(full)/6-311+G(2d,2p)//B3LYP/6-311+G(d,p), give values for these PAs and reaction energy with mean absolute deviations (MADs) between 1.2 and 3.4 kJ/mol, Table S1. In contrast, the B3LYP/6-31++G(d,p) approach yields a MAD of either 5.2 or 6.9 kJ/mol depending on whether an experimental [40] or very high level (W2) theoretical value for PA(CH_2NH) [41] is used for comparison. Calculations also performed at the B3LYP/6-31G(d,p), B3LYP/6-31+G(d,p), and B3LYP/6-311++G(d,p) and B3LYP/6-311++G(2d,2p) level show that the better agreement with the literature values is achieved by using the triple-zeta basis set and that diffuse functions on hydrogen do not alter the energies appreciably (~0.1 kJ/mol). In particular, we note that the 6-31G(d,p), 6-31+G(d,p), and 6-31++G(d,p) basis sets yield energies for the decomposition reaction of protonated glycine that lie 50, 11, and 12 kJ/mol, respectively, above the best experimental literature thermochemistry [38], whereas any of the triple-zeta results used here lie within 2.4 kJ/mol of the experimental value. Such differences are also found in the calculated thermochemistry for the present systems; B3LYP/6-31++G(d,p) results are an average

of 16 ± 10 kJ/mol higher than B3LYP/6-311+G(d,p) results.

Oxygen-protonated AMOx

Table S3 lists the energies of the various oxygen-protonated species, shown in Figure S2, along with transition states linking them. If the carbonyl oxygen (O_2) is protonated, we find four conformers of AMOx. The two lowest of these has the proton lying cis to the ring oxygen [O_{2c}], whereas in the other two, it is trans [O_{2t}]. The intramolecular OH•OC hydrogen bond stabilizes the former by about 10 kJ/mol. The amino methyl side-chain can be oriented in two positions, either c_t or g_t, where the subscript indicates that the amino group has its lone-pair in a trans orientation relative to the CC bond. The g_t conformers lie 2 – 3 kJ/mol higher in energy than the c_t conformers for both [O_{2c}] and [O_{2t}]. In all cases, protonation at this point weakens the C-O bond of the ring (essentially incipient formation of a terminal carboxylic acid group) such that this bond distance is 1.54 – 1.55 Å for the [O_{2t}] conformers and 1.59 – 1.61 Å for the [O_{2c}] conformers, compared to 1.307 Å in the H^+AMOx GS. Indeed, the cyclic form of the oxazolone ring is stabilized for [O_{2c}]-g_t by a NH•O hydrogen bond. In [O_{2c}]-c_t, this stabilization is lacking and we find that this structure is not stable using the 6-311+G(d,p) basis set, but can only be found using double-zeta basis sets, as used by previous authors [1,39,42]. The structure shown in Figure S2 was determined using a 6-31+G(d,p) basis set. For the triple-zeta basis set, [O_{2c}]-c_t ring opens to form an alklyated nitrile with a near linear CNCC central portion of the molecule. This *N*-carboxymethyl-2-aminoacetonitrile (CAAN) is a species previously located by Balta et al. [42] and called a retro-Ritter product by Reid et al. [43]. CAAN[O_{2c}]-t and CAAN[O_{2t}]-t have C-O bond distances of 3.240 and 3.117 Å and lie 72 – 76 and 105 – 110 kJ/mol, respectively, above the H^+AMOx GS.

If the ring oxygen (O_1) is protonated, the OC-O bond of the ring cleaves forming an acylium ion stabilized by interaction with the hydroxyl group. There are three of these [O_1] conformers having different side chain orientations, t, c_t, and c, lying 118 – 128, 160 – 171, and 162 – 174 kJ/mol, respectively, above the GS. The former is stabilized by the OH•NH_2

UU IR Author Manuscript

hydrogen bond, which is also evident in the longer OC-OH bond distance of 2.637 Å compared to 2.577 and 2.589 Å for the c_t and c conformers. Alternatively, ring-protonated AMOx can break the other O-C bond in the ring leading to the open nitrile structures, CAAN[O_{1c}]-g and t, lying 82 – 86 and 84 – 87 kJ/mol above the GS. The latter complex is related to the CAAN[O_{2c}]-t by rotation of the carboxylic acid group.

Of the transition states located, the key one is TS(H^+AMOx[N_1-O_1]-t), which transfers the proton from the terminal nitrogen to the ring oxygen and. This is the lowest energy pathway found that converts from N-protonated to O-protonated species, lying 117 – 127 kJ/mol above the H^+AMOx GS. Notably, although the H^+AMOx[O_1]-t species can be located (lying 3.9 – 5.4 kJ/mol below the TS before zero point energy (ZPE) corrections are made). Once these corrections are made, the TS lies below this species by 0.7 – 2.3 kJ/mol. Thus, the proton spontaneously reverts back to the nitrogen. In order to form a stable O-protonated form, the side chain must rotate back over TS(H^+AMOx[O_1]-(t-c)) at 166 – 177 kJ/mol above the GS, Table S3, such that this is the rate-limiting TS for production of stable oxygen-protonated conformers. This is sufficiently high in energy that such conformers are not important in the dissociation of H^+AMOx.

Theoretical Results for Direct $b_2^+ \rightarrow a_1^+$ Decomposition

Siu and coworkers elucidated a mechanism for directly forming the $CH_2NH_2^+$ (a_1^+) ion from b_2^+ [1,39]. Our exploration of this mechanism is shown in Figure S4 and differs from that reported earlier in the initial steps. Table S6 lists the energies of the various species involved. Despite repeated attempts to relocate the rate-limiting TS reported by Siu and coworkers (including use of both the 6-31++G(d,p) and 6-311+G(d,p) basis sets as well as starting points constructed to mimic that reported in the Supporting information of their paper), we could never find a TS (**1→6**) that directly connected H^+AMOx[N_2]-c (**1**) with the c-$C_3H_4NO_2^+$[N]$(CH_2NH)_{CHN}$ complex (**6**). Rather, H^+AMOx[N_2]-c first transforms to H^+AMOx[N_2]-g_t, which removes the stabilizing N_2H•N_1 hydrogen bond. Then the system passes over TS(H^+AMOx[N_2]-g_t(C~C)) in

which the carbon bond to the amino-methyl group is broken. This TS lies 160 – 164 (DFT) or 189 (MP2) kJ/mol above the H^+AMOx GS, compared to the 174 kJ/mol value that Siu and coworkers found for TS(**1**→**6**). Our TS is partially stabilized by a NH•O(ring) hydrogen bond (2.23 Å), which is not present in the structure reported by Siu and coworkers. This TS leads to a $(c\text{-}C_3H_3NO_2)(CH_2NH_2^+)_{OHN}$ complex that retains the NH•O(ring) hydrogen bond (1.83 Å). Lying only 1 – 3 kJ/mol higher in energy (and 7 – 12 kJ/mol below the rate-limiting TS) is $TS(cC_3H_3NO_2)(CH_2NH_2^+)_{(OC)HN}$, in which the NH•O(ring) bond is broken and replaced by N•HC, thereby forming a covalent CH bond and the relatively stable $(c\text{-}C_3H_4NO_2^+[N])(CH_2NH)_{CHN}$ complex (**6**). From here, the mechanism shown in Figure S4 matches that of Siu and coworkers [1]. The CH_2NH species transfers from the N•HC hydrogen bond to a more stable N•HN bond, where the proton is equally shared between the $c\text{-}C_3H_3NO_2$ and CH_2NH units as indicated by energy differences of 0 – 2 (**0**) kJ/mol. In agreement with Siu and coworkers, the TS between having the proton localized on either unit actually lies lower in energy once zero point corrections are made, by 3 – 5 (**5**) kJ/mol. Thus, dissociation of this complex can easily form both $CH_2NH_2^+$ + $c\text{-}C_3H_3NO_2$ and $c\text{-}C_3H_4NO_2^+[N]$ + CH_2NH, with the former products being favored by 20 – 23 (**25**) kJ/mol. The latter product (*m/z* 86) was not observed either here or by Siu and coworkers, but in our work, it could be masked by the much more intense primary product ion at *m/z* 87. In either case, the products are limited by the rate-limiting $TS(H^+AMOx[N_2]\text{-}g_t(C\sim C))$ at 160 – 189 kJ/mol. This is 32 – 63 (**36**) kJ/mol above the TS for decarbonylation of H^+AMOx, and in addition, the former TS is tighter than the latter with entropies of activation of 23 versus 42 J/K mol. Thus, direct cleavage of $b_2^+ \rightarrow a_1^+$ in reaction (3b) will not compete very effectively with formation of a_2^+ in reaction (1) at low energies.

Siu and coworkers also located another means of forming a_1^+ directly from b_2^+ that involves synchronously breaking three bonds, leading to direct formation of $CH_2NH_2^+$ + H_2CCO + HNCO. This $TS(H^+AMOx[N_2]\text{-}c\{OC\sim O,C\sim N,C\sim C\})$ (**1**→**5**) was very high in energy, 299.2 kJ/mol, and therefore was not explored further here.

For the b_2^+ ion derived from H^+GAG, the ring in H^+AMOx is methylated. In agreement

with Siu and coworkers, we find the TS for direct formation of $CH_2NH_2^+$ (a_1^+) from H^+MAMOx, TS(H^+MAMOx[N_2]-g_t{C~C}) (**1→8**), lies 6 (**7**) kJ/mol above the analogous TS in the H^+AMOx system, Table S6, which Siu and coworkers attribute to better charge stabilization of the associated b_2^+ ion. Because the mechanism shown in Figure S4 forms the $CH_2NH_2^+$ (a_1^+) ion involving the terminal nitrogen, an analogous mechanism for ring-methylated H^+MAMOx cannot form $C_2H_4NH_2^+$. As noted above, the very similar shapes and magnitudes of the $C_2H_4NH_2^+$ and $CH_2NH_2^+$ cross sections in Figure 1c with each other and with that for $CH_2NH_2^+$ in Figure 1a indicates that these species are dominantly formed by similar mechanisms. This is consistent with the decomposition of the proton-bound $H^+(CH_2NH)(RCHNH)$ complex (where R = H or CH_3) but not with the direct $b_2^+ \rightarrow a_1^+$ mechanism. Therefore interpretation of the threshold for appearance of the a_1^+ ion via this mechanism, whether in competition with a_2^+ formation or not, as suggested by Siu and coworkers, is inconsistent with our results. Harrison and coworkers reached the same conclusion for the methylated b_2^+ ion [44].

To further verify this result, we analyzed the data for $b_2^+(H^+GGG)$ as a competition between a_2^+ and a_1^+ formation. Both channels could be reproduced with high fidelity (with only small changes in the parameters for a_2^+ formation), however, the cross section for a_1^+ formation had to be scaled upwards by a factor between $8 - 150 \times 10^3$, a nonphysical result that could indicate the calculated TS is too tight. However, as noted above, the $\Delta S^{\ddagger}_{1000}$ value is 23 J/K mol, which is not that much tighter than for the a_2^+ channel, 42 J/K mol. Such a scaling factor can sometimes be removed by scaling the frequencies instead. In order to reproduce the data in this fashion, the vibrational frequencies (arbitrarily chosen as < 625 cm^{-1}) for the TS needed to be scaled by $0.3_5 \pm 0.1$, which leads to a $\Delta S^{\ddagger}_{1000}$ value of 102 J/K mol, much larger than most phase-space-limit TSs (a product-like TS that is the loosest reasonable TS). In these models, the thresholds for a_1^+ formation are similar, 2.29 ± 0.12 and 2.21 ± 0.20 eV, Table S5, well above the values obtained by Siu and coworkers, 1.69 +0.08/-0.12 eV with competition and 1.85 +0.09/-0.13 eV when competition was ignored. We also note that our thresholds are inconsistent with the theoretically calculated energies of TS(H^+MAMOx[N_2]-g_t{C~C}), 160 – 189 kJ/mol. For

UU IR Author Manuscript

completeness, we also tried using the parameters of Siu and coworkers (with no scaling of the cross section or frequencies) to reproduce our data, but this gives a cross section for the a_1^+ ion that has the wrong shape and is an order of magnitude too small above 4 eV even though the threshold is much too low compared to our data. Overall, we conclude that although this pathway may contribute to the total a_1^+ cross sections at high energies, it cannot be the primary pathway for its formation.

Theoretical Results for Alternate Decomposition Pathways of H^+DKP: Reactions (12) and (14)

The lowest energy pathway found for reactions (12) and (14) is shown in Figure S5. It starts with the c-$C_3H_7N_2O^+[N_1]$ product ion formed after decarbonylation of H^+DKP, Figure 4. Cleavage of the CN bond assisted by backside attack of the oxygen forms an epoxide, c-$CH_2C(O)NHCH_2NH_2^+[N_1]$-c, with a transition state lying 226 – 236 kJ/mol above H^+DKP. Rotating the terminal amino-methyl group to a trans position costs little energy, 9 – 11 kJ/mol, and forms c-$CH_2C(O)NHCH_2NH_2^+[N_1]$-t. From here, a proton can transfer from the central CH_2 group to the terminal CH_2 group over the rate-limiting transition state at 287 – 328 kJ/mol, which is 14 – 27 kJ/mol lower than that for the pathway to reactions (11) and (13). This process forms the ketone $CH_3C(=O)NHCHNH_2^+[N_1]$-tc, which is the most stable of the $C_3H_7N_2O^+$ isomers examined here, lying 60 – 81 kJ/mol below the cyclic form (and along with the CO product, 11 – 16 kJ/mol below H^+DKP). (As noted in the text, the $CH_3C(=O)NHCHNH_2^+$ isomer was not considered by Siu and coworkers [45] or Bythell et al. [46] in their IRMPD studies of the a_2^+ ion, even though it is lower in energy and can be derived directly from the cyclic species c-$C_3H_7N_2O^+[N]$ with an energy barrier lower than those leading to some isomers that were considered.) From this species, cleavage of the CN bond passes over TS($CH_3C(=O)NHCHNH_2^+[N_1]$-tc{C~N}) to form the products of reaction (14) and proton transfer yields those of reaction (12). As these products lie 226 – 239 and 83 – 125 kJ/mol, respectively, below the rate-limiting TS, formation of these species should be facile once the H atom transfer TS is surmounted. Ultimately, although the rate-limiting TS for this pathway is

UU IR Author Manuscript

lower in energy than that for reactions (11) and (13), it appears to be inactive because the $H_2NCHNH_2^+$ (*m/z* 45) product ion is not observed and the large difference in the relative energies of reactions (12) and (14) disfavors appreciable formation of the CH_3CO^+ product ion. This observation can probably be understood by realizing that the $C_3H_7N_2O^+$ product (whether in the linear or cyclic conformation) can dissociate by decarbonylation much more easily than by reactions (12) and (14). The former process is restricted by TS($C_3H_7N_2O^+[N_2]$-ct{C~OC~N}) at 201 – 216 kJ/mol above H^+ DKP, whereas the latter lies 85 – 112 kJ/mol higher in energy.

References

[1] H. El Aribi, C.F. Rodriquez, D.R.P. Almeida, Y. Ling, W.W.-N. Mak, A.C. Hopkinson, K.W.M. Siu, J. Am. Chem. Soc. 125 (2003) 9229.
[2] D. Gerlich, Adv. Chem. Phys. 82 (Part 1) (1992) 1.
[3] K.M. Ervin, P.B. Armentrout, J. Chem. Phys. 83 (1985) 166.
[4] N. Aristov, P.B. Armentrout, J. Phys. Chem. 90 (1986) 5135.
[5] D.A. Hales, P.B. Armentrout, J. Cluster Science 1 (1990) 127.
[6] A. Mookherjee, M.J. Van Stipdonk, P.B. Armentrout, work in progress.
[7] R.M. Moision, P.B. Armentrout, J. Am. Soc. Mass Spectrom. 18 (2007) 1124.
[8] R.M. Moision, P.B. Armentrout, J. Phys. Chem. A 106 (2002) 10350.
[9] A.L. Heaton, R.M. Moision, P.B. Armentrout, J. Phys Chem. A 112 (2008) 3319.
[10] A.L. Heaton, P.B. Armentrout, J. Phys. Chem. B 112 (2008) 12056.
[11] T. Kim, A.V. Tolmachev, R. Harkewicz, D.C. Prior, G. Anderson, H.R. Udseth, R.D. Smith, Anal. Chem. 72 (2000) 2247.
[12] D.R. Carl, R.M. Moision, P.B. Armentrout, J. Am. Soc. Mass Spectrom. 20 (2009) 2312.
[13] S.J. Ye, R.M. Moision, P.B. Armentrout, Int. J. Mass Spectrom. 240 (2005) 233.
[14] A.L. Heaton, P.B. Armentrout, J. Am. Chem. Soc. 130 (2008) 10227.
[15] A.L. Heaton, S.J. Ye, P.B. Armentrout, J. Phys. Chem. A 112 (2008) 3328.
[16] S.J. Ye, P.B. Armentrout, J. Phys. Chem. A 112 (2008) 3587.
[17] E. Teloy, D. Gerlich, Chem. Phys. 4 (1974) 417.
[18] D. Gerlich, Adv. Chem. Phys. 82 (1992) 1.
[19] N.F. Dalleska, K. Honma, L.S. Sunderlin, P.B. Armentrout, J. Am. Chem. Soc. 116 (1994) 3519.
[20] N.R. Daly, Rev. Sci. Instrum. 31 (1960) 264.
[21] K.M. Ervin, P.B. Armentrout, J. Chem. Phys. 83 (1985) 166.
[22] F. Muntean, P.B. Armentrout, J. Chem. Phys. 115 (2001) 1213.
[23] T.S. Beyer, D.F. Swinehart, Commun. ACM 16 (1973) 379.
[24] S.E. Stein, B.S. Rabinovitch, J. Chem. Phys. 58 (1973) 2438.
[25] S.E. Stein, B.S. Rabinovitch, Chem. Phys. Lett. 49 (1977) 183.
[26] R.G. Gilbert, S.C. Smith, Theory of Unimolecular and Recombination Reactions, Blackwell Scientific, London, 1990.
[27] P.J. Robinson, K.A. Holbrook, Unimolecular Reactions, Wiley Interscience, New York, 1972.
[28] M.T. Rodgers, K.M. Ervin, P.B. Armentrout, J. Chem. Phys. 106 (1997) 4499.
[29] M.T. Rodgers, P.B. Armentrout, J. Chem. Phys. 109 (1998) 1787.
[30] P.B. Armentrout, J. Chem. Phys. 126 (2007) 234302.
[31] P.B. Armentrout, A.L. Heaton, J. Am. Soc. Mass Spectrom. (2011) in press.

[32] D.A. Hales, L. Lian, P.B. Armentrout, Int. J. Mass Spectrom. Ion Processes 102 (1990) 269.
[33] F. Muntean, P.B. Armentrout, J. Phys. Chem. B. 106 (2002) 8117.
[34] F. Muntean, P.B. Armentrout, J. Phys. Chem. A 107 (2003) 7413.
[35] A.L. Heaton, P.B. Armentrout, J. Am. Soc. Mass Spectrom. 20 (2009) 852.
[36] M.J. Frisch, G.W. Trucks, H.B. Schlegel, G.E. Scuseria, M.A. Robb, J.R. Cheeseman, J.A. Montgomery, Jr., T. Vreven, K.N. Kudin, J.C. Burant, J.M. Millam, S.S. Iyengar, J. Tomasi, V. Barone, B. Mennucci, M. Cossi, G. Scalmani, N. Rega, G.A. Petersson, H. Nakatsuji, M. Hada, M. Ehara, K. Toyota, R. Fukuda, J. Hasegawa, M. Ishida, T. Nakajima, Y. Honda, O. Kitao, H. Nakai, M. Klene, X. Li, J.E. Knox, H.P. Hratchian, J.B. Cross, C. Adamo, J. Jaramillo, R. Gomperts, R.E. Stratmann, O. Yazyev, A.J. Austin, R. Cammi, C. Pomelli, J.W. Ochterski, P.Y. Ayala, K. Morokuma, G.A. Voth, P. Salvador, J.J. Dannenberg, V.G. Zakrzewski, S. Dapprich, A.D. Daniels, M.C. Strain, O. Farkas, D.K. Malick, A.D. Rabuck, K. Raghavachari, J.B. Foresman, J.V. Ortiz, Q. Cui, A.G. Baboul, S. Clifford, J. Cioslowski, B.B. Stefanov, G. Liu, A. Liashenko, P. Piskorz, I. Komaromi, R.L. Martin, D.J. Fox, T. Keith, M.A. Al-Laham, C.Y. Peng, A. Nanayakkara, M. Challacombe, P.M.W. Gill, B. Johnson, W. Chen, M.W. Wong, C. Gonzalez, J.A. Pople, Gaussian 03, revision B.02, Gaussian, Inc., Pittsburgh, PA, 2003.
[37] J.A. Montgomery, Jr., M.J. Frisch, J.W. Ochterski, G.A. Petersson, J. Chem. Phys. 110 (1999) 2822.
[38] P.B. Armentrout, A.L. Heaton, S.J. Ye, J. Phys. Chem. A. (2011) in press.
[39] H. El Aribi, G. Orlova, C.F. Rodriquez, D.R.P. Almeida, A.C. Hopkinson, K.W.M. Siu, J. Phys. Chem. B 108 (2004) 18743.
[40] G. Bouchoux, J.-Y. Salpin, Rapid Commun. Mass Spectrom. 13 (1999) 932.
[41] G.D. Oliveira, J.M.L. Martin, I.K.C. Silwal, J.F. Liebman, J. Computational Chem. 22 (2001) 1297.
[42] B. Balta, M. Basma, V. Aviyente, C. Zhub, C. Lifshitz, Int. J. Mass Spectrom. 201 (2000) 69.
[43] G.E. Reid, R.J. Simpson, R.A.J. O'Hair, J. Am. Soc. Mass Spectrom. 9 (1998) 945.
[44] A.G. Harrison, I.G. Csizmadia, T.-H. Tang, J. Am. Soc. Mass Spectrom. 11 (2000) 427.
[45] U.H. Verkerk, C.-K. Siu, J.D. Steill, H. El Aribi, J. Zhao, C.F. Rodriguez, J. Oomens, A.C. Hopkinson, K.W.M. Siu, J. Phys. Chem. Lett. 1 (2010) 868.
[46] B.J. Bythell, P. Maitre, B. Paizs, J. Am. Chem. Soc. 132 (2010) 14766.
[47] E. Uggerud, Theor. Chem. Acc. 97 (1997) 313.
[48] E.P.L. Hunter, S.G. Lias, J. Phys. Chem. Ref. Data 27 (1998) 413.
[49] S. Hammerum, T.I. Sølling, J. Am. Chem. Soc. 121 (1999) 6002.
[50] B. Paizs, M. Schnolzer, U. Warnken, S. Suhaib, A.G. Harrison, Phys. Chem. Chem. Phys. 6 (2004) 2691.
[51] R.A.L. Peerboom, S. Ingemann, N.M.M. Nibbering, J.F. Liebman, J. Chem. Soc. Perkin 2 (1990) 1825.
[52] R.A.J. O'Hair, P.S. Broughton, M.L. Styles, B.T. Frink, C.M. Hadad, J. Am. Soc. Mass Spectrom. 11 (2000) 687.
[53] B. Balta, V. Aviyente, C. Lifshitz, J. Am. Soc. Mass Spectrom. 14 (2003) 1192.

TABLE S1: Comparison of 0 K theoretical and experimental values for proton affinities (PA) of glycine (G) and CH_2NH and H^+G fragmentation.

	This work										Literature	
Process	B3LYP /TZ+[a]	MP2 /TZ+[b]	B3LYP// B3LYP[c]	B3LYP/ TZ++[d]	B3P86// B3LYP[e]	MP2// B3LYP[f]	MP2// MP2[g]	B3LYP /DZ[h]	B3LYP /DZ+[h]	B3LYP /DZ++[h]	theory	experiment
PA(G)	878.8	881.3	881.4	881.0	888.8	879.6	878.9	908.1	881.3	881.4	925 (MP2)[i] 895 (G2)[i]	880.5 ± 8[j]
PA(CH_2NH)	863.3	860.9	862.9	862.6	868.0	858.7	858.4	881.7	865.5	865.2	862.2 ± 3.0[k]	846.9 ± 8[i] 848 ± 8[l] 856.9 ± 6.3[m]
$H^+G \rightarrow$ $CH_2NH_2^+ +$ $H_2O + CO$	137.1	130.7	137.1	136.9	184.1	136.6	134.7	189.0	150.4	150.6	199.2 (B3LYP)[n] 118.4 (QCISD)[n] 172.8 (MP2)[n] 154 (MP2)[i]	139.0 ± 8.2[o]
MAD[p]	**1.6**	3.5	**1.2**	1.1	19.7	**2.3**	3.3	32.4	5.2	5.2		
MAD[q]	**3.4**	4.4	**3.0**	2.8	21.4	**1.8**	2.5	34.1	6.9	6.9		

[a] B3LYP/6-311+G(d,p). [b] MP2(full)/6-311+G(d,p). [c] B3LYP/6-311+G(2d,2p)//B3LYP/6-311+G(d,p). [d] B3LYP/6-311++G(2d,2p). [e] B3P86/6-311+G(2d,2p)//B3LYP/6-311+G(d,p). [f] MP2(full)/6-311+G(2d,2p)//B3LYP/6-311+G(d,p). [g] MP2(full)/6-311+G(2d,2p)// MP2(full)/6-311+G(d,p). [h] B3LYP/6-31G(d,p), B3LYP/6-31+G(d,p), and B3LYP/6-31++G(d,p). [i] Uggerud [47]: MP2/6-31G(d,p) and G2(MP2). [j] Hunter and Lias [48]. [k] W2 theory [41]. See also Hammerum and Sølling [49] and Paizs et al. [50]. [l] Peerboom et al. [51]. [m] Bouchoux and Salpin [40]. [n] O'Hair et al. [52]. 298 K values adjusted to 0 K. B3LYP/6-31G(d), QCISD(T)/6-31+G(d,p)//B3LYP/6-31G(d), MP2/6-31G(d). [o] Evaluated from literature heats of formation, see [38]. [p] Mean absolute deviation from experimental values and W2 value for PA(CH_2NH). [q] Mean absolute deviation from experimental values. PA(CH_2NH) from [40]. Bold indicates levels of theory used in the present study.

Table S2. Relative theoretical energies (kJ/mol) at 0 K of H^+AMOx and H^+DKP conformers and transition states (and their imaginary frequencies in cm^{-1}) connecting them.[a]

Species	B3LYP[b]	B3LYP//B3LYP[b]	MP2(full)//B3LYP[b]	Lit	imag freq
H^+AMOx[N_2]-c	0.0	0.0	0.0	0.0[c,d]	
H^+AMOx[N_1]-c	24.0	24.2	13.0	23.8[c]	
H^+AMOx[N_2]-g	29.4	28.5	30.7		
H^+AMOx[N_2]-g_t	33.6	31.6	35.9		
H^+AMOx[N_1]-t	43.0	44.7	33.4		
TS(H^+AMOx[N_2]-(cg))	29.9	29.1	31.2		69
TS(H^+AMOx[N_2]-g_{c-t})	45.6	43.1	47.6		306
TS(H^+AMOx[N_2-N_1]-c)	37.2	38.6	29.5		1269
TS(H^+AMOx[N_2]-(cg_t))	39.6	38.1	42.9		100
TS(H^+AMOx[N_1]-(ct))	50.9	51.2	40.7		79
H^+DKP[O_c]	-11.7 (0.0)	-11.9 (0.0)	-7.3 (0.0)	-12.6[d]	
H^+DKP[O_t]	-4.7 (7.0)	-4.4 (7.5)	0.0 (7.4)		
H^+DKP[N]	51.1 (62.8)	55.8 (67.8)	45.3 (52.7)	54.0[d]	
TS(H^+DKP[O_{c-t}])	19.8 (31.6)	19.2 (31.1)	25.8 (33.1)		555
TS(H^+DKP[O_t-N])	216.5 (228.2)	219.5 (231.3)	216.5 (223.8)		1833
TS(H^+DKP[O_c-N])	240.7 (252.4)	243.1 (255.0)	230.2 (237.5)		1735

[a] Values are relative to H^+AMOx[N_2]-c. Values in parentheses show the energies relative to H^+DKP[O_c]. [b] Values from the present study at the B3LYP/6-311+G(d,p), B3LYP/6-311+G(2d,2p)//B3LYP/6-311+G(d,p), and MP2(full)/6-311+G(2d,2p)//B3LYP/6-311+G(d,p) levels of theory. [c] B3LYP/6-31++G(d,p) results from Siu and coworkers [1]. [d] B3LYP/6-31+G(d,p) results from Balta et al. [53].

UU IR Author Manuscript

Table S3. Relative theoretical energies (kJ/mol) at 0 K of oxygen-protonated H^+AMOx conformers and transition states (and their imaginary frequencies in cm^{-1}) connecting them.[a]

Species	B3LYP[b]	B3LYP// B3LYP[b]	MP2(full) //B3LYP[b]	Lit[c]	imag freq
H^+AMOx[N_2]-c	0.0	0.0	0.0	0.0	
CAAN[O_{2c}]-t	74.8	75.5	72.2	72.0	
CAAN[O_{1c}]-g	83.9	86.0	82.0		
CAAN[O_{1c}]-t	85.8	87.2	84.2		
CAAN[O_{2t}]-t	109.9	107.0	105.3		
H^+AMOx[O_{2c}]-c_t [d]	116.6	111.4	119.2	113.4	
H^+AMOx[O_{2c}]-g_t	118.5	113.6	121.1		
H^+AMOx[O_1]-t	125.8	128.0	118.0		
H^+AMOx[O_{2t}]-c_t	130.0	122.2	129.6		
H^+AMOx[O_{2t}]-g_t	132.5	125.2	132.3		
H^+AMOx[O_1]-c_t	171.3	171.2	160.7		
H^+AMOx[O_1]-c	173.6	173.1	162.3		
TS(H^+AMOx[$O_{2c\text{-}1c}$]-t) (rotation -)	94.9	95.7	93.5		50
TS(H^+AMOx[$O_{2c\text{-}1c}$]-t) (rotation +)	95.1	95.9	93.6		50
CAAN[O_{1c}]-(g-t)	106.3	106.7	103.0		343
CAAN[O_{2t}]-(t-c-t)	113.2	110.2	108.7		8
TS(H^+AMOx[O_{2c}]-g_t-CAAN[O_{2c}]-t)	117.3	113.2	121.4		173
TS(H^+AMOx[N_1-O_1]-t)	123.5	126.8	117.3		396
TS(H^+AMOx[O_{2t}]-t-CAAN[O_{2c}]-t)	126.8	125.4	124.0		559
TS(H^+AMOx[O_{2c}]-(g^+_t-g^-_t)	128.2	123.2	130.4		89
TS(H^+AMOx[O_{2t}]-c_t-CAAN[O_{2t}]-t)	132.2	126.0	136.6		157
TS(H^+AMOx[O_{2t}]-(c-g_t)	139.2	131.8	139.8		75

TS(CAAN[O_{2t}-O_{1t}-O_{2t}]-t)	141.0	137.9	139.7	51
TS(H^+AMOx[O_{2t}]-(g^+_t-g^-_t)	141.3	134.0	141.1	89
TS(H^+AMOx[O_{2t-c}]-c)	169.1	162.6	173.9	715
TS(H^+AMOx[O_1]-(t-c))	176.9	177.2	166.2	77
TS(H^+AMOx[O_1]-(c-c_t))	179.3	178.6	168.2	242
TS(CAAN[O_{1c}]-t-H^+AMOx[O_{1c}]-c_t)	198.5	200.0	201.5	366
TS(CAAN[O_{1c}]-g-H^+AMOx[O_{1c}]-c)	202.4	203.9	205.4	362
TS(H^+AMOx[O_{2c}]-t -CAAN[O_{1c}]-t)	242.6	241.2	236.2	1990

[a] Values are relative to H^+AMOx[N_2]-c. [b] Values from the present study at the B3LYP/6-311+G(d,p), B3LYP/6-311+G(2d,2p)//B3LYP/6-311+G(d,p), and MP2(full)/6-311+G(2d,2p)//B3LYP/6-311+G(d,p) levels of theory. [c] B3LYP/6-31+G(d,p) values from Balta et al. [53]. [d] Geometry optimized at B3LYP/6-31+G(d,p) level. Collapses to CAAN[O_{2c}]-t at the present level of theory.

Table S4. Relative theoretical energies (kJ/mol) at 0 K of H^+AMOx and H^+DKP fragmentation intermediates, products, and transition states (and their imaginary frequencies in cm^{-1})

Species	B3LYP[a]	B3LYP// B3LYP[a]	MP2(full) //B3LYP[a]	Literature[b]	imag freq
H^+AMOx[N_2]-c	0.0	0.0	0.0	0.0 (**1**)	
TS(H^+AMOx[N_2]-c{OC~O})	127.8	131.7	126.4	137.7 (**1**→**2**)	338
TS(H^+AMOx[N_1]-c{OC~O})	151.4	154.4	147.1		386
TS(H^+DKP[N]{C~CO~N})	149.5	154.3	150.6		276
	(*161.2*)	(*166.1*)	(*157.9*)		
c-$C_3H_7N_2O^+$[N_1]($CO_{N1H•Cu}$)	27.5	31.9	9.5		
c-$C_3H_7N_2O^+$[N_1]($CO_{N1H•Cd}$)	27.7	32.3	10.5		
c-$C_3H_7N_2O^+$[N_1]($CO_{N2H•C}$)	37.4	41.9	21.5		
$C_3H_7N_2O^+$[N_1]-ct(OC_{HN1})	72.8	77.1	67.6		
$C_3H_7N_2O^+$[N_2]-ct(OC_{HN2})	80.0	84.7	75.7		
$C_3H_7N_2O^+$[N_2]-ct(OC_{HC})	80.8	85.9	81.5		
$C_3H_7N_2O^+$[N_2]-ct(OC_C)	81.0	86.1	80.4	92.5 (**2**)	
$C_3H_7N_2O^+$[N_2]-ct(OC_{HN1})	82.3	87.3	82.4		
$C_3H_7N_2O^+$[N_1]-ct(OC_C)	88.1	92.8	85.4		
$C_3H_7N_2O^+$[N_2]-cc(OC_{HN2})	112.9	117.0	104.6		
$C_3H_7N_2O^+$[N_2]-cc(OC_C)	123.4	127.9	116.6		
$C_3H_7N_2O^+$[N_2]-cc(OC_{HN1})	123.6	128.1	118.1		
TS($C_3H_7N_2O^+$[N_2]-ct(CO_{HN1-HC}))	81.0	86.1	80.7		20
TS($C_3H_7N_2O^+$[N_2]-ct(CO_{C-HC}))	82.2	87.3	83.2		29
TS($C_3H_7N_2O^+$[N_2]-ct($CO_{HN2-HN1}$))	84.8	89.8	82.5		24
TS($C_3H_7N_2O^+$[N_1]-ct(CO_{HN1-C}))	89.5	94.1	85.2		18

TS($C_3H_7N_2O^+[N_1\text{-}N_2]$-ct($CO_{HN1}$))	90.6	96.7	90.7		1139
TS(c-$C_3H_7N_2O^+[N_1]${C~N_1}(CO_{HN2}))	109.3	114.1	113.3		183
TS(c-$C_3H_7N_2O^+[N_1]${C~N_1}(CO_{HN1}))	118.5	123.1	123.6		176
TS($C_3H_7N_2O^+[N_2]$-cc($CO_{HN2\text{-}HN1}$))	125.3	129.7	116.8		33
TS($C_3H_7N_2O^+[N_2]$-cc($CO_{C\text{-}HN2}$))	123.4	127.8	118.4		25
c-$C_3H_7N_2O^+[N_1]$ + CO	50.8	55.4	41.9	59.4 (**4**)	
$C_3H_7N_2O^+[N_2]$-ct + CO	91.0	96.1	96.8	102.5 (**3**)	
$C_3H_7N_2O^+[N_1]$-ct + CO	92.8	97.4	95.4		
$C_3H_7N_2O^+[N_2]$-cc + CO	120.6	125.0	125.5	132.2 (**12**)	
$H^+(CH_2NH)_2(OC_{HN})$ + CO	92.6	96.6	94.4		
$H^+(CH_2NH)_2(OC_C)$ + CO	100.6	104.9	103.8	120.5 (**14**)	
TS($C_3H_7N_2O^+[N_2\text{-}N_1]$-ct) + CO	104.1	110.4	110.7		1157
TS(c-$C_3H_7N_2O^+[N_1]${C~N_1}) + CO	128.3	133.1	140.3	139.7 (**4→12**)	182
TS($C_3H_7N_2O^+[N_2]$-c(tc)) + CO	136.6	139.5	138.1	150.2 (**3→4**)	114
TS($C_3H_7N_2O^+[N_2]$-ct{C~OC~N}) + CO	189.2	192.4	208.5	208.8 (**3→14**)	190
$H^+(CH_2NH)_2$ + 2 CO	106.8	111.3	115.8	126.4 (**15**)	
$H^+(CH_2NH)CO$ + CO + CH_2NH	191.9	192.9	195.9		
	(*203.7*)	(*204.7*)	(*203.3*)		
$CH_2NH_2^+$ + OCNH + CH_2CO	146.0	150.6	193.2	174.9 (**5**)	
$CH_2NH_2^+$ + CH_2NH + 2 CO	216.7	218.2	227.4	238.1	
	(*228.4*)	(*230.1*)	(*234.7*)		

[a] Values from the present study at the B3LYP/6-311+G(d,p), B3LYP/6-311+G(2d,2p)// B3LYP/6-311+G(d,p), and MP2(full)/6-311+G(2d,2p)//B3LYP/6-311+G(d,p) levels of theory. Values in italics are relative to $H^+DKP[O_c]$.

[b] B3LYP/6-31++G(d,p) values from Siu and coworkers [1]. Designations in parentheses are the names used by these authors.

TABLE S5: Fitting Parameters of Eq. (S1), Threshold Energies (eV) at 0 K, and Entropies of Activation (J/K mol) at 1000 K[a]

Reaction	Reactant	Products[b]	TS[c]	σ_0	n	E_0	$\Delta S^{\ddagger}_{1000}$
4	H^+DKP	$C_3H_7N_2O^+ + CO$	H^+DKP[O_t-N]	3.8 (0.8)	1.4 (0.2)	2.17 (0.18)	-15 (2)
6		$CH_3CO^+ + OCNH + CH_2NH$	$H^+CH_2CONHCH_2[O_c]\{C\sim N\}$			~2.77 (0.20)	24 (2)
1	b_2^+ (H^+GGG)	$a_2^+ + CO$	H^+AMOx{OC~O}	6.5 (2.4)	1.2 (0.2)	1.56 (0.12)	42 (2)
7	b_2^+ (H^+GAG)	$a_2^+ + CO$	H^+MAMOx{OC~O}	16.7 (4.6)	1.1 (0.2)	1.44 (0.10)	34 (2)
4	H^+DKP	$a_2^+ + CO$	H^+DKP[O_t-N]	5.4 (3.4)	1.4 (0.4)	2.11 (0.20)	-15 (2)
2		$\rightarrow H^+(CH_2NH)_2 + 2\ CO$	$C_3H_7N_2O^+\{C\sim OC\sim N\}$	5.7 (3.6)		2.97 (0.28)	40 (2)
5	H^+DKP	$CH_2NH_2^+(CO) + CH_2NH + CO$	$C_3H_7N_2O^+\{C\sim OC\sim N\}$	1.7 (01.0)	1.7 (0.2)	2.64 (0.16)	40 (2)
2		$H^+(CH_2NH)_2 + 2\ CO$	$C_3H_7N_2O^+\{C\sim OC\sim N\}$	3.7 (1.6)		2.58 (0.16)	40 (2)
3a		$\rightarrow CH_2NH_2^+ + CH_2NH + 2\ CO$	PSL	4.3 (2.4)		3.37 (0.12)	43 (10)
1	b_2^+ (H^+GGG)	$a_2^+ + CO$	H^+AMOx{OC~O}	5.8 (1.4)	1.2 (0.4)	1.55 (0.14)	42 (2)
2		$\rightarrow H^+(CH_2NH)_2 + 2\ CO$	$C_3H_7N_2O^+\{C\sim OC\sim N\}$	5.6 (2.0)		2.86 (0.28)	40 (2)
2	b_2^+ (H^+GGG)[d]	$H^+(CH_2NH)_2 + 2\ CO$	$C_3H_7N_2O^+\{C\sim OC\sim N\}$	4.0 (1.8)	1.5 (0.6)	2.50 (0.30)	40 (2)
3a		$\rightarrow a_1^+ + CH_2NH + 2\ CO$	PSL	3.7 (1.6)		2.92 (0.42)	43 (10)
1	b_2^+ (H^+GGG)[e]	$a_2^+ + CO$	H^+AMOx{OC~O}	6.9 (2.8)	1.1 (0.2)	1.58 (0.10)	42 (2)
3b		$a_1^+ + cC_3H_3NO_2$	H^+AMOx[N_2]-g_t{C~C}	2.7 (3.9) $\times 10^5$		2.29 (0.24)	23 (2)
				6.9 (2.8)[g]		2.21 (0.40)	102 (20)
7	b_2^+ (H^+GAG)	$a_2^+ + CO$	H^+MAMOx{OC~O}	16.7 (4.6)	1.1 (0.2)	1.44 (0.12)	34 (2)

8		→ $H^+(CH_2NH)(C_2H_4NH)$ + 2 CO	$C_4H_9N_2O^+${C~OC~N}	17.8 (6.0)		3.04 (0.18)	54 (2)
8	b_2^+ (H^+GAG)[f]	$H^+(CH_2NH)(C_2H_4NH)$ + 2 CO	$C_4H_9N_2O^+${C~OC~N}	4.5 (2.2)	1.4 (0.2)	2.62 (0.08)	54 (2)
9a		→ $C_2H_4NH_2^+$ + CH_2NH + 2 CO	PSL	13.2 (4.6)		2.62 (0.08)	34 (10)
9a	b_2^+ (H^+GAG)[e,h]	$C_2H_4NH_2^+$ + CH_2NH + 2 CO	PSL	8.2 (5.0)	1.8 (0.4)	2.73 (0.30)	32 (10)
10a		a_1^+ + C_2H_4NH + 2 CO	PSL			2.91 (0.30)	35 (10)

[a] Uncertainties (2 standard deviations) in parentheses. [b] Arrow indicates a sequential process coming after the previous entry. [c] H^+AMOx{OC~O} = TS(H^+AMOx[N_2]-c{OC~O}). H^+MAMOx{OC~O} = TS(H^+MAMOx[N_2]-ctg{OC~O}). $C_3H_7N_2O^+${C~OC~N} = $C_3H_7N_2O^+$[N_2]-ct{C~OC~N}. $C_4H_9N_2O^+${C~OC~N} = $C_4H_9N_2O^+$[N_2]-ctt{C~OC~N}. H^+AMOx{C~C} = H^+AMOx[N_2]-g_t{C~C}. PSL = loose phase space limit. [d] EM = $C_3H_7N_2O^+$[N_2]-ct. [e] Competition between the indicated TSs is included in the modeling. [f] EM = $C_4H_9N_2O^+$[N_2]-ctt. [g] Frequencies of TS below 625 cm^{-1} scaled by 0.3 – 0.4. [h] EM = $(C_2H_4NH)H^+(CH_2NH)$.

Table S6. Relative theoretical energies (kJ/mol) at 0 K of intermediates, products, and transition states (and their imaginary frequencies in cm^{-1}) involved in direct formation of $CH_2NH_2^+$ (a_1^+) from H^+AMOx (b_2^+) and H^+MAMOx (b_2^+)

Species	B3LYP[a]	B3LYP// B3LYP[a]	MP2(full) //B3LYP[a]	Literature[b]	imag freq
H^+AMOx[N_2]-c / *H^+MAMOx[N_2]-c*	0.0	0.0	0.0	0.0 (**1**)	
(c-$C_3H_3NO_2$)($CH_2NH_2^+$)$_{NHN}$	48.6	50.5	62.3	49.4 (**8**)	
(c-$C_3H_4NO_2^+$)(CH_2NH)$_{NHN}$	48.6	50.1	64.0	49.4 (**7**)	
(c-$C_3H_4NO_2^+$)(CH_2NH)$_{CHN}$	84.5	85.4	104.6	86.6 (**6**)	
(c-$C_3H_3NO_2$)($CH_2NH_2^+$)$_{OHN}$	149.7	155.1	176.0		
TS(c-$C_3H_3NO_2$)H^+(CH_2NH)$_{NHN}$	43.5	45.8	58.7	44.4 (**7→8**)	764
TS(c-$C_3H_4NO_2^+$)(CH_2NH)$_{(CN)HN}$	87.7	88.5	106.0	90.0 (**6→7**)	65
TS(c-$C_3H_3NO_2$)($CH_2NH_2^+$)$_{(OC)HN}$	153.0	156.3	177.0		131
TS(H^+AMOx[N_2]-g_t{C~C})	160.0	164.0	189.3	173.6 (**1→6**)[c]	219
TS(H^+MAMOx[N_2]-g_t{C~C})	*166.4*	*170.3*	*195.6*	*180.7* (**1→8**)[c]	*218*
$CH_2NH_2^+$ + c-$C_3H_3NO_2$	130.2	130.2	149.8	131.0 (**9**)	
$CH_2NH_2^+$ + c-$C_4H_5NO_2$	*142.7*	*143.1*	*161.7*	*143.1 (**11**)*	
c-$C_3H_4NO_2^+$ (H^+Ox) + CH_2NH	151.8	149.9	172.5	155.6 (**10**)	
c-$C_4H_6NO_2^+$ (H^+MOx) + CH_2NH	*148.3*	*146.3*	*170.1*		
c-$C_3H_3NO_2$ (carbene) + $CH_2NH_2^+$	245.8	247.1	280.3	244.3 (**11**)	

[a] Values from the present study at the B3LYP/6-311+G(d,p), B3LYP/6-311+G(2d,2p)// B3LYP/6-311+G(d,p), and MP2(full)/6-311+G(2d,2p)//B3LYP/6-311+G(d,p) levels of theory. Values in italics refer to methylated species.

[b] B3LYP/6-31++G(d,p) values from Siu and coworkers [1,39]. Designations in parentheses are the names used by these authors.

[c] This TS is not the same as that found in the present work. See text.

Table S7. Relative theoretical energies (kJ/mol) at 0 K of intermediates, products, and transition states (and their imaginary frequencies in cm^{-1}) involved in formation of CH_3CO^+ from H^+DKP

Species	B3LYP[a]	B3LYP// B3LYP[a]	MP2(full) //B3LYP[a]	imag freq
$H^+DKP[O_c]$	0.0	0.0	0.0	
$TS(H^+DKP[O_c]\{C\sim C,C\sim N\})$	273.8	278.3	272.5	581
$H^+CH_2CONHCH_2[O_c] + OCNH$	123.4	123.7	148.6	
$TS(H^+CH_2CONHCH_2[O_c]\{C\sim N\}) + OCNH$	301.6	305.4	354.8	376
$CH_2NH_2^+ + CH_2CO + OCNH$	157.8	162.5	200.6	
$CH_3CO^+ + CH_2NH + OCNH$	219.7	221.7	235.4	
$c\text{-}C_3H_7N_2O^+[N_1] + CO$	62.5	67.3	49.2	
$TS(c\text{-}C_3H_7N_2O^+[N_1]\{C\sim N\})+ CO$	226.6	229.2	235.8	372
$c\text{-}CH_2C(O)NHCH_2NH_2^+[N_1]\text{-}c + CO$	207.7	211.1	212.4	
$c\text{-}CH_2C(O)NHCH_2NH_2^+[N_1]\text{-}(ct) + CO$	216.7	219.8	223.2	80
$c\text{-}CH_2C(O)NHCH_2NH_2^+[N_1]\text{-}t + CO$	211.6	214.3	218.4	
$TS(c\text{-}CH_2C(O)NHCH_2NH_2^+[N_1]\text{-}t\{C\sim H\sim C\}) + CO$	287.0	289.2	327.9	438
$CH_3C(=O)NHCHNH_2^+[N_1]\text{-}tc + CO$	-16.3	-13.8	-11.3	
$TS(CH_3C(=O)NHCHNH_2^+[N_1]\text{-}tc\{C\sim N\}) + CO$	110.8	116.8	111.1	207
$H_2NCHNH_2^+ + CH_2CO + CO$	58.2	63.1	89.1	
$CH_3CO^+ + H_2NCHNH + CO$	204.0	206.0	202.5	

[a] Values from the present study at the B3LYP/6-311+G(d,p), B3LYP/6-311+G(2d,2p)// B3LYP/6-311+G(d,p), and MP2(full)/6-311+G(2d,2p)//B3LYP/6-311+G(d,p) levels of theory.

Figure Captions

Figure S1. Structures for H^+AMOx and H^+DKP with relative energies in kJ/mol from Table 1. Hydrogen bonds are shown by dashed lines.

Figure S2. Structures for oxygen protonated H^+AMOx with relative energies in kJ/mol from Table 1. Weak bonds are shown by dashed lines.

Figure S3. Potential energy surface for coupling between $[N_2]$ and $[N_1]$ forms of H^+AMOx and their decarbonylation pathways. Geometry optimizations and single point energies of each elementary step are determined at the B3LYP/6-311+G(d,p) level of theory and corrected for ZPE. Short dashed lines indicate hydrogen bonds and longer dashed lines show bonds that are breaking.

Figure S4. Reaction coordinate surface for direct formation of a_1^+ from H^+AMOx. Geometry optimizations and single point energies of each elementary step are determined at the B3LYP/6-311+G(d,p) level of theory and corrected for ZPE. Short dashed lines indicate hydrogen bonds and longer dashed lines show bonds that are breaking or particularly weak interactions.

Figure S5. Reaction coordinate surface for formation of CH_3CO^+ in reaction (12) and for reaction (14). Geometry optimizations and single point energies of each elementary step are determined at the B3LYP/6-311+G(d,p) level of theory and corrected for ZPE. Short dashed lines show bonds that are breaking or weak interactions.

UU IR Author Manuscript

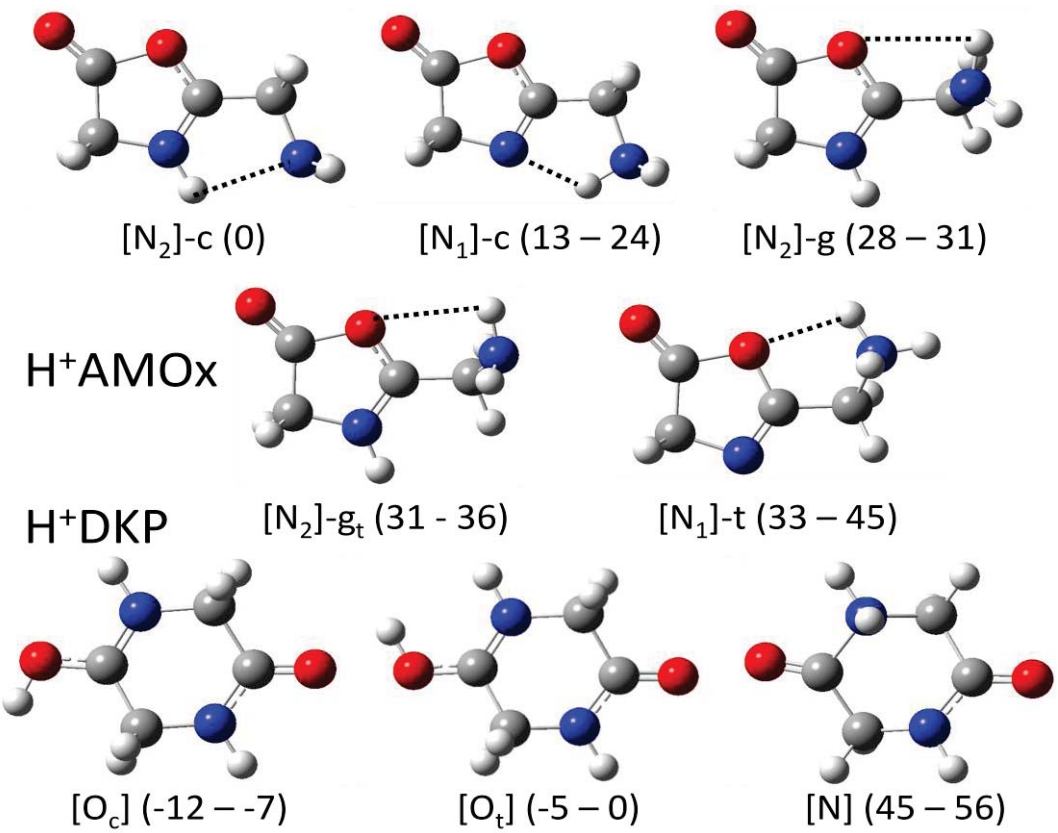

Figure S1

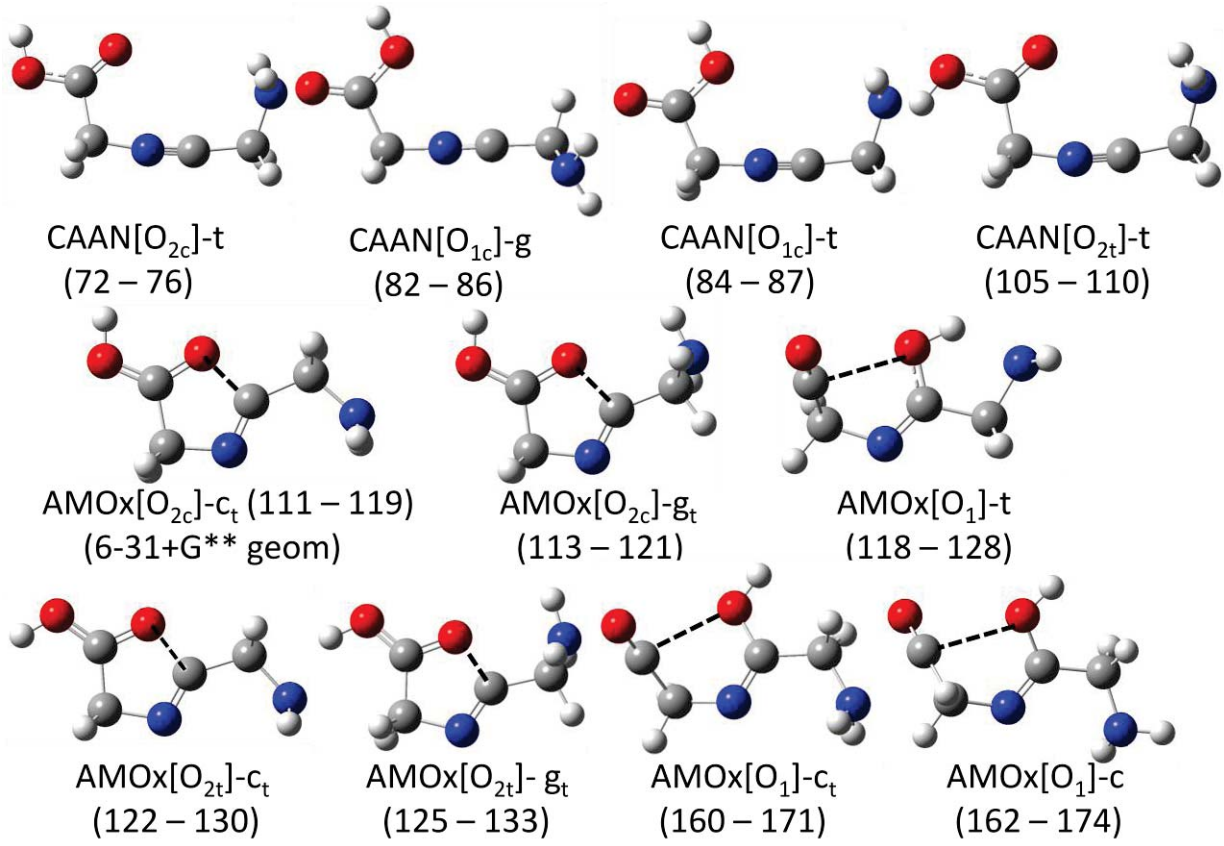

Figure S2

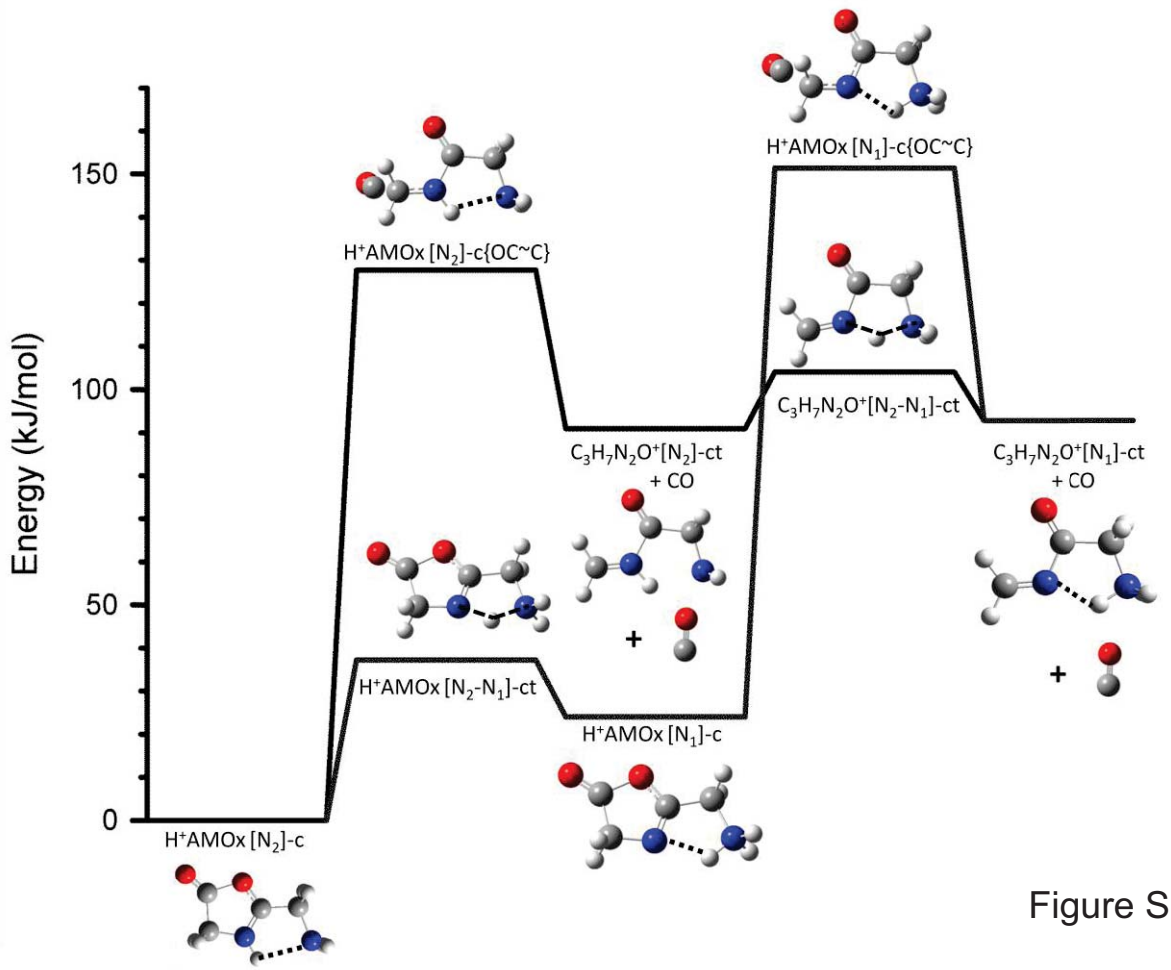

Figure S3

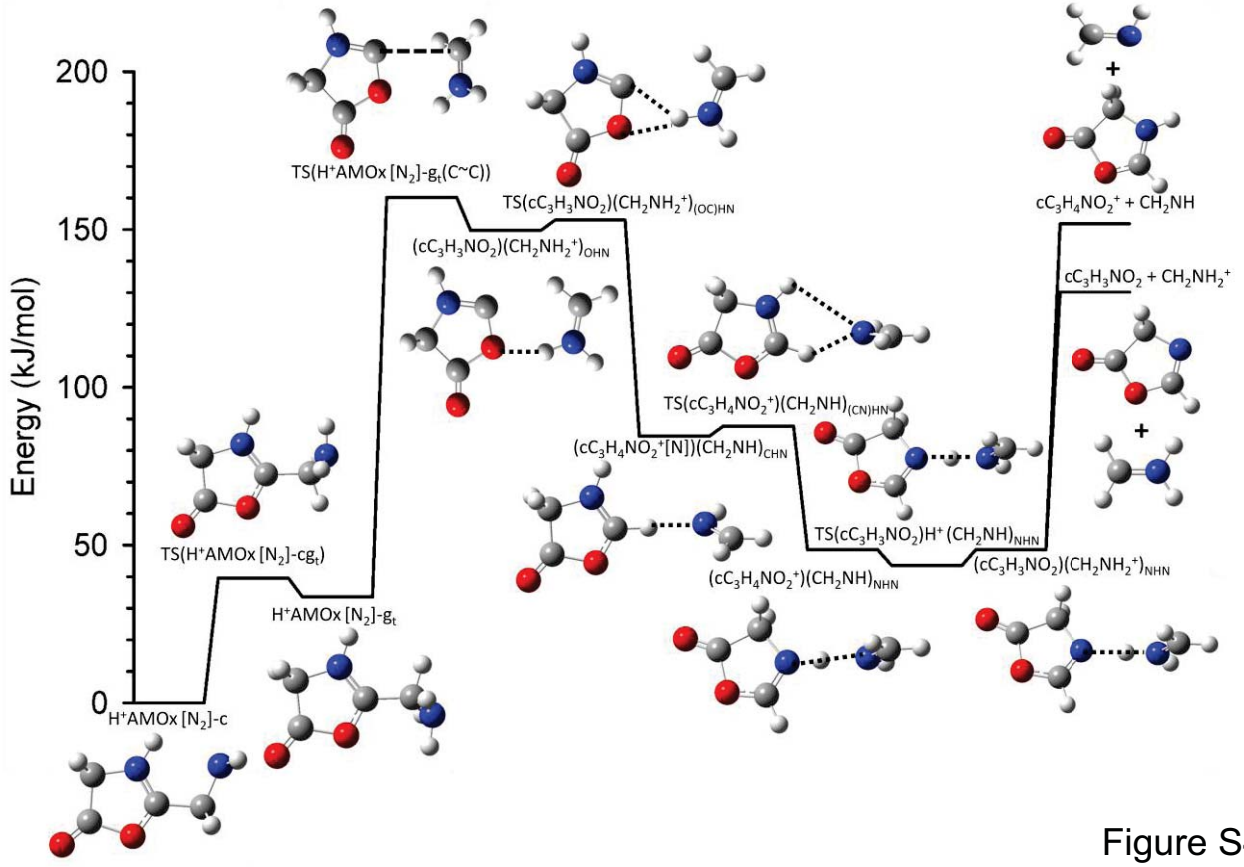

Figure S4

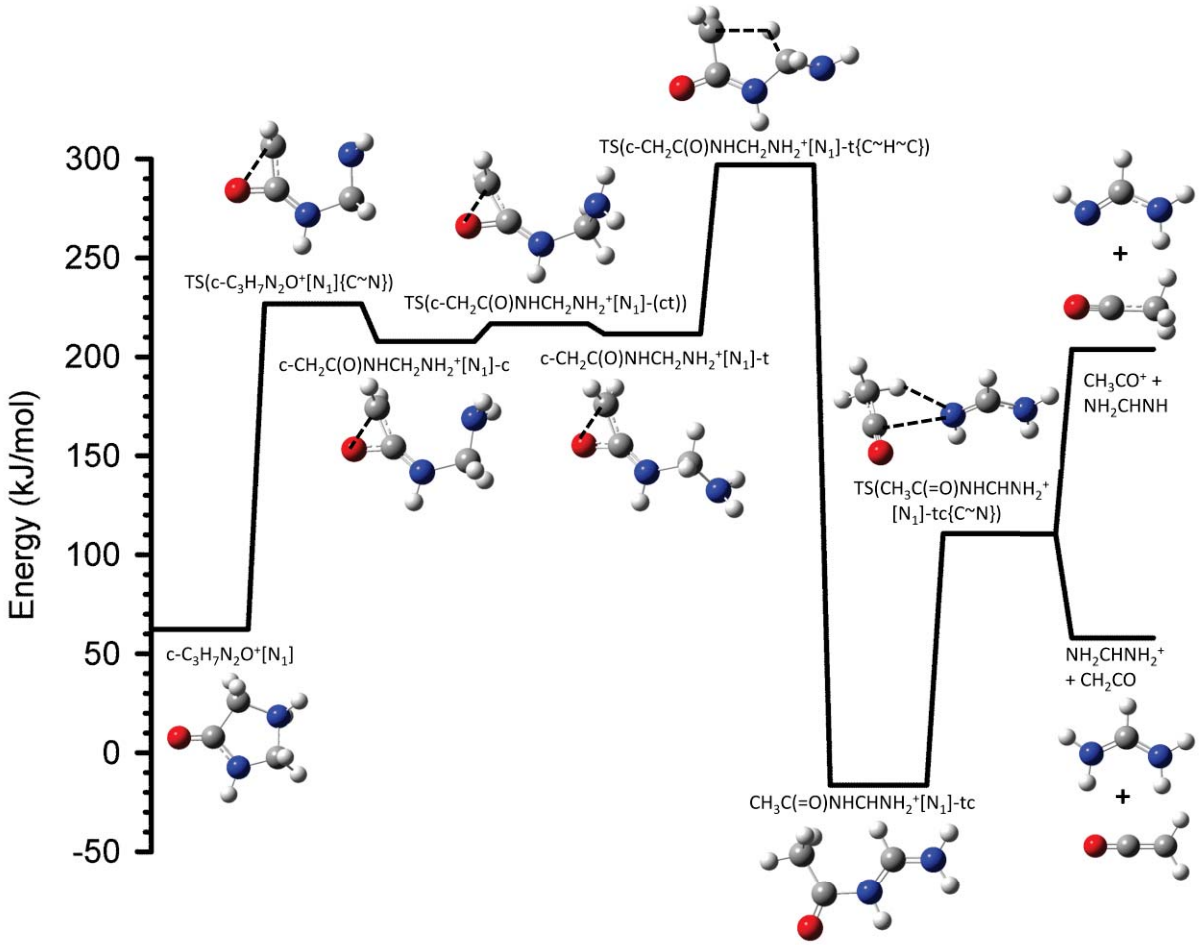

Figure S5